#### REPUBLIC OF TURKEY

# YILDIZ TECHNICAL UNIVERSITY GRADUATE SCHOOL OF SCIENCE AND ENGINEERING

# NON-DESTRUCTIVE APPROACH FOR DEFECT DETECTION IN CONCRETE STRUCTURES BY EM WAVES WITH FDTD TECHNIQUES

# Ümmü ŞAHİN ŞENER

DOCTOR OF PHILOSOPHY THESIS

Department of Mathematical Engineering

Mathematical Engineering Program

Supervisor

Asst. Prof. Dr. Sebahattin EKER

#### **REPUBLIC OF TURKEY**

#### YILDIZ TECHNICAL UNIVERSITY

#### GRADUATE SCHOOL OF SCINECE AND ENGINEERING

# NON-DESTRUCTIVE APPROACH FOR DEFECT DETECTION IN CONCRETE STRUCTURES BY EM WAVES WITH FDTD TECHNIQUES

A thesis submitted by Ümmü ŞAHİN ŞENER in partial fulfillment of the requirements for the degree of DOCTOR OF PHILOSOPHY is approved by the committee on 03.08.2021 in Department of Mathematical Engineering, Mathematical Engineering Program.

Asst. Prof. Dr. Sebahattin EKER
Istanbul Technical University
Supervisor

#### **Approved By the Examining Committee**

Asst. Prof. Dr. Sebahattin EKER, Supervisor	
Istanbul Technical University	
Prof. Dr. Ertuğrul KARAÇUHA, Member Istanbul Technical University	
Prof. Dr. Hülya ŞAHİNTÜRK, Member Yıldız Technical University	
Prof. Dr. İbrahim EMİROĞLU, Member Yıldız Technical University	
Asst. Prof. Dr. Süha TUNA, Member Istanbul Technical University	

I hereby declare that I have obtained the required legal permissions during data collection and exploitation procedures, that I have made the in-text citations and cited the references properly, that I haven't falsified and/or fabricated research data and results of the study and that I have abided by the principles of the scientific research and ethics during my Thesis Study under the title of Non-Destructive Approach for Defect Detection in Concrete Structures by Electromagnetic Waves with FDTD Techniques supervised by my supervisor, Asst. Prof. Dr. Sebahattin EKER. In the case of a discovery of false statement, I am to acknowledge any legal consequence.

Ümmü ŞAHİN ŞENER



#### **ACKNOWLEDGEMENTS**

I would like to offer my gratitude to my supervisor, Asst. Prof. Dr. Sebahattin Eker, both for him help and support in preparing this thesis, and for his guidance and efforts in developing my perspective on life and my personality.

I also would like to express my sincere to my thesis committee members, Prof. Dr. Ertuğrul Karaçuha and Prof. Dr. Hülya Şahintürk for their contributions and guidance. Many thanks to Prof. Dr. İbrahim Emiroğlu and Asst. Prof. Dr. Süha Tuna for their contributions.

I would like to thank Asst. Prof. Dr. Kadir Kılınç and master student Ahmet Savaş for their unwavering support in molding concrete samples and making them ready for measurement using the Kırklareli University Civil Engineering Laboratory.

I am indebted to Prof. Dr. İbrahim Akduman and Gökhan Cansız for their support in conducting the measurements at the Medical Devices Research Development and Application Laboratory of Istanbul Technical University.

Finally, I wish to express my forever gratefulness to my mother, and my father, who always make me proud of being their daughter in every breath of my life. Their unmeasured and unquestionable love always gives me the courage to overcome every obstacle in life. I am heartily thankful to my husband, Ersin Şener, for his warm support.

Ümmü ŞAHİN ŞENER

## **TABLE OF CONTENTS**

L	IST (	OF SYN	MBOLS	viii
L	IST (	OF ABI	BREVIATIONS	ix
L	IST (	OF FIG	URES	X
L	IST (	OF TAI	BLES	xiii
A	BST	RACT		xiv
Ö	ZET			xv
1	INT	rodu	JCTION	1
	1.1	Litera	ature Review	1
		1.1.1	Optical Methods	2
		1.1.2	Acoustic Emission	3
		1.1.3	Ultrasound	
		1.1.4	Magnetic Particle	
		1.1.5	Eddy Current	5
		1.1.6	Active Thermography	
		1.1.7	Liquid Penetrant	7
		1.1.8	Radiology	8
		1.1.9	Microwave and Radar	9
	1.2	Objec	tive of the Thesis	11
	1.3	Нуро	thesis	12
	1.4	Orgar	nization of the Dissertation	12
2	NU	MERIO	CAL SIMULATION AND FINITE DIFFERENCE TIME DOMAIN	
	IETH	_		14
	2.1	Basic	Facts and Knowledge	14
		2.1.1	Electromagnetic Methods and FDTD	
		2.1.2	The Advantage of the FDTD	
	2.2	The S	calar Wave Equation and FDTD	18
		2.2.1	Propagating-Wave Solutions	18
		2.2.2	Finite Differences	19
	2.3	Maxw	vell's Curl Equations and FDTD	22
		2.3.1	Reduction to Two Dimensions (2D)	
		2.3.2	Reduction to One Dimensions (1D)	27
		2.3.3	Equivalence to the Wave Equation in One Dimension	28

	2.4	Finite	Difference Time Domain Solution and Yee's Algorithm	29
		2.4.1	Finite Differences and Notation	30
		2.4.2	FDTD Updating Equations for Three-Dimensional Problems	31
		2.4.3	FDTD Updating Equations for Two-Dimensional Problems	38
		2.4.4	FDTD Updating Equations for One-Dimensional Problems	43
	2.5	Stabil	ity Criteria and Numerical Dispersion	46
		2.5.1	Stability Criteria in FDTD Algorithm	46
		2.5.2	Numerical Dispersion	48
	2.6	The Ir	ndependence of FDTD Method from Divergence	52
3	SO	URCE V	WAVEFORMS AND ABSORBING BOUNDARY CONDITIONS	54
	3.1	Sourc	e Waveforms for FDTD Simulations	54
		3.1.1	Sinusoidal Waveform	54
		3.1.2	Gaussian Waveform	55
	3.2	Absor	bing Boundary Conditions	59
			Mur Type ABC	
	3.3	Perfe	ctly Matched Layer	62
		3.3.1	Berenger PML	63
		3.3.2	Uniaxial PML	64
		3.3.3	Discrete Uniaxial PML	68
		3.3.4	Corner Regions	69
	3.4	Dielec	ctric Properties of Concrete	72
4	CO	NCRET	E TYPES AND SIMULATION SETUPS	74
	4.1	Surfac	ce Crack Definition	74
		4.1.1	Crack Definition	74
		4.1.2	Simulation Results for Surface Cracks	76
	4.2	Interi	or Crack Definition	79
		4.2.1	Definition of the Interior Crack via Riemann Integral Domain	79
		4.2.2	Simulation Results for Interior Crack	83
4.3 Material Characterization of Rectangular Concrete Blocks Contain Different Materials			85	
		4.3.1	Wave Propagation in Planarly Layered Media	85
		4.3.2	Layered Media Definitions	90
		4.3.3	Simulation Results of Layered Media Samples	97
	4.4	Cylind	lrical Concrete Types	103
		4.4.1	Definition of Cylindrical Concrete Types with Defects	103

P	PUBLICATIONS FROM THE THESIS			140
REFERENCES			131	
6	RE	SULTS	AND DISCUSSION	128
	5.3	Calcul	lating the Reflection and Transmission Coefficient	123
		5.2.2	Measurement Setup	120
		5.2.1	Vivaldi Antenna and Vivaldi Antenna Array	117
	5.2	Meası	urement of Concrete Samples	116
	5.1	Moldi	ng the Concrete Samples	113
5	Coı	ncrete	Structure Specimens and Measurements	112
		4.4.2	Simulation Results of Cylindrical Concretes	106

## **LIST OF SYMBOLS**

$\Delta x$	Cell Size in the x-Direction
$\Delta y$	Cell Size in the y-Direction
$\Delta z$	Cell Size in the z-direction
t	Computation Duration
$\Delta t$	Computation Time Step
×	Cross Product Symbol
abla	Curl Operator
$\hat{k_i}$	Direction of the Incident Wave
$\hat{k}_r$	Direction of the Reflected Wave
$\hat{k_t}$	Direction of the Transmission Wave
$\sigma$	Electric Conductivity of the Medium
$\mathbf{J}_{\mathrm{e}}$	Electric Current Density
E	Electric Field Strength
D	Electric Flux Density
ε	Electric Permittivity of the Medium
A	Electric Potential Vector
$\sigma^{^*}$	Equivalent Magnetic Loss
$\mathbf{J}_{\mathrm{m}}$	Magnetic Current Density
Н	Magnetic Field Strength
В	Magnetic Flux Density
μ	Magnetic Permeability of the Medium
c	Speed of Light in Free Space
$E_x$	x-Component of the Electric Field
$H_{x}$	x-Component of the Magnetic Field
$E_{y}$	y-Component of the Electric Field
$H_{y}$	y-Component of the Magnetic Field
$E_z$	z-Component of the Electric Field
$H_z$	z-Component of the Magnetic Field

#### LIST OF ABBREVIATIONS

ABC Absorbing Boundary Condition

AE Acoustic Emission

ASNT American Society of Nondestructive Testing

BPML Berenger Perfectly Matched Layer
CFL Courant-Friedrichs-Levy Criteria

CPML Convolutional Perfectly Matched Layer

DBC Dispersive Boundary Condition

EC Eddy Current

FDTD Finite Difference Time Domain

GPR Ground Penetrating Radar

MPI Magnetic Particle Inspection

MRTD Multiresolution Time Domain

NDC Nondestructive Characterization

NDE Nondestructive Evaluation

NDI Nondestructive Inspection

NDS Nondestructive Sensing

NDT Nondestructive Testing

PEC Perfect Electric Conductive

PMC Perfect Magnetic Conductive

PML Perfectly Matched Layer

PSTD Pseudospetral Time Domain

PT Penetrant Testing

SFD Static Finite Difference

SUT Specimen Under Test

TE Transverse Electric

TEM Transverse Electromagnetic

TF/SC Total Field/Scattered Field

TM Transverse magnetic

UPML Uniaxial Perfectly Matched Layer

VNA Vector Network Analyzer

## **LIST OF FIGURES**

Figure 2.1 (a) Unit Yee Cell (b) FDTD Space
<b>Figure 2.2</b> Field Components for Calculation of the $E_x(i,j,k)$
<b>Figure 2.3</b> Field Components for Calculation of the $H_x(i,j,k)$
Figure 2.4 Two-Dimensional TE <sub>z</sub> FDTD Field Components
Figure 2.5 Two-Dimenssional TM <sub>z</sub> FDTD Field Components
<b>Figure 2.6</b> One-Dimensional FDTD Positions of Field Components $E_y$ and $H_z$ 44
<b>Figure 2.7</b> One-Dimensional FDTD Positions of Field Components $E_z$ and $H_y$ 45
Figure 4.1 Surface Crack Model Defined by Rectangular Step Function
Figure 4.2 Surface Crack Model Defined by Dynamic Geometry
<b>Figure 4.3</b> Simulation Result for Case A at 600-Time Step: (a) $E_x$ Field Distribution for 1.5 GHz, (b) $E_z$ Field Distribution for 1.5 GHz, (c) $E_x$ Field Distribution for 3.0 GHz, (d) $E_z$ Field Distribution for 6.0 GHz, (f) $E_z$ Field Distribution for 6.0 GHz
<b>Figure 4.4</b> Simulation Result for Case B at 600-Time Step: (a) E <sub>x</sub> Field Distribution for 1.5 GHz, (b) E <sub>z</sub> Field Distribution for 1.5 GHz, (c) E <sub>x</sub> Field Distribution for 3.0 GHz, (d) E <sub>z</sub> Field Distribution for 3.0 GHz, (e) E <sub>x</sub> Field Distribution for 6.0 GHz, (f) E <sub>z</sub> Field Distribution for 6.0 GHz
Figure 4.5 Riemann Integral Definition: Rude Partition
Figure 4.6 Riemann Integral Definition: Thin Partition
Figure 4.7 Interior Crack Model
<b>Figure 4.8</b> Simulation Result for Case C at 700-Time Step: (a) $E_x$ Field Distribution for 1.5 GHz, (b) $E_z$ Field Distribution for 1.5 GHz, (c) $E_x$ Field Distribution for 3.0 GHz, (d) $E_z$ Field Distribution for 3.0 GHz, (e) $E_x$ Field Distribution for 6.0 GHz.
<b>Figure 4.9</b> 3-D Simulation Result for All Cases for 1.5 GHz: (a) $E_x$ for Case A at 600-Time Step, (b) $E_z$ for Case A at 600 Time Step, (c) $E_x$ for Case B at 600 Time Step, (d) $E_z$ for Case B at 600 Time Step, (e) $E_x$ for Case C at 700 Time Step, (f) $E_z$ for Case C at 700 Time Step
<b>Figure 4.10</b> Model A: Layered Media with Pavement, Mortar, Concrete and Horizontal Rebar93
<b>Figure 4.11</b> Model B: Layered Media with Pavement, Mortar, Concrete and Vertica Rebar
Figure 4.12 Model C: Layered Media with Circular Pavement and Concrete 93
Figure 4.13 Model D: Layered Media with Concrete and Soil94
Figure 4.14 Model F. Lavered Media with Concrete and Soil

Figure 4.15 Model F Numerical Model of Computation Domain
<b>Figure 4.16</b> Simulation Result for Model A at 500-Time Step: (a) $E_x$ Field Distribution for 1.5 GHz, (b) $E_z$ Field Distribution for 1.5 GHz, (c) $E_x$ Field Distribution for 3.0 GHz, (d) $E_z$ Field Distribution for 3.0 GHz, (e) $E_x$ Field Distribution for 6.0 GHz
<b>Figure 4.17</b> Simulation Result for Model B at 400-Time Step: (a) $E_x$ Field Distribution for 1.5 GHz, (b) $E_z$ Field Distribution for 1.5 GHz, (c) $E_x$ Field Distribution for 3.0 GHz, (d) $E_z$ Field Distribution for 3.0 GHz, (e) $E_x$ Field Distribution for 6.0 GHz.
<b>Figure 4.18</b> Simulation Result for Model C at 250-Time Step: (a) $E_x$ Field Distribution for 1.5 GHz, (b) $E_z$ Field Distribution for 1.5 GHz, (c) $E_x$ Field Distribution for 3.0 GHz, (d) $E_z$ Field Distribution for 3.0 GHz, (e) $E_x$ Field Distribution for 6.0 GHz99
<b>Figure 4.19</b> Simulation Result for Model D at 400-Time Step: (a) $E_x$ Field Distribution for 1.5 GHz, (b) $E_z$ Field Distribution for 1.5 GHz, (c) $E_x$ Field Distribution for 3.0 GHz, (d) $E_z$ Field Distribution for 3.0 GHz, (e) $E_x$ Field Distribution for 6.0 GHz
<b>Figure 4.20</b> Simulation Result for Model E at 450-Time Step: (a) E <sub>x</sub> Field Distribution for 1.5 GHz, (b) E <sub>z</sub> Field Distribution for 1.5 GHz, (c) E <sub>x</sub> Field Distribution FOR 3.0 GHZ, (D) E <sub>z</sub> Field Distribution for 3.0 GHz, (e) E <sub>x</sub> Field Distribution for 6.0 GHz, (f) E <sub>z</sub> Field Distribution for 6.0 GHz103
<b>Figure 4.21</b> Simulation Result for Model F at 450-Time Step: (a) E <sub>x</sub> Field Distribution for 1.5 GHz, (b) E <sub>z</sub> Field Distribution for 1.5 GHz, (c) E <sub>x</sub> Field Distribution for 3.0 GHz, (d) E <sub>z</sub> Field Distribution for 3.0 GHz, (e) E <sub>x</sub> Field Distribution for 6.0 GHz.
Figure 4.22 Cylinder A: Two-Layered FRP Tube with Concrete Core and Rebar.104
Figure 4.23 Cylinder B: One-Layered FRP Tube with Concrete Core and Crack105
Figure 4.24 Cylinder C: Concrete Cylinder with Styrfoam and Rebar106
<b>Figure 4.25</b> Simulation Result for Cylinder A at 400-Time Step: (a) $E_x$ field Distribution for 1.5 GHz, (b) $E_z$ Field Distribution for 1.5 GHz, (c) $E_x$ Field Distribution for 3.0 GHz, (d) $E_z$ Field Distribution for 3.0 GHz, (e) $E_x$ Field Distribution for 6.0 GHz
<b>Figure 4.26</b> Simulation Result for Cylinder B at 400-Time Step: (a) $E_x$ Field Distribution for 1.5 GHz, (b) $E_z$ Field Distribution for 1.5 GHz108
<b>Figure 4.27</b> Simulation Result for Cylinder B at 400-Time Step: (a) $E_x$ Field Distribution for 3.0 GHz, (b) $E_z$ Field Distribution for 3.0 GHz, (c) $E_x$ Field Distribution for 6.0 GHz109
<b>Figure 4.28</b> Simulation Result for Cylinder C at 400-Time Step: (a) $E_x$ Field Distribution for 1.5 GHz, (b) $E_z$ Field Distribution for 1.5 GHz, (c) $E_x$ Field Distribution for 3.0 GHz, (d) $E_z$ Field Distribution for 3.0 GHz, (e) $E_x$ Field Distribution for 6.0 GHz
<b>Figure 5.1</b> Preparation of Concrete Samples: (a) Preparation of Concrete Mix, (b) Keeping the Samples in the Curing Tank

Figure 5.	<b>.2</b> Physical Structure of Rectangular Models: (a) Case A, (b) Case B115
Figure 5.	.3 Physical Structure of Cylindrical Models: (a) Cylinder B, (b) Cylinder C
Figure 5.	4 Vivaldi Antenna Geometry: (a) 3-D View (b) Top View118
Figure 5.	.5 Measurement Setup for Rectangular Models: (a) Case A, (b) Case B122
Figure 5.	.6 Measurement Setup for Cylindrical Models: (a) Cylinder B, (b) Cylinder C
_	7 Measurement Results: (a) S-parameters for Case A, (b) S-parameters for Case B, (c) Reflection Coefficient for Case A, (d) Reflection Coefficient for Case B, (e) Transmission Coefficient for Case A, (f) Transmission Coefficient for Case B
Figure 5.	<b>.8</b> Measurement Results: (a) S-parameters for Cylinder B, (b) S-parameters for Cylinder C, (c) Reflection Coefficient for Cylinder B, (d) Reflection Coefficient for Cylinder C, (e) Transmission Coefficient for Cylinder B, (e) Transmission Coefficient for Cylinder C

# LIST OF TABLES

Table 3.1 Microwave Frequency Ranges	58
Table 5.1 Concrete Types and Strengths	114

# Non-Destructive Approach for Defect Detection in Concrete Structures by EM Waves with FDTD Techniques

Ümmü ŞAHİN ŞENER

Department of Mathematical Engineering

Doctor of Philosophy Thesis

Supervisor: Asst. Prof. Dr. Sebahattin EKER

In this study; concrete samples are divided into three groups and both simulation and non-destructive measurements are made using the electromagnetic characteristics of concrete and construction materials that can be used in concrete structures. Concrete structures may contain defects due to environmental factors such as humidity and temperature, exposure to sudden energy changes such as earthquakes or wear over time. These defects need to be checked for the service life of the concrete structure. The most basic defects in concrete structures are surface cracks that can be found on the concrete surface and can go down to a certain depth, or internal cracks that cannot be observed from the outside. Cracks do not have a definite shape due to the natural formation process. In our study, rectangular step function and dynamic geometry are used to express surface cracks. By adding the narrowing rectangles one after another towards the inside of the concrete, a deeper crack is expressed, while a relatively shallow crack is expressed by the succession of circles, with the origin of one circle being the tangent point of another circle. The area between the two curves used in the integral definition is used to express the inner crack. The crack in the interior of the concrete is the area between the two curves, namely the Riemann integral region, and this region is assumed to be filled with air. As it is known from the Riemann integral definition, the finer the partition of the area between the two curves is taken, the closer the area is to reality, so the crack modeling closest to reality is made by taking the fine partition of the air-filled area in the concrete. A concrete structure does not only consist of concrete, but also rebar, mortar, pavement and masonry can be found together with concrete. In addition, in environments with very high humidity, composite materials can be used together with concrete in the construction of piles. Considering these situations, modeling of concrete filled composite piles is made together with layered rectangular concrete structures containing mortar, masonry and soil. After determining the geometry of concrete samples, crack shape, content of layered samples and shape of concrete filled composite materials, samples are simulated with the help of FDTD, which is widely used in the simulation of electromagnetic wave propagation. Gaussian waves are used as input signals in simulations because frequency modulation is easier compared to other waveforms. In the numerical simulation, an absorber boundary condition is used to terminate the calculation region and to prevent the waves coming to the boundary from re-entering the calculation area. The results are compared using both transverse electric field and transverse magnetic field waves in the simulations. Two rectangular concrete specimens with surface cracks at different depths, one cylindrical concrete specimen with internal crack, and one cylindrical concrete specimen with rebar and avoids are prepared and dried in air. The prepared samples are measured in an anechoic chamber in the frequency range of 0.4-4.0 GHz using Vivaldi antenna array and vector network analyzer and scattering parameters are obtained. The reflection and transmission coefficients obtained from the scattering parameters and the reflection and transmission coefficients obtained from FDTD calculation are compared and the results are shown in figures.

**Keywords:** Concrete cracks, layered concrete samples, computational modeling, electromagnetic wave propagation, FDTD; microwave radar NDT

YILDIZ TECHNICAL UNIVERSITY
GRADUATE SCHOOL OF SCIENCE AND ENGINEERING

### Beton Yapılarda Kusur Tespitinde ZUSF Tekniği Kullanarak EM Dalgalar Aracılığıyla Tahribatsız Yaklaşım

Ümmü ŞAHİN ŞENER

Matematik Mühendisliği Bölümü

Doktora Tezi

Danışman: Dr. Öğr. Üyesi Sebahattin EKER

Bu çalışmada; beton numuneler üç gruba ayrılarak, betonun ve beton yapılarda kullanılabilen inşaat malzemelerinin elektromanyetik karakteristiği kullanılarak hem simülasyon hem de tahribatsız ölçüm yapılmıştır. Beton yapılar nem ve sıcaklık gibi çevresel faktörler sebebiyle, deprem gibi ani enerji değişimlerine maruz kalmakla ya da zamanla yıpranmasından dolayı kusurlar içerebilir. Bu kusurların beton yapının kullanım ömrü uzunluğu açısından kontrol edilmesi gerekmektedir. Beton yapılardaki en temel kusur beton yüzeyinde bulunup belirli bir derinliğe inebilen yüzey kırıkları ya da dış kısımdan gözlemlenemeyen iç kırıklardır. Kırıkların doğal oluşum sürecinden dolayı belirli bir şekilleri yoktur. Çalışmamızda yüzey kırıklarını ifade etmek için dikdörtgensel adım fonksiyonu ve dinamik geometri kullanılmıştır. Daralan dikdörtgenlerin birbiri ardınca betonun iç kısmına doğru eklenmesiyle daha derine inen bir kırık ifade edilirken bir çemberin orijini başka bir çemberin teğet noktası olacak şekilde çemberlerin birbirini takip etmesiyle nispeten daha yüzeysel bir kırık ifade edilmiştir. İç kırığı ifade etmek için integral tanımı ifadesinde kullanılan iki eğri arasında kalan alan ifadesi kullanılmıştır. Betonun iç kısmındaki kırık iki eğri arasında kalan alan yani Riemann integral bölgesi olup bu bölgenin hava ile dolu olduğu kabul edilmiştir. Riemann integral tanımından bilindiği üzere iki eğri arasındaki alanın parçalanışları ne kadar

ince alınırsa alan gerçeğe o kadar yakın ifade edilmiş olduğundan beton içindeki hava ile dolu alanın ince parçalanışı alınarak gerçeğe en yakın kırık modellemesi yapılmıştır. Bir beton yapı sadece betondan ibaret olmayıp, betonla birlikte inşaat demiri, harç, taş ve tuğla bir arada bulunabilir. Ayrıca nem oranının çok yüksek olduğu çevrelerde kolon inşasında betonla birlikte kompozit malzemeler birlikte kullanılabilir. Bu durumlar göz önünde bulundurularak harç, taş ve toprak içeren katmanlı dikdörtgensel beton yapılarla birlikte beton dolgulu kompozit kazıkların da modellemesi yapılmıştır. Beton numunelerin geometrisi, kırık şekli, katmanlı olma durumundaki içeriği ve beton dolgulu kompozit malzemelerin şekli belirlendikten sonra elektromanyetik dalganın yayılımının simülasyonunda yaygın kullanılan Zaman Uzayında Sonlu Farklar (ZUSF) yardımıyla numuneler simüle edilmiştir. Gauss dalgalarının frekans modülasyonu diğer dalga formlarına kıyasla daha kolay olduğundan simülasyonlarda giriş sinyali olarak kullanılır. nümerik simülasyonda hesaplama bölgesini sonlandırmak ve sınıra gelen dalgaların tekrar hesaplama alanına girmesini engellemek amacıyla soğurucu sınır koşulu kullanılır. Simülasyonlarda hem enine elektrik alan hem de enine manyetik alan dalgaları kullanılarak sonuçları karşılaştırılmıştır. Simülasyonu yapılan ve farklı derinliklerde yüzey kırığı içeren iki tane dikdörtgensel beton numune, bir tane iç kırık içeren silindirik beton numune, bir tane de inşaat demiri ve hava boşluğu içeren silindirik beton numune hazırlanmış ve hava ortamında kurutulmuştur. Hazırlanan numuneler Vivaldi anten dizisi ve vektör ağ analizörü kullanılarak 0.4-4.0 GHz frekans aralığında yankısız odada ölçülüp saçılma parametreleri elde edilmiştir. Saçılma parametrelerinden elde edilen yansıma ve iletim katsayıları ile ZUSF kullanılarak elde edilen yansıma ve iletim katsayıları karşılaştırılarak sonuçlar grafiklerle gösterilmiştir.

**Anahtar Kelimeler:** Beton kırıkları, katmanlı beton numuneler, hesaplamalı modelleme, elektromanyetik dalga yayılımı, ZUSF; mikrodalga radar HMY.

YILDIZ TEKNİK ÜNİVERSİTESİ FEN BİLİMLERİ ENSTİTÜSÜ

# 1 INTRODUCTION

#### 1.1 Literature Review

Reinforced concrete structures wear over time. This deposition may be caused by a sudden change of state, such as earthquakes, as it can be gradually spreading over time. In both cases, it is important to determine the position and size of the wear, cracking or delamination before starting any repair, rehabilitation, and maintenance or improvement process [1-3]. Early detection of damage and cracks in concrete structures and infrastructures has great importance for public safety economically saves. The need for reliable non-destructive testing techniques increases with the aging of existing concrete structures and infrastructure and the importance of public safety and economic aspects. At the end of a certain period, the deterioration in concrete seriously affects the service life, safety and maintenance costs of concrete structures. Reinforced concrete structures require routine, precise and reliable monitoring [4, 5]. Non-destructive testing is carried out to periodically check the structural integrity of many concrete structures, such as bridge trays, plates, and tunnels. In the inspection of concrete structures with non-destructive testing, the integrity of the structure is not compromised, and the serviceability of the structure is not prevented since this inspection can be done in a short time Delamination and cracking constitute a large part of the concrete deterioration [6-8].

Nondestructive testing (NDT) techniques, which have been used for more than 30 years, are analysis techniques used in science and industry to evaluate the properties of a material, component or system without damaging the samples and destroying the integrity of the structure being tested. According to American Society of Nondestructive Testing (ASNT), NDT is the examination of the object without affecting its future usefulness, using technologies appropriate for the condition or structure of the substance to be examined. According to the basic principle of NDT, the inspection is performed by ensuring that a parameter of the sample and a

parameter of the method used are interacted without changing the quality and integrity of the sample to be examined [9, 10]. The main purpose of the NDT method is that the inspection is non-destructive and does not change the physical properties of the test object. In the non-destructive testing method, terms other than NDT are also used according to the information obtained from the test and the areas of use [11-13]. For example, if information is given about the process along with the test method, the term Nondestructive Evaluation (NDE) is used. Nondestructive Inspection (NDI) is used in areas other than process control. Nondestructive Characterization (NDC) is used to express the specific characterization of material properties, and Nondestructive Sensing (NDS) is used if sensors are used to obtain information from the sample inspected. There are many NDT techniques used to detect defects in the structures, such as acoustic, thermal, radiographic, microwave radar methods. In the following subsections current NDT techniques are reviewed [14, 15].

#### 1.1.1 Optical Methods

The optical non-destructive testing method uses optic waves, which are the range of electromagnetic waves visible to the human eye. Although the history of optical non-destructive testing methods is based on visual inspection, which is the oldest method, over time, techniques such as laser speckle metrology and machine visualization have been used with the development of technology. Optical spectrum includes visible wavelengths, these wavelengths vary from approximately 400nm to 700 nm, and frequency is between 750 THz and 428 THz. Classical optics are divided into two main branches as geometric optics and physical optics [16, 17]. In geometric optics, or ray optics, light is assumed to travel on straight lines. In physical optics, or wave optics, light is thought of as an electromagnetic wave.

In a homogeneous medium in regions free of current and charges, propagation of the light waves can be defined using the scalar wave equation.

$$\nabla^{2}V(\mathbf{r},t) - \frac{1}{c^{2}} \frac{\partial^{2}V(\mathbf{r},t)}{\partial t^{2}} = 0$$
 (1.1)

where  $\mathbf{r}(x, y, z)$  is a position vector of a point P in space and  $\mathbf{s}(s_x, s_y, s_z)$  a unit vector in a fixed direction. Any solution of (1.1) of the form  $V = V(\mathbf{r}, \mathbf{s}, t)$ , t is time and c is the speed of light waves in free space [18, 19].

There are various optical technologies that used in the assessment of the structures. These are small-scale optical fibre, optical heterodyne interferometry, infrared thermography, speckle technology that based on laser interferometry, endoscopic NDT technic based on optical measurements, terahertz (THz) technology.

In optical fiber technology, optical fibers are used to collect and detect the signal coming from the structure under examination, and it has a wide range of uses as it can be used to measure almost anything. Since optical fibers are a very light material, they can be easily attached to the surface or internal parts of the structure to be tested and can be used in every environment because they are resistant to environmental effects such as corrosion and electromagnetic waves. Certain properties of the light used in the examination, such as wavelength, density and polarization, affect the examination results [20, 21].

#### 1.1.2 Acoustic Emission

Compared to other NDE techniques, the acoustic emission (AE) method is one of the techniques that is difficult to apply practically, although it is based on simple physical concepts. Acoustic methods are non-destructive testing methods that use mechanical waves as body wave and surface wave to investigate the condition in the structures to be inspected [22-25].

Acoustic emission can be defined as the oscillation of transient elastic waves caused by the rapid redistribution of the stress in a material, that is, the wave used in the inspection is produced within the material itself. In the acoustic emission method, acoustic signals should be examined in order to detect the oscillation of sound waves and damage [26-29].

Since different AE sources can produce very different AE waveforms from each other, the emitted acoustic signal depends on the characteristics of the source. The ability to monitoring the volume of a region or material using a series of AE sensors, scanning in a short time and inexpensively, and continuing to use the structure or

material while scanning with the AE method are the advantages of the AE method. With the AE monitoring technique, evaluation of the damage progress of chemical industry materials and routine testing of pressure vessels can be performed. In addition to these, damage activity monitoring, damage location, damage mechanism identification, strength predictions can be performed by the AE emission [30].

#### 1.1.3 Ultrasound

Ultrasonic NDE is one of the most widely used NDE methods today. Ultrasonic waves are sound waves that can propagate in solid, liquid and gaseous environments and vibrate at a frequency too high to hear. The interaction of ultrasonic waves with solids in a non-destructive testing needs to be examined. Since the motion of ultrasonic waves in solid media can be expressed mathematically, generating ultrasonic waves and using transducers one can find the structure, thickness and flexibility of a solid material. Ultrasonic NDE has many applications in aircraft, tubing, semiconductor, manufacturing, rail, power and other industries [31-34].

Ultrasonic waves are waves that oscillate at a frequency above 20,000 Hertz and frequencies used in NDE applications range from approximately 50 kHz to several GHz. In contrast to electromagnetic waves, sound waves propagate faster in solids and slower in air, electromagnetic waves propagate optimally in a vacuum and minimally in solids. Properties of ultrasonic waves such as velocity and attenuation are used to characterize the density, elastic properties, composition, geometric properties or defects of a material [35-38].

In ultrasonic inspection, a transducer is placed in a sample and the voltage pulse is converted into an ultrasonic pulse (wave). After the pulse passes through the object and responds to its geometry and mechanical properties, it is either transmitted to another transducer (pitch-catch method) or reflected back to the original transducer (pulse-echo method). In both methods, the signal is converted back into an electrical pulse observed on an oscilloscope. With the help of the observed signal, the wave velocity or thickness within the sample, if there is a defect or delamination, its size, shape, location, if a layered medium is examined, the thickness of the layers can be displayed [39, 40].

#### 1.1.4 Magnetic Particle

Magnetic Particle Inspection (MPI) is the most appropriate NDE method that can be used when inspecting the defects on the surface or crack just below the surface of the ferromagnetic materials. In non-destructive examinations to be made with MPI; the magnetization method, the current type, the particle to be used is primarily to be wet or dry are the parameters that should be determined first. In the MPI method, the sample to be examined is magnetized and finely divided ferromagnetic particles are poured on the surface. If there is any defect on the surface of the inspected structure or in the areas close to the surface, magnetic particles can be attracted to the edges of these defects, as the magnetic field will be affected by these defects. Since the sample examined in the MPI method must be magnetized, it cannot be used in non-ferrous samples such as copper, brass, aluminum, titanium, but can be used in materials that are easy to magnetize [41, 42].

The advantages of the MPI method are as follows: it is very simple to use, but it is the most reliable method for detecting surface cracks, including very fine cracks, there is no limitation on the geometry of the part being tested and the shape of the crack, unlike the liquid penetrant method, if the crack is filled with any foreign material or the MPI method can be used even if the surface of the material under investigation is coated with paint. The disadvantages of the MPI method are as follows: it can only be used to detect surface or near-surface cracks and can only be used on ferromagnetic samples [43-45].

#### 1.1.5 Eddy Current

Using the eddy current (EC) NDT method, the positions of metal objects at different depths in concrete and soil environments such as walls and grounds can be determined. With the help of EC probes, the response of the examined material to electromagnetic waves at certain frequencies can be measured and using these measurements, the thickness of the material, its hardness, the presence of corrosion, whether the material is porosity and the presence of defects such as cracks can be interpreted. Since the electrical conductivity and magnetic properties are used in the EC non-destructive testing method, this method can be used in structures made of conductive materials such as metals and composite materials with low

conductivity. EC methods are also widely used in areas such as quality control, service integrity control, process control in the automotive and aircraft industries, research energy generation and maintenance. Thanks to the EC method, as in many other NDE methods, information such as geometry, conductivity and magnetic permeability of the examined sample is obtained [46-48].

The application areas of the EC method can be expressed as follows: the thickness of machined parts such as metallic foil, sheet and tube wall can be measured. In cases where the electromagnetic properties of the coating and the main material are different, the coating thickness can be measured. Material discontinuities such as cracks, seams, fractures and holes in plates and plates can be detected. Buried objects such as underground pipes, buried bombs and underground mines can be detected [49].

In eddy current method, conductive materials are examined by magnetic induction by using AC transformer as probe. In the EC method, the following steps are followed: excitation coil is stimulated by an AC signal, ferromagnetic or conductive material is brought near the probe to interact with the signal, a complete connection is established between the EC probe and the test sample. When the conductive material is released into the environment where the magnetic field is present, a current occurs, and these currents are called eddy currents since these currents generally go in a closed and circular path. Using the conductivity of a material, one can gain insight into the material's handling, hardness, and conductivity at temperature. Since eddy current technique is an electromagnetic method, the magnetic permeability property of the material affects the signal response. The response signals obtained in this method are displayed in the impedance plane and represent the impedance change in the start coil, although in different formats. The advantage of EC method over traditional ultrasonic method, penetrant method and magnetic particles is non-contact. It does not require any surface preparation. Its advantage over X-ray methods is its low cost. It gives fast results and is portable. Although sensitive to electromagnetic properties such as conductivity, there are no restrictions on geometric properties. Measurements can also be made at high temperatures. The most important disadvantage of this method is that the sample examined must be conductive. Since the signal response is not only due to discontinuities in the material but to all material properties, the obtained response can be difficult to interpret. It can only detect cracks on and near the surface [50, 51].

#### 1.1.6 Active Thermography

In this non-destructive testing technique, since the infrared imaging method is integrated with external heating and the sub-surface structure is tested, this method is called active thermography. Although there are thermal NDE techniques with different characteristics from each other, the methods using infrared cameras for measurements are generally called active thermography. The common features of all active thermography techniques can be listed as follows: the sample is heated by optical absorption, the inside of the sample is waited until it warms up, the temperature distribution on the surface of the sample is displayed using an infrared camera, the condition of the temperature distribution according to time and location is examined in order to interpret the material and geometric properties of the examined structure [52, 53].

In this technique, sub-surface defects can be detected by making use of the temperature difference between the material examined and the defect. Video recordings of surface temperature distribution are analyzed using infrared cameras. By expressing the change in surface temperature as a function of time, the subsurface structure of the sample is examined. The differences between the heating sources used to heat the sample cause the techniques used in active thermography to differ from each other. In all techniques used, after the sample is started to be heated with the help of a heat source, the change of surface temperature according to time and location is compared with an analytical model in every position measured by the camera. Thanks to active thermography, cracks, gaps, branching fractures in composite structures can be easily detected without contact [54-57].

#### 1.1.7 Liquid Penetrant

Penetrant testing (PT) is a simple, inexpensive and precise non-destructive testing method that allows the examination of discontinuities on the surfaces of a wide variety of materials, component parts and systems. These discontinuities on the material surfaces may be in the original materials or may be due to manufacturing processes or environmental factors. In order to detect any damage or fracture in the material by this method, it must have a relationship with the surface. The color of the liquid used in this method should be different from the color of the structure containing fractures. Just like a crack that one cannot normally see on the pavement can be seen after it is filled with dirty water. Compared to many other NDT methods, PT requires less mechanical skill [58, 59].

The most important things in this method are the cleanliness of the surface to be tested and the processing time. This method consists of two stages. First, the type of penetrant is determined, and then the time required for the penetrant to enter the defects in a word dwell time is determined. After the penetrant is applied and enough time has passed, the excess liquid is removed from the surface and then another material called developer is placed on the surface. The developer creates a contrasting background to make the penetrant easy to see.

The purpose of the PT method is to completely cover the sample surface of the penetrating liquid and then penetrate the depths of the discontinuities opening to the surface. Surface tension contact angle and surface wetting, capillarity and dwell time are the are the basic parameters of this method [60].

#### 1.1.8 Radiology

Radiographic techniques and especially X-rays are one of the few non-destructive testing methods that can visualize the interior of samples and are used without material discrimination. X-rays are electromagnetic waves that can be scattered, absorbed by materials, and can pass through materials that block visible light because of their high energy. While examining the sample, the interior of objects can be imaged depending on the amount of X-ray used, the thickness and density of the material. the X-ray is also used to determine the anatomical structure of the materials. X-rays are used in 1-dimensional imaging, 2-dimensional imaging called projection radiography, and 3-dimensional images called computed tomography. 2-dimensional X-ray imaging is one of the most common imaging methods used both

in the medical field and in the non-destructive examination of samples, using film as the image storage medium [61, 62].

The X-ray NDE method is easier to interpret the results than many other methods, as it reveals the picture of the sample under examination and clearly reveals the imaged object. This method can be used in a wide range of areas from people to engine blocks without material restrictions. It is a useful method for determining the components of the sample, examining the mass or bulk density, and measuring its thickness. It is also a suitable method for using internal features such as voids, branching fractures, porosity in cast materials. This method can be used in a wide range of areas from visualization of human limbs to inspection of reinforced concrete blocks without material discrimination. The main disadvantages of this method are that the radiation method poses a serious safety concern, the high voltage requirement to produce X-rays, and the use of protective materials and equipment. It is not suitable for all types of cracks detection; it has limitations in crack detection. Even if closed cracks have a finite opening, discontinuity detection can only be made in certain directions. It is difficult to detect surface imperfections using this method. People who will use this method must have high security awareness [63, 64].

#### 1.1.9 Microwave and Radar

Microwave nondestructive testing techniques were first introduced in the early 1960s and are extensively used in many areas from the 1990s to the present (Bahr, 1982). Microwave nondestructive testing technique started to develop later compared to other techniques and until very recently it was excluded from other non-destructive testing techniques [65-70].

Although the microwave NDT technique started to be used later than other techniques, it has developed very rapidly compared to other techniques and has achieved significant success especially in material characterization. Considering the constantly developing material technology, alternative lightning techniques are required instead of classical NDT approaches because lighter, stronger and more electrically insulating composites replace metals in many applications. Examination

of the dielectric materials such as ceramics, plastics and composites using microwave and millimeter wave is a new field of application in NDT [71-75].

As the first developed NDT techniques are used to examine metallic structures, they are insufficient for the recently produced composite materials. Microwaves can easily penetrate in dielectric materials [76, 77]. The depth at which information about a material can be obtained or the distance that the microwave can propagate depends on the loss factor of the dielectric material (the ability to absorb microwave energy), the operating frequency and the receiver sensitivity [78-80].

Microwave measurements may be carried out on one side or on both sides of a material and on contact or non-contact. Microwave NDT techniques can be used to examine the geometric and dimensional properties of an environment as well as defects can be examined. The measurement accuracy can be increased by using the polarization properties of the microwave in order to better visualize the defects in a particular area of the material being measured. It is also possible to evaluate the properties and composition of mixtures of chemically produced composites.

In an application, the smallest spatial distance between the two defects is considered to be resolution so that they can be perceived individually. Later, near-field microwave and millimeter wave techniques provided better resolutions than one-tenth of the wavelength, and in recent studies on microwave waves, better results than one fifty seconds of wavelength are obtained. This is because an open-ended waveguide aperture or lateral resolution in the near field of a probe, such as an open-ended coaxial line, is determined by the probe dimensions rather than the operating wavelength. Changes in the properties of the reflection coefficient for a given microwave sensor and its defect are very different in far field and near field conditions [81, 82].

Hardware systems for microwave NDT applications do not have to be expensive. If laboratory-testing equipment is used to make measurements, the cost is high. Besides, the hardware for a particular application can be developed and manufactured to be relatively cheap, simple in design, hand-held, battery-powered, operator-friendly and on-line. As the primary purpose of detecting defects in most microwave NDT applications is the primary purpose, complex post signal

processing is generally not needed. Large scanning areas can be achieved as scanning areas can be equipped with a range of sensors. Microwave signals could not penetrate inside the conductors and graphite composites, but this does not mean that metals and composite materials can never be investigated, metals and graphite composites can be examined by evaluating their properties such as thickness and material composition of dielectric coatings on the outer surfaces [83].

One of the most important features of microwave NDT techniques is that many different probes/sensors can be used. Some of these may give better results than others for a particular application. In addition, more precise results can be achieved by optimizing the system parameters in microwave NDT techniques. Once the theoretical basis for the interaction of microwaves with a given environment is understood and modeled, electromagnetic codes can be developed to estimate the result of a measurement to obtain the highest possible measurement accuracy [84]. Some of the areas that use the microwave NDT techniques are composite inspection,

Some of the areas that use the microwave NDT techniques are composite inspection, dielectric material characterization, microwave imaging, medical and industrial applications. With the help of microwave radar NDT method, thickness measurement of coatings, inspection of single-layer dielectric sheets, examination of layered dielectric composites made of plastic, ceramic, wood, gap detection in layered and half-space of dielectric composites, detection of delamination and dispersion, determination of dispersion depth of layered composite or a thick dielectric Delamination potential in the material, rust and corrosion detection in paint and thick layer laminate composite coatings, detection and evaluation of impact damage in reinforced composite structures [85, 86].

### 1.2 Objective of the Thesis

In this research, internal crack that cannot be detected from the outside and two different surface crack geometries are defined in concrete structures. In order to define the surface crack, rectangles of decreasing width and circles of the same radius moving one after another are used respectively in two different concrete samples. In the other concrete sample, crack type is defined different from the void that cannot be detected from the surface and very thin crack definition is made by using the Riemann integral region to express the concrete defects. In addition to the

definitions of cracks, the interaction of composite piles and layered structures with mortar, concrete and pavement on their surface with the microwave is investigated by preparing the simulation setups. FDTD modeling is performed in the center frequency of L (1.0-2.0 GHz), S (2.0-4.0 GHz) and C (4.0-8.0 GHz) bands for prepared simulation setups which are suitable for the defined cracks. In the FDTD calculations, the dispersivity of the concrete samples is also taken into account. The structures which have surface crack are measured with Vivaldi antenna array. The reflection and transmission coefficients obtained from the measurement results and FDTD calculations are compared.

#### 1.3 Hypothesis

Until today, studies on smooth geometries have been made, and have been limited to numerical simulations and laboratory measurements. In our study, the most appropriate modeling is made for the crack that can be encountered in real life. Complex structured concrete (concrete containing cracks, rebars, delaminations and voids) is simulated, these simulation models are physically poured into the mold in the construction laboratory, allowed to dry in the air for a long time (more than six months), then, concrete measurement is made in an anechoic chamber using electromagnetic waves and vivaldi antenna array. The results obtained from the measurement and the results obtained from the simulation are compared. Hypothesis: The measurement values of the simulated concrete structures and the samples poured into the mold suitable for these situations overlap with the simulation values. Therefore, it will be shown that it is possible to simulate the cases we have presented without the need for costly experimental studies.

### 1.4 Organization of the Dissertation

This thesis is organized and presented in the following manner.

**Chapter 2** reviews the finite difference time domain (FDTD) method. Basic facts and knowledge of electromagnetic methods and FDTD are illustrated. The advantages of the FDTD method and the reasons for its use in this thesis are briefly mentioned. By expressing Maxwell's equations and finite differences, the expression of Maxwell's curl equations with difference equations is given. The derivation of the update

equations to be used in simulations is explained in detail by using finite difference notation and Yee algorithm. In order to facilitate the calculation, the three-dimensional equations have been reduced to two dimensions and one dimension. Finally, the section is completed by mentioning the stability condition and numerical dispersion.

**Chapter 3** illustrates the source waveforms, absorbing boundary conditions and dielectric properties of concrete.

Chapter 4 shows crack types, layered concrete structures and cylindrical concretes. Three different types of cracks that can be encountered in a concrete structure have been identified. Surface cracks are defined with shrinking rectangles and dynamic geometry, and internal cracks, which cannot be observed from the outer surface, is defined by the Riemann integral definition. Simulation setups of six different layered rectangular structures with different building materials are prepared. Since nondestructive testing can be performed with microwave radar technique for concrete filled composite piles used in environments with very high humidity, simulations have also been made for cylindrical concretes and concrete filled composite piles. In the simulations, the field distributions from both the TEz mode and the TMz mode are compared and it is investigated which mode is more advantageous in which situations. Surface cracks, rebars, voids, and internal cracks are simulated at 1.5 GHz, 3.0 GHz and 6.0 GHz frequencies, and 2-D and 3-D cases of field distributions are given.

**Chapter 5** physical structure of the concrete specimens, dielectric properties of concrete and measurement setups, reflection and transmission coefficients. The WCR02 table is presented by expanding it to the frequencies we work with. The variation of dielectric properties according to the moisture content of the concrete is examined.

**Chapter 6** summarizes the results from this study and discusses possible research topics for future studies.

# NUMERICAL SIMULATION AND FINITE DIFFERENCE TIME DOMAIN METHOD

#### 2.1 Basic Facts and Knowledge

In the absence of the computer technology, electromagnetic problems are generally tried to be solved by analytical methods and if analytical methods are inadequate the problems are researched experimentally. With the advancement of computer technology, computational electromagnetics has developed rapidly over the past decade and has come to a state where extremely accurate predictions can be obtained for various electromagnetic problems such as the scattering cross section of radar targets, the sensitive design of antennas and microwave devices, which are among the most popular problems of today. Computational electromagnetic methods used in problems that cannot be solved analytically can be divided into two parts as differential equation methods and integral equation methods. In general, integral equation methods give approximate results in terms of finite sums, whereas differential equation methods give results in terms of finite differences [87].

In previous years, when studies in the time domain were not developed, most of the computational electromagnetic problems were carried out in the frequency domain where harmonic behavior was present. In real problem applications, frequency domain approaches are used since it is possible to compare the results obtained from the numerical solutions of the canonical problems with analytical solutions. In addition, the operation of the systems used to make measurements in the frequency domain has also led to the use of the frequency domain in problem solutions. Although frequency domain techniques have been used before time domain techniques, they have some difficulties. For example, scattering techniques that is used to electrically model the scattering properties of large and complex shapes do not work well when the material composition is non-metallic or more complex geometrically.

Integral equation methods are not affected by the content of the materials in the calculation domain and the complexity of the geometry, but since it will be necessary to solve high-dimensional linear equation systems, calculation space is needed. Differential equation methods used in computational electromagnetics have become more preferred in simulations because they do not contain complex mathematical formulas and are easier to encode. Differential equations time-domain approaches can be applied to many physical problems, as the computational resources are evolving and easy to adapt to simulation models that do not involve complex mathematical operations [88].

Maxwell's equations were solved numerically at first with the help of frequency domain integral equations, and then this research was developed, and direct time domain solutions of Maxwell's curl equations were made on spatial grids. Finite Difference Time Domain method first proposed by Yee in 1966 was the first technique used in the time domain and continued to be developed using it for new problems. FDTD method can solve Maxwell's equations without the need for complex asymptotic or Green function operations. Although it solves problems in the time domain, it works for very broad band frequencies using the Fourier transform [89].

The FDTD is a recursive method based on solving directly into the time space by replacing differential operators in time-dependent Maxwell equations with central finite difference equations. Thus, it allows the calculation of three electric field and three magnetic field components in time at certain discrete points of space. The FDTD method has second order accuracy in time and space, and the time steps must be selected according to the Courant stability criterion. Thus, the solution does not have amplitude errors (dissipative error) but due to geometric discretization, dispersive error exists in the solution.

FDTD method is useful for many problems such as photonic crystal based device modeling, electromagnetic band-gap-based device modeling, electromagnetic impact effects and analysis, radar performance analysis and radar cross-sectional area, interaction of biological tissues with electromagnetic wave, detection of medical diseases, electromagnetic wave propagation around the earth at low

frequencies, electromagnetic wave propagation in frequency dependent mediums, electromagnetic interference and compatibility analysis, classical and industrial electromagnetic device and system modeling. Because FDTD is a versatile modeling method, its results can be animated in MATLAB, Fortran, C ++ etc. In the FDTD method, both narrowband and broadband sources can be modeled [90-92].

#### 2.1.1 Electromagnetic Methods and FDTD

The first solution methods of Maxwell equations are based on frequency space solutions (sinusoidal steady state). Before 1960, closed form and infinite series based analytical solutions and numerical results are obtained with mechanical calculators. After 1960, high frequency asymptotic techniques and integral equation-based solutions are obtained thanks to electronic computers using programming languages such as Fortran. Sinusoidal types wave solutions have become widespread within this scope. The reasons for this are the mathematical effects of the Fourier theorem, the calculation of resonance frequencies, the spread of the solution of boundary value problems for the diffraction of waves at certain frequencies, electronic and communication technology based on single frequency carrier waves, sinusoidal waves in the nature. Sinusoidal-steady-state solutions can be obtained in general but studies on broadband and transient solutions are limited. In addition, for the problems encountered in the frequency space, electromagnetic wave scattering from complex geometry, non-metallic linear/nonlinear composite and large-scale structures numerical time space solutions have been proposed. The FDTD method is one of the most commonly used [89, 90].

#### 2.1.2 The Advantage of the FDTD

The FDTD does not use linear algebra. Therefore, there is no upper limit for the number of unknowns. There are solved problems until 10° unknowns. The FDTD offers a controllable solution. The solution is under control since the errors are well understood. Responds the impulse directly. Thus, it is possible to obtain a wideband pulse or sinusoidal steady state response in a single operation. Non-linear solutions are possible. It is possible to find non-linear responses of electromagnetic systems. Provides a systematic approach. It does not require new formulations, except for grid editing for different problems. For example, does not need to calculation of

Green function, potential etc. which is vary depending on the structure. Memory needs are solved. Nowadays, due to the developments in semiconductor technologies, memory problems required for FDTD have been solved with a high degree. Real-time imaging needs are solved. Today, due to the developments in semiconductor technologies, FDTD provides the opportunity to imaging the required field distribution. The number of publications related to FDTD is increasing every year because of the mentioned advantages. Thus, many new electromagnetic systems have been possible like digital systems, integrated optical applications etc. [89].

#### 2.1.3 The Dynamic Range of the FDTD

The FDTD algorithm developed for a problem needs to be examined in which boundaries and how accurately it produces results. The range of FDTD algorithms developed for a particular problem is the dynamic range that gives the best results in a given calculation region. According to this  $P_{\text{incident}}\left(Watt / m^2\right)$  is power of the incident wave and minimum observable scattered power is  $P_{\text{min scattered}}\left(Watt / m^2\right)$  and the dynamic range is defined as follows:

$$dynamic\ range = 10\log\left(\frac{P_{incident}\left(Watt/m^{2}\right)}{P_{\min.scattered}\left(Watt/m^{2}\right)}\right) \tag{2.1}$$

The main factors affecting the minimum observable scattered wave:

Errors due to the Absorbing Boundary Conditions (ABCs): Since the accuracy of reflection coefficients of Absorbing Boundary Conditions (ABCs) used in the 1980s is varying between -30 dB (3%) and -50 dB (0.3%), the dynamic range of the FDTD varies between almost 40-50 dB. But since 1994, the perfectly matched layer absorbing boundary conditions has been used instead of analytical boundary conditions, the accuracy can be achieved in terms of reflection coefficients at around -80 dB so the dynamic range of FDTD approaches almost 80 dB. Numerical dispersion errors (phase velocity anisotropy and non-homogenous gridding): As the dynamic range of the FDTD method is improved with the application of perfectly matched layer absorbing boundary conditions, the numerical dispersion errors can

be very big in electrically large-scale problems and consequently error rate is increasing as a result. As a solution to this situation, Multiresolution Time Domain (MRTD) and Pseudospetral Time Domain (PSTD) methods which have smaller numerical dispersion errors have been proposed [90].

#### 2.2 The Scalar Wave Equation and FDTD

#### 2.2.1 Propagating-Wave Solutions

In this section, the numerical FDTD solution of the most basic partial differential equation defining wave motion will be studied. After obtaining the analytical propagating wave solutions, the finite difference technique is applied to the wave equation and the numerical dispersion, numerical phase velocity, numerical stability and time step are examined.

In a source free region, the wave equation that governs either the electric of magnetic field in one dimension can be written below:

$$\frac{\partial^2 f(x,t)}{\partial x^2} - \mu \varepsilon \frac{\partial^2 f(x,t)}{\partial t^2} = 0$$
 (2.2)

where  $f(\omega) = f(x,t) = f(t \pm x/c)$  is a solution to this equation and provided that f is twice differentiable and  $c = 1/\sqrt{\mu\varepsilon}$ .

In here  $\frac{\partial \omega}{\partial t} = 1$ ,  $\frac{\partial \omega}{\partial x} = \pm \frac{1}{c}$  and the first derivatives of this function can be obtained via the chain rule.

$$\frac{\partial f(\omega)}{\partial t} = \frac{\partial f(\omega)}{\partial \omega} \frac{\partial \omega}{\partial t} = \frac{\partial f(\omega)}{\partial \omega}$$
(2.3)

$$\frac{\partial f(\omega)}{\partial x} = \frac{\partial f(\omega)}{\partial \omega} \frac{\partial \omega}{\partial x} = \pm \frac{1}{c} \frac{\partial f(\omega)}{\partial \omega}$$
(2.4)

The second derivatives can be obtained similarly using the chain rule

$$\frac{\partial}{\partial t} \left( \frac{\partial f(\omega)}{\partial t} \right) = \frac{\partial}{\partial t} \left( \frac{\partial f(\omega)}{\partial \omega} \right) = \frac{\partial^2 f(\omega)}{\partial \omega^2} \frac{\partial \omega}{\partial t} = \frac{\partial^2 f(\omega)}{\partial \omega^2}$$
(2.5)

$$\frac{\partial}{\partial x} \left( \frac{\partial f(\omega)}{\partial x} \right) = \frac{\partial}{\partial x} \left( \pm \frac{1}{c} \frac{\partial f(\omega)}{\partial \omega} \right) = \pm \frac{1}{c} \frac{\partial^2 f(\omega)}{\partial \omega^2} \frac{\partial \omega}{\partial x} = \frac{1}{c} \frac{\partial^2 f(\omega)}{\partial \omega^2}$$
(2.6)

As a result, (2.5) and (2.6) show that

$$\frac{\partial^2 f}{\partial t^2} = \frac{\partial^2 f}{\partial \omega^2} \tag{2.7}$$

$$\frac{\partial^2 f}{\partial x^2} = \frac{1}{c} \frac{\partial^2 f}{\partial \omega^2} \tag{2.8}$$

Substituting these into (2.2) yields

$$\frac{1}{c^2} \frac{\partial^2 f}{\partial \omega^2} - \frac{1}{c^2} \frac{\partial^2 f}{\partial \omega^2} = 0 \tag{2.9}$$

Since the two terms that satisfy the equation on the left side can be cancel. In here c represents the speed of light in free space. Using the permittivity and permeability of free space, c is obtained as  $c = 1/\sqrt{\varepsilon_0 \mu_0} \approx 3 \times 10^8 \, \text{m/s}$ . [89].

#### 2.2.2 Finite Differences

Numerical methods used in mathematical solutions are divided into Direct Methods (Gaussian Elimination, Numerical Integration) and Recursive Methods (Taylor Series). In the direct methods round-off errors can reach significant levels. according to this distinction the FDTD method is a recursive method. Accordingly, FDTD is based on determining the numerical equivalents of analytical derivatives of various degrees by expanding to the Taylor series of unknowns. While direct methods usually provide a solution with a certain number of computer operations, in recursive methods the number of computer operations is determined according to the convergence principle.

The finite difference method is divided into three as follows:

- Static Finite Difference (SFD)
   Laplace and Poisson Equation
   TEM (Transverse Electromagnetic) and Quasi TEM Equations
- 2. Finite Difference Frequency Domain (FDFD)

Helmholtz Equation

# Finite Difference Time Domain Wave Equation

Static finite difference and finite difference frequency domain do not provide time-based recursive solution. For this reason, only the matrix equation is obtained as a result of spatial discretization and this situation brings along the various disadvantages of the matrix equations. Since the entire FDTD solution is obtained recursively in time and in space, any matrix equation is not formed and the FDTD is distinguished from other finite difference techniques. Recursion is stopped when the problem is decided to be solved, the recursion is decided to be convergent, and the recursion is long enough. The basic errors that can be encountered in a recursive algorithm are the establishment of a mathematical model that is not sufficiently suitable for the physical model, data collection errors, truncation errors, inexact arithmetic usage and rounding errors [89].

Considering a Taylor's series expansion of  $f(x,t_n)$  about the space point  $x_i$  to the space point  $x_i + \Delta x$ , keeping time fixed at  $t_n$ ,

$$f(x_{i} + \Delta x)\Big|_{t_{n}} = f\Big|_{x_{i},t_{n}} + \Delta x \cdot \frac{\partial f}{\partial x}\Big|_{x_{i},t_{n}} + \frac{(\Delta x)^{2}}{2} \cdot \frac{\partial^{2} f}{\partial x^{2}}\Big|_{x_{i},t_{n}} + \frac{(\Delta x)^{3}}{6} \cdot \frac{\partial^{3} f}{\partial x^{3}}\Big|_{x_{i},t_{n}} + \frac{(\Delta x)^{4}}{24} \cdot \frac{\partial^{4} f}{\partial x^{4}}\Big|_{\xi_{i},t_{n}}$$

$$(2.10)$$

The last term here is known as the error term or remainder term.  $\xi_1$  is a space located somewhere in the interval  $(x_i, x_i + \Delta x)$ . Similarly, using the Taylor's series expansion to the space point  $x_i - \Delta x$ , and fixing time at  $t_n$ 

$$f(x_{i} - \Delta x)\Big|_{t_{n}} = f\Big|_{x_{i},t_{n}} - \Delta x \cdot \frac{\partial f}{\partial x}\Big|_{x_{i},t_{n}} + \frac{(\Delta x)^{2}}{2} \cdot \frac{\partial^{2} f}{\partial x^{2}}\Big|_{x_{i},t_{n}}$$

$$-\frac{(\Delta x)^{3}}{6} \cdot \frac{\partial^{3} f}{\partial x^{3}}\Big|_{x_{i},t_{n}} + \frac{(\Delta x)^{4}}{24} \cdot \frac{\partial^{4} f}{\partial x^{4}}\Big|_{\xi_{2},t_{n}}$$

$$(2.11)$$

In the remainder term,  $\xi_2$  is a space point located in the interval  $(x_i, x_i - \Delta x)$ . Considering together (2.10) and (2.11) one can be obtain,

$$f\left(x_{i}+\Delta x\right)\Big|_{t_{n}}+f\left(x_{i}-\Delta x\right)\Big|_{t_{n}}=2f\Big|_{x_{i},t_{n}}+\left(\Delta x\right)^{2}\cdot\frac{\partial^{2} f}{\partial x^{2}}\Big|_{x_{i},t_{n}}+\frac{\left(\Delta x\right)^{4}}{12}\cdot\frac{\partial^{4} f}{\partial x^{4}}\Big|_{\mathcal{E}_{2},t_{n}}$$
(2.12)

In here using the mean-value theorem,  $\xi_3$  is a space point that located in the interval  $(x_i - \Delta x, x_i + \Delta x)$ . By rearrangement of terms one can obtain

$$\left. \frac{\partial^2 f}{\partial x^2} \right|_{x_i, t_n} = \left( \frac{f(x_i + \Delta x) - 2f(x_i) + f(x_i - \Delta x)}{(\Delta x)^2} \right) \right|_t + O((\Delta x)^2)$$
(2.13)

Where  $O((\Delta x)^2)$  refers the remaining term. In order to reduce the error,  $\Delta x$  must approach zero. (2.13) is called as second order accurate, central difference approximation to the second partial derivative of f. After this i shows space position and n shows time observation point. (2.13) equation can be written more simply like this;

$$\left. \frac{\partial^{2} f}{\partial x^{2}} \right|_{x_{i}, t_{n}} = \frac{f_{i+1}^{n} - 2f_{i}^{n} + f_{i-1}^{n}}{\left(\Delta x\right)^{2}} + O\left(\left(\Delta x\right)^{2}\right)$$
 (2.14)

where  $f_i^n$  express a field that calculated at the space point  $x_i = i\Delta x$  and time point  $t_n = n\Delta t$  (2.14) express the central difference approximation, backward and forward approximations can be calculated similarly, and they are given (2.15) and (2.16) respectively.

$$\left. \frac{\partial^2 f}{\partial x^2} \right|_{x_i, t_n} = \frac{f_{i-2}^n - 2f_{i-1}^n + f_{i-2}^n}{\left(\Delta x\right)^2} + O\left(\left(\Delta x\right)^2\right)$$
 (2.15)

$$\left. \frac{\partial^2 f}{\partial x^2} \right|_{x_i, t_n} = \frac{f_{i+2}^n - 2f_{i+1}^n + f_i^n}{\left(\Delta x\right)^2} + O\left(\left(\Delta x\right)^2\right)$$
 (2.16)

For the second order partial time derivative  $x_i$  is accepted fixed and expand f in forward and backward Taylor's series in time. After that a second order accurate central difference approximation to the second partial time derivative of f [90].

$$\left. \frac{\partial^2 f}{\partial t^2} \right|_{x_i, t_n} = \frac{f_i^{n+1} - 2f_i^n + f_i^{n-1}}{\left(\Delta t\right)^2} + O\left(\left(\Delta t\right)^2\right)$$
 (2.17)

# 2.3 Maxwell's Curl Equations and FDTD

For modeling the electromagnetic event in any environment, the differential or integral states of Maxwell's equations are used in three dimensions. The time-dependent Maxwell's equations are given in differential and integral form

Gauss' law for the electric field:

$$\nabla.\mathbf{D}(\mathbf{r},t) = \rho_{e}(\mathbf{r},t) \tag{2.18}$$

$$\iint_{S} \mathbf{D}(\mathbf{r}, t) . \mathbf{ds} = \iiint_{V} \rho_{e}(\mathbf{r}, t) dv$$
(2.19)

Gauss' law for the magnetic field:

$$\nabla .\mathbf{B}(\mathbf{r},t) = \rho_h(\mathbf{r},t) \tag{2.20}$$

$$\iint_{S} \mathbf{B}(\mathbf{r},t).\mathbf{ds} = \iiint_{V} \rho_{h}(\mathbf{r},t) dv$$
(2.21)

Faraday's law:

$$\frac{\partial}{\partial t} \mathbf{B}(\mathbf{r}, t) = -\nabla \times \mathbf{E}(\mathbf{r}, t) - \mathbf{M}(\mathbf{r}, t)$$
(2.22)

$$\frac{\partial}{\partial t} \iint_{S} \mathbf{B}(\mathbf{r}, t) . \mathbf{ds} = -\oint_{t} \mathbf{B}(\mathbf{r}, t) . \mathbf{dl} - \iint_{S} \mathbf{B}(\mathbf{r}, t) . \mathbf{ds}$$
(2.23)

Ampere's law:

$$\frac{\partial}{\partial t} \mathbf{D}(\mathbf{r}, t) = \nabla \times \mathbf{H}(\mathbf{r}, t) - \mathbf{J}(\mathbf{r}, t)$$
(2.24)

$$\frac{\partial}{\partial t} \iint_{S} \mathbf{D}(\mathbf{r}, t) . d\mathbf{s} = -\oint_{I} \mathbf{H}(\mathbf{r}, t) . d\mathbf{l} - \iint_{S} \mathbf{J}(\mathbf{r}, t) . d\mathbf{s}$$
(2.25)

These equations can be expressed separately in all coordinate systems. In the FDTD algorithm only Faraday and Ampere laws are sufficient since Gauss' law is provided automatically in FDTD cells due to the location of  $\mathbf{E}(\mathbf{r},t)$  and  $\mathbf{H}(\mathbf{r},t)$ . Since the FDTD is a recursive algorithm,  $T = n_{total}.\Delta t$  express the duration time, where n is time step and  $\Delta t$  is time interval. Considering the  $f(\mathbf{r},t)|_{t=n\Delta t} = f(\mathbf{r},n\Delta t) = f^n(\mathbf{r})$  and  $\mathbf{M}(\mathbf{r},t) = 0$  the derivative of the equation (2.21) with respect to  $n\Delta t$  time can be expressed in the form of central differences and taking into account that electric fields are in exact steps and magnetic fields are in half time steps.

$$\nabla \times \mathbf{E}(\mathbf{r}, n) = -\frac{\partial}{\partial t} \mathbf{B}(\mathbf{r}, n) \Rightarrow \nabla \times \mathbf{E}^{n}(\mathbf{r}) \cong -\frac{\mathbf{B}^{n+1/2}(\mathbf{r}) - \mathbf{B}^{n-1/2}(\mathbf{r})}{\Delta t}$$
(2.26)

$$\mathbf{B}^{n+1/2}\left(\mathbf{r}\right) \cong \mathbf{B}^{n-1/2}\left(\mathbf{r}\right) - \Delta t \left[\nabla \times \mathbf{E}^{n}\left(\mathbf{r}\right)\right]$$
(2.27)

Similarly taking consideration the derivative the equation (2.24) at  $t = (n+1/2)\Delta t$  time step in the form of central differences

$$\nabla \times \mathbf{H}(\mathbf{r}, n+1/2) = \frac{\partial}{\partial t} \mathbf{D}(\mathbf{r}, n+1/2) + \mathbf{J}(\mathbf{r}, n+1/2)$$
(2.28)

$$\nabla \times \mathbf{H}^{n+1/2}\left(\mathbf{r}\right) \cong \frac{\mathbf{D}^{n+1}\left(\mathbf{r}\right) - \mathbf{D}^{n}\left(\mathbf{r}\right)}{\Delta t} + \mathbf{J}^{n+1/2}\left(\mathbf{r}\right)$$
(2.29)

$$\mathbf{D}^{n+1}(\mathbf{r}) \cong \mathbf{D}^{n}(\mathbf{r}) - \Delta t \left[ \mathbf{J}^{n+1/2}(\mathbf{r}) - \nabla \times \mathbf{H}^{n+1/2}(\mathbf{r}) \right]$$
 (2.30)

Since  $\mathbf{J}^{n+1/2}(\mathbf{r})$  shows the electrical current, using the interpolation  $\mathbf{D}^{n+1}(\mathbf{r})$  can be calculated as (2.31).

$$\mathbf{D}^{n+1}(\mathbf{r}) \cong \mathbf{D}^{n}(\mathbf{r}) - \Delta t \left[ \frac{\mathbf{J}^{n+1}(\mathbf{r}) - \mathbf{J}^{n}(\mathbf{r})}{2} - \nabla \times \mathbf{H}^{n+1/2}(\mathbf{r}) \right]$$
(2.31)

 $\mathbf{J}^{n+1}(\mathbf{r})$  and  $\mathbf{J}^{n}(\mathbf{r})$  can be calculated using  $\mathbf{J}(\mathbf{r},t)$ .

In linear, isotropic and nondispersive materials,  $\mathbf{D}$  is related to  $\mathbf{E}$  and  $\mathbf{B}$  is related to  $\mathbf{H}$  as follows:

$$\mathbf{D} = \varepsilon \mathbf{E} = \varepsilon_r \varepsilon_0 \mathbf{E}, \ \mathbf{B} = \mu \mathbf{H} = \mu_r \mu_0 \mathbf{H}$$
 (2.32)

The materials that accepted isotropic and nondispersive convert some of the  ${\bf E}$  and  ${\bf H}$  field into heat energy so some the  ${\bf E}$  and  ${\bf H}$  field fields attenuate. Note that  ${\bf J}$  and  ${\bf M}$  acts independent sources of E-field energy and H-field energy,  ${\bf J}_{source}$  and  ${\bf M}_{source}$ .

$$\mathbf{J} = \mathbf{J}_{source} + \sigma \mathbf{E}, \ \mathbf{M} = \mathbf{M}_{source} + \sigma^* \mathbf{H}$$
 (2.33)

 $\sigma$ : electric conductivity (Siemens/meter)

 $\sigma^*$ : equivalent magnetic loss (ohms/meter)

Equation (2.32) is substituted in Equ. (2.22) and Equ. (2.24) the equations, following equation is obtained.

$$\frac{\partial \mathbf{H}}{\partial t} = -\frac{1}{\mu} \nabla \times \mathbf{E} - \frac{1}{\mu} \left( \mathbf{M}_{source} + \sigma^* \mathbf{H} \right)$$
 (2.34)

$$\frac{\partial \mathbf{E}}{\partial t} = \frac{1}{\varepsilon} \nabla \times \mathbf{H} - \frac{1}{\varepsilon} (\mathbf{J}_{source} + \sigma \mathbf{E})$$
 (2.35)

Six scalar equations are obtained after the vector operators of Equ. (2.34) and (2.35) are written. When components of Equ. (2.34) and (2.35) are reformulated two decoupled groups of equations are obtained, and the decoupled equations are evaluated separately [89, 90].

$$\frac{\partial H_x}{\partial t} = \frac{1}{\mu} \left[ \frac{\partial E_y}{\partial z} - \frac{\partial E_z}{\partial y} - \left( M_{source_x} + \sigma^* H_x \right) \right]$$
 (2.36)

$$\frac{\partial H_{y}}{\partial t} = \frac{1}{\mu} \left[ \frac{\partial E_{z}}{\partial x} - \frac{\partial E_{x}}{\partial z} - \left( M_{source_{y}} + \sigma^{*} H_{y} \right) \right]$$
 (2.37)

$$\frac{\partial H_z}{\partial t} = \frac{1}{\mu} \left[ \frac{\partial E_x}{\partial y} - \frac{\partial E_y}{\partial x} - \left( M_{source_z} + \sigma^* H_z \right) \right]$$
 (2.38)

For the Equ. (2.35)

$$\frac{\partial E_x}{\partial t} = \frac{1}{\varepsilon} \left[ \frac{\partial H_z}{\partial y} - \frac{\partial H_y}{\partial z} - \left( J_{source_x} + \sigma E_x \right) \right]$$
 (2.39)

$$\frac{\partial E_{y}}{\partial t} = \frac{1}{\varepsilon} \left[ \frac{\partial H_{x}}{\partial z} - \frac{\partial H_{z}}{\partial x} - \left( J_{source_{y}} + \sigma E_{y} \right) \right]$$
 (2.40)

$$\frac{\partial E_z}{\partial t} = \frac{1}{\varepsilon} \left[ \frac{\partial H_y}{\partial x} - \frac{\partial H_x}{\partial y} - \left( J_{source_z} + \sigma E_z \right) \right]$$
 (2.41)

The partial differential equation systems in (2.36) -(2.38) and (2.39) -(2.41) are the basis of the FDTD algorithm used for electromagnetic wave interactions with three-dimensional objects [90].

### 2.3.1 Reduction to Two Dimensions (2D)

Considering that the structure to be simulated using the FDTD extends to infinity in the z-direction without a change in shape or position and the incident wave is uniform in the z direction, then all the derivatives with respect to z is equal to zero or  $\partial/\partial z = 0$ . As a result, all the equations defined in Equ. (2.36) and Equ. (2.39) are reduced to 2-D.

$$\frac{\partial H_x}{\partial t} = \frac{1}{\mu} \left[ -\frac{\partial E_z}{\partial y} - \left( M_{source_x} + \sigma^* H_x \right) \right]$$
 (2.42)

$$\frac{\partial H_{y}}{\partial t} = \frac{1}{\mu} \left[ \frac{\partial E_{z}}{\partial x} - \left( M_{source_{y}} + \sigma^{*} H_{y} \right) \right]$$
 (2.43)

$$\frac{\partial H_z}{\partial t} = \frac{1}{\mu} \left[ \frac{\partial E_x}{\partial y} - \frac{\partial E_y}{\partial x} - \left( M_{source_z} + \sigma^* H_z \right) \right]$$
 (2.44)

$$\frac{\partial E_x}{\partial t} = \frac{1}{\varepsilon} \left[ \frac{\partial H_z}{\partial y} - \left( J_{source_x} + \sigma E_x \right) \right]$$
 (2.45)

$$\frac{\partial E_{y}}{\partial t} = \frac{1}{\varepsilon} \left[ -\frac{\partial H_{z}}{\partial x} - \left( J_{source_{y}} + \sigma E_{y} \right) \right]$$
 (2.45)

$$\frac{\partial E_z}{\partial t} = \frac{1}{\varepsilon} \left[ \frac{\partial H_y}{\partial x} - \frac{\partial H_x}{\partial y} - \left( J_{source_z} + \sigma E_z \right) \right]$$
 (2.47)

Grouping the Equ. (2.42) –(2.44) and Equ. (2.45) –(2.47) two equations groups are obtained. These are TE or HH-polarized waves which contains  $E_x$ ,  $E_y$ ,  $H_z$  component and TM or VV-polarized waves which contains  $H_x$ ,  $H_y$ ,  $E_z$  components.

Transverse magnetic mode with respect to z in two dimensions that is to say  $TM_z$  mode:

$$\frac{\partial H_x}{\partial t} = \frac{1}{\mu} \left[ -\frac{\partial E_z}{\partial y} - \left( M_{source_x} + \sigma^* H_x \right) \right]$$
 (2.48)

$$\frac{\partial H_{y}}{\partial t} = \frac{1}{\mu} \left[ \frac{\partial E_{z}}{\partial x} - \left( M_{source_{y}} + \sigma^{*} H_{y} \right) \right]$$
 (2.49)

$$\frac{\partial E_z}{\partial t} = \frac{1}{\varepsilon} \left[ \frac{\partial H_y}{\partial x} - \frac{\partial H_x}{\partial y} - \left( J_{source_z} + \sigma E_z \right) \right]$$
 (2.50)

Transverse electric- mode with respect to z in two dimensions that is to say  $TE_z$  mode:

$$\frac{\partial E_x}{\partial t} = \frac{1}{\varepsilon} \left[ \frac{\partial H_z}{\partial y} - \left( J_{source_x} + \sigma E_x \right) \right]$$
 (2.51)

$$\frac{\partial E_{y}}{\partial t} = \frac{1}{\varepsilon} \left[ -\frac{\partial H_{z}}{\partial x} - \left( J_{source_{y}} + \sigma E_{y} \right) \right]$$
 (2.52)

$$\frac{\partial H_z}{\partial t} = \frac{1}{\mu} \left[ \frac{\partial E_x}{\partial y} - \frac{\partial E_y}{\partial x} - \left( M_{source_z} + \sigma^* H_z \right) \right]$$
 (2.53)

Neither TM nor TE mode does not contain common vector components. Therefore, these modes may be existing simultaneously in any environment without any interactions. These modes are two possibilities that can occur if the partial derivative of the electromagnetic wave interaction problem in the z direction is equal to zero. These two modes are very different each other in physically. This is due to the positioning of the E and H field lines relative to the surface of the modeled

structure. The TEz mode creates E-field lines in a plane perpendicular to the z-axis with infinite length while the TMz mode sets up only E-field lines parallel to the z-axis [89, 90].

## 2.3.2 Reduction to One Dimensions (1D)

Assuming that both electromagnetic field excitation and the structure that is modeled has not have any variation in the y-direction. It is assumed that all domain partial derivatives are equal to zero for both y and z, and that the interaction structure consists of an infinite space with a possible material layer in the x direction.

After that the two-dimensional  $TM_z$  mode expressed by Maxwell's equations (2.48) –(2.50) is reduced to the following form:

$$\frac{\partial H_x}{\partial t} = \frac{1}{\mu} \left[ -\left( M_{source_x} + \sigma^* H_x \right) \right] \tag{2.54}$$

$$\frac{\partial H_{y}}{\partial t} = \frac{1}{\mu} \left[ \frac{\partial E_{z}}{\partial x} - \left( M_{source_{y}} + \sigma^{*} H_{y} \right) \right]$$
 (2.55)

$$\frac{\partial H_z}{\partial t} = \frac{1}{\mu} \left[ \frac{\partial E_x}{\partial y} - \frac{\partial E_y}{\partial x} - \left( M_{source_z} + \sigma^* H_z \right) \right]$$
 (2.56)

Considering that  $M_{source_x} = 0$  for all time and  $H_x = 0$  at t = 0 time step and as a result  $\partial H_x/\partial t = 0$  at t = 0 time step. In this case the terms containing  $H_x$  in Equ. (2.54) – (2.56) are vanish and x-directed, z-polarized transverse electromagnetic (TEM) in one dimension is obtained as follows:

$$\frac{\partial H_{y}}{\partial t} = \frac{1}{\mu} \left( \frac{\partial E_{z}}{\partial x} - \left( M_{source_{y}} + \sigma^{*} H_{y} \right) \right)$$
 (2.57)

$$\frac{\partial E_z}{\partial t} = \frac{1}{\varepsilon} \left( \frac{\partial H_y}{\partial x} - \left( J_{source_z} + \sigma E_z \right) \right)$$
 (2.58)

The two-dimensional  $TE_z$  mode expressed by Maxwell's equations (2.51) –(2.53) is reduced to the following form:

$$\frac{\partial E_x}{\partial t} = \frac{1}{\varepsilon} \left[ -\left( J_{source_x} + \sigma E_x \right) \right]$$
 (2.59)

$$\frac{\partial E_{y}}{\partial t} = \frac{1}{\varepsilon} \left[ -\frac{\partial H_{z}}{\partial x} - \left( J_{source_{y}} + \sigma E_{y} \right) \right]$$
 (2.60)

$$\frac{\partial H_z}{\partial t} = \frac{1}{\mu} \left[ -\frac{\partial E_y}{\partial x} - \left( M_{source_z} + \sigma^* H_z \right) \right]$$
 (2.61)

Considering that  $J_{source_x} = 0$  for all time and  $E_x = 0$  at t = 0 time step and as a result  $\partial E_x/\partial t = 0$  at t = 0 time step. In this case the terms containing  $E_x$  in Equ. (2.59) – (2.61) are vanish and x-directed, y-polarized transverse electromagnetic (TEM) in one dimension is obtained as follows [90]:

$$\frac{\partial E_{y}}{\partial t} = \frac{1}{\varepsilon} \left( -\frac{\partial H_{z}}{\partial x} - \left( J_{source_{y}} + \sigma E_{y} \right) \right)$$
 (2.62)

$$\frac{\partial H_z}{\partial t} = \frac{1}{\mu} \left( -\frac{\partial E_y}{\partial x} - \left( M_{source_z} + \sigma^* H_z \right) \right)$$
 (2.63)

### 2.3.3 Equivalence to the Wave Equation in One Dimension

Assuming that the one-dimensional x-directed, z-polarized TEM mode given in (2.57) and (2.58). From this equation considering the  $M_{source_y} = J_{source_z} = 0$  and  $\sigma^* = \sigma = 0$  one can obtain homogeneous, lossless, one-dimensional scalar wave equation for  $H_y$ . Taking the partial time derivative of (2.57),

$$\frac{\partial}{\partial t} \left( \frac{\partial H_{y}}{\partial t} = \frac{1}{\mu} \cdot \frac{\partial E_{z}}{\partial x} \right) \rightarrow \frac{\partial^{2} H_{y}}{\partial t^{2}} = \frac{1}{\mu} \cdot \frac{\partial^{2} E_{z}}{\partial t \partial x}$$
 (2.64)

and taking the partial space derivative of (2.58),

$$\frac{\partial}{\partial x} \left( \frac{\partial E_z}{\partial t} = \frac{1}{\varepsilon} \cdot \frac{\partial H_y}{\partial x} \right) \to \frac{\partial^2 E_z}{\partial x \partial t} = \frac{1}{\varepsilon} \cdot \frac{\partial^2 H_y}{\partial x^2}$$
 (2.65)

Substituting the *x-t* derivative of  $E_z$  in (2.65) into the *t-x* derivative of  $E_z$  in (2.64) one can obtain:

$$\frac{\partial^2 H_y}{\partial t^2} = \frac{1}{\mu} \cdot \frac{1}{\varepsilon} \cdot \frac{\partial^2 H_y}{\partial x^2} = c^2 \frac{\partial^2 H_y}{\partial x^2}$$
 (2.66)

where  $c = 1/\sqrt{\mu\varepsilon}$ , (2.66) is a one-dimensional scalar wave equation for  $H_y$ .

Taking the partial time derivative of (2.58) and considering the  $M_{source_y}=J_{source_z}=0$  and  $\sigma^*=\sigma=0$  one can obtain homogeneous, lossless, one-dimensional scalar wave equation for  $E_z$ .

$$\frac{\partial}{\partial t} \left( \frac{\partial E_z}{\partial t} = \frac{1}{\varepsilon} \cdot \frac{\partial H_y}{\partial x} \right) \to \frac{\partial^2 E_z}{\partial t^2} = \frac{1}{\varepsilon} \cdot \frac{\partial^2 H_y}{\partial t \partial x}$$
 (2.67)

and taking the partial space derivative of (2.57):

$$\frac{\partial}{\partial x} \left( \frac{\partial H_{y}}{\partial t} = \frac{1}{\mu} \cdot \frac{\partial E_{z}}{\partial x} \right) \rightarrow \frac{\partial^{2} H_{y}}{\partial x \partial t} = \frac{1}{\mu} \cdot \frac{\partial^{2} E_{z}}{\partial x^{2}}$$
 (2.68)

Substituting the *x-t* derivative of  $H_y$  in (2.68) into the *t-x* derivative of  $H_y$  in (2.67) one can obtain:

$$\frac{\partial^2 E_z}{\partial t^2} = \frac{1}{\varepsilon} \cdot \frac{1}{u} \cdot \frac{\partial^2 E_z}{\partial x^2} = c^2 \frac{\partial^2 E_z}{\partial x^2}$$
 (2.69)

where  $c=1/\sqrt{\mu\varepsilon}$  , (2.69) is a one-dimensional scalar wave equation for  $E_z$  .

# 2.4 Finite Difference Time Domain Solution and Yee's Algorithm

The basis of the Yee algorithm is very robust and still has great usability. Instead of solving the wave equation for only electric field and magnetic field, a solution is obtained for the electric and magnetic fields by time and space discretization using the Maxwell curl equations combined with the Yee algorithm. As both E and H information is used to solve the problem, a better result is obtained in large scale problems. Both the electrical and magnetic material properties can be modeled easily. The Yee algorithm centers E and H components in time according to a leapfrog arrangement. Using the previously stored H data, all E calculations in the area are completed and memorized for a given time point. Then, using the calculated

E data, the H calculations in the space are completed and stored in memory. Recalculating components E using the most recently obtained H data, the cycle starts again. The leapfrog time-stepping algorithm is explicit so that problems with simultaneous equations and matrix inversion are avoided [90].

#### 2.4.1 Finite Differences and Notation

Considering that the problem is defined as a grid in the cartesian coordinates with  $N = (N_x, N_y, N_z)$  and  $\mathbf{r} = \mathbf{r}(i\Delta x, j\Delta y, k\Delta z) = \mathbf{r}(i, j, k)$ 

$$f(r,t)\Big|_{t=n\Delta t} = f(i\Delta x, j\Delta y, k\Delta z, n\Delta t) = f^{n}(i, j, k)$$
(2.70)

Equ. (2.70) can be taken as the fundamental of the Yee notation. According to the discretization given above (2.70),  $\mathbf{E}^{n}(\mathbf{r})$  and  $\mathbf{H}^{n+1/2}(\mathbf{r})$  values must be calculated at the same time. In this context,  $\mathbf{H}^{n+1/2}(\mathbf{r})$  expressions that are half a step ahead in time should be offset in position according to the formula  $position = speed \times time$ .

Accordingly, each small cubic cell is called a FDTD cell or unit Yee cell. Each unit Yee cell has three electric and three magnetic field components with different intracellular locations. The electric field components are in the middle of the cell surfaces while the magnetic field components are in the middle of the cell's edge lines.

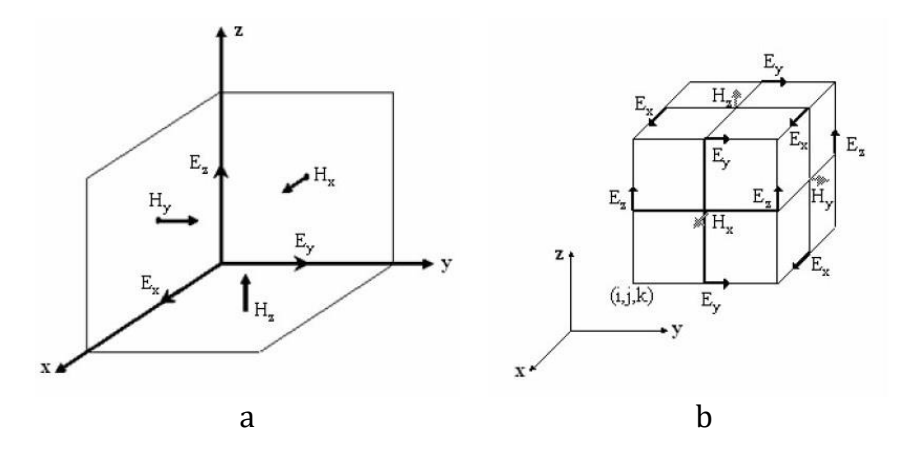


Figure 2.1 (a) Unit Yee Cell (b) FDTD Space [90]

Due to the difference in the position of the electric field and magnetic field in the cell, the time step values automatically differ from each other by  $\Delta t/2$ .

In the FDTD method the problem space consists of  $(N_x \times N_y \times N_z)$  pieces of rectangular cubic cells as Figure 2.1. The FDTD method is first given in Cartesian coordinates, and it must provide three fundamental conditions. In this coordinate system, the computational space boundary must be sufficiently far from the scattering surface (at least 1– 2 wavelength), unit cells must have at least  $\lambda/10$  dimensions, and provide the stability criterion [89].

#### 2.4.2 FDTD Updating Equations for Three-Dimensional Problems

To achieve the numerical approximation of the Maxwell's curl equations in three dimensions given by (2.39) –(2.40) and (2.42) –(2.44) can be expressed as discrete equations in both space and time.

Taking consideration

$$\frac{\partial E_x}{\partial t} = \frac{1}{\varepsilon} \left[ \frac{\partial H_z}{\partial y} - \frac{\partial H_y}{\partial z} - \left( J_{source_x} + \sigma E_x \right) \right]$$
 (2.39)

Considering central difference for the time and space derivatives with the location of  $E_x(i, j, k)$  approximate value of the derivatives in (2.37a) can be calculated.

$$\frac{E_{x}^{n+1}(i,j,k) - E_{x}^{n}(i,j,k)}{\Delta t} = \frac{1}{\varepsilon(i,j,k)} \frac{H_{z}^{n+1/2}(i,j,k) - H_{z}^{n+1/2}(i,j-1,k)}{\Delta y} - \frac{1}{\varepsilon(i,j,k)} \frac{H_{y}^{n+1/2}(i,j,k) - H_{y}^{n+1/2}(i,j,k-1)}{\Delta z} - \frac{\sigma(i,j,k)}{\varepsilon(i,j,k)} E_{x}^{n+1/2}(i,j,k) - \frac{1}{\varepsilon(i,j,k)} J_{source_{x}}^{n+1/2}(i,j,k)$$
(2.71)

Although the components of the electric field are defined at integer time steps in the finite difference algorithm, on the right side of Equ. (2.71) the electric field component is defined at semi-integer time step. The  $E_x^{n+1/2}(i,j,k)$  can be written as the average of the  $E_x^{n+1}(i,j,k)$  and  $E_x^n(i,j,k)$  as follows.

$$E_x^{n+1/2}(i,j,k) = \frac{E_x^{n+1}(i,j,k) + E_x^n(i,j,k)}{2}$$
 (2.72)

Substituting the (2.72) in (2.71) and after some mathematical manipulations updating equation of the electric field for the next step can be calculated using the values of the magnetic field components, the source component, and the electric field component from the previous time step. The field positions of  $E_x$  are indicated in Figure 2.2.

$$\frac{2\varepsilon(i,j,k) + \Delta t.\sigma(i,j,k)}{2\varepsilon(i,j,k)} E_x^{n+1}(i,j,k) = \frac{2\varepsilon(i,j,k) + \Delta t.\sigma(i,j,k)}{2\varepsilon(i,j,k)} E_x^{n}(i,j,k) + \frac{\Delta t}{\varepsilon(i,j,k)\Delta y} \left(H_z^{n+1/2}(i,j,k) - H_z^{n+1/2}(i,j-1,k)\right) \quad (2.73)$$

$$-\frac{\Delta t}{\varepsilon(i,j,k)} J_{source_x}^{n+1/2}(i,j,k)$$

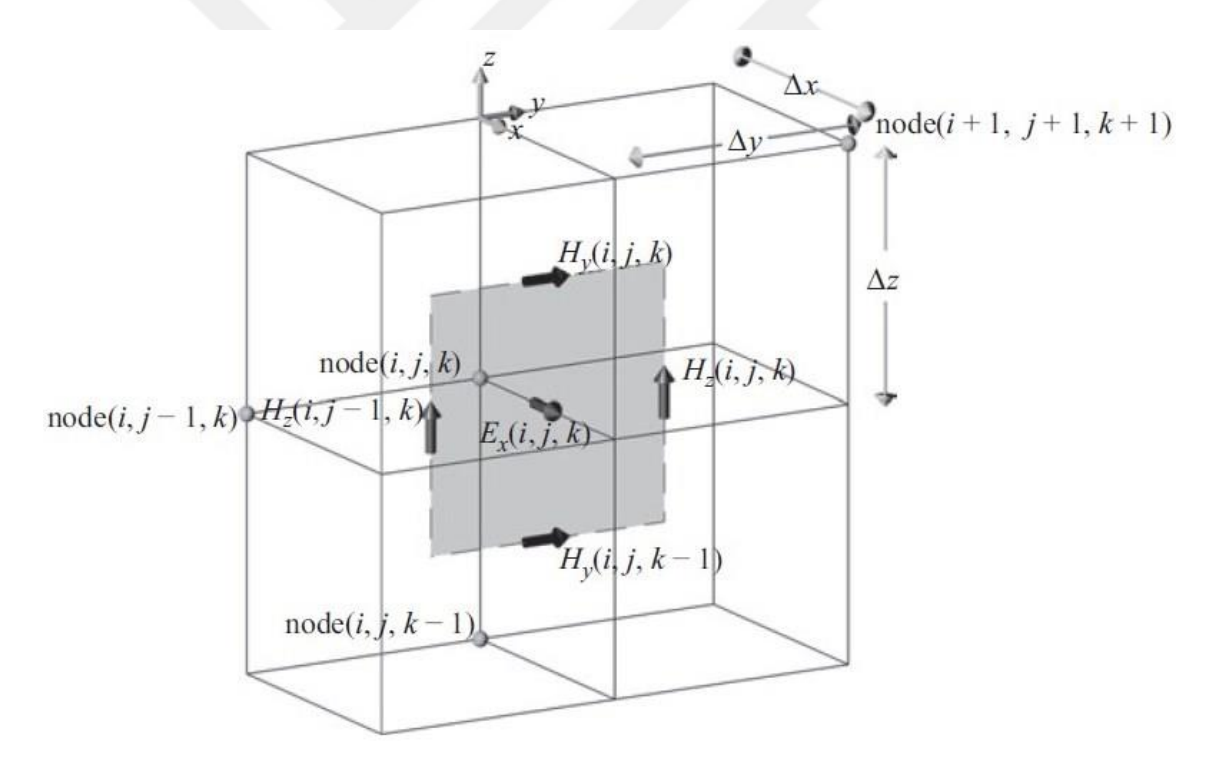


**Figure 2.2** Field Components for Calculation of the  $E_x(i,j,k)$  [89]

$$E_{x}^{n+1}(i,j,k) = \frac{2\varepsilon(i,j,k) - \Delta t.\sigma(i,j,k)}{2\varepsilon(i,j,k) + \Delta t.\sigma(i,j,k)} E_{x}^{n}(i,j,k) + \frac{2\Delta t}{(2\varepsilon(i,j,k) + \Delta t.\sigma(i,j,k))\Delta y} (H_{z}^{n+1/2}(i,j,k) - H_{z}^{n+1/2}(i,j-1,k)) - \frac{2\Delta t}{(2\varepsilon(i,j,k) + \Delta t.\sigma(i,j,k))\Delta z} (H_{y}^{n+1/2}(i,j,k) - H_{z}^{n+1/2}(i,j,k-1)) - \frac{2\Delta t}{2\varepsilon(i,j,k) + \Delta t.\sigma(i,j,k)} J_{source_{x}}^{n+1/2}(i,j,k) - H_{z}^{n+1/2}(i,j,k-1)$$

$$(2.74)$$

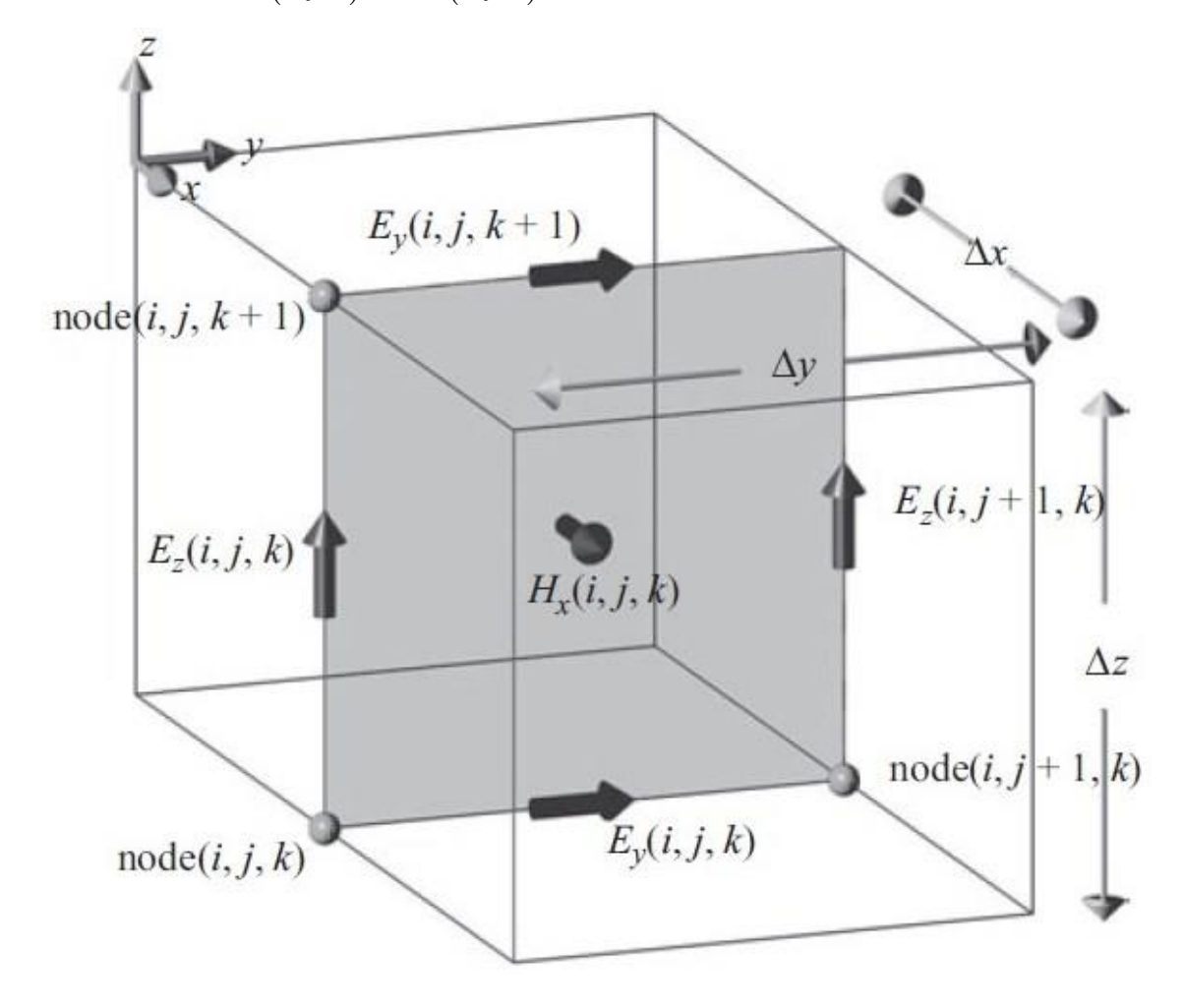


**Figure 2.3** Field Components for Calculation of the  $H_{x}(i,j,k)$  [89]

Similar to the method used to derive the electric field equations, update equations can be obtained in semi-integer time steps for the magnetic field components according to the field locations expressed in Figure 2.3.

After discretization of the (2.36) in space and time finite difference formula for

$$\frac{\partial H_x}{\partial t} = \frac{1}{\mu} \left[ \frac{\partial E_y}{\partial z} - \frac{\partial E_z}{\partial y} - \left( M_{source_x} + \sigma^* H_x \right) \right]$$
 (2.36)

 $H_z^{n+1/2}(i,j,k)$  can be obtained as follows.

$$\frac{H_{x}^{n+1/2}(i,j,k) - H_{x}^{n-1/2}(i,j,k)}{\Delta t} = \frac{1}{\mu(i,j,k)} \frac{E_{y}^{n}(i,j,k+1) - E_{y}^{n}(i,j,k)}{\Delta y} - \frac{1}{\mu(i,j,k)} \frac{E_{z}^{n}(i,j+1,k) - E_{z}^{n}(i,j,k)}{\Delta y} - \frac{1}{\mu(i,j,k)} H_{x}^{n}(i,j,k) - \frac{1}{\mu(i,j,k)} M_{source_{x}}^{n}(i,j,k)$$
(2.75)

Using some mathematical manipulations, the future term is written as follows:

$$H_{x}^{n+1/2}(i,j,k) = \frac{2\mu(i,j,k) - \Delta t.\sigma^{*}(i,j,k)}{2\mu(i,j,k) + \Delta t.\sigma^{*}(i,j,k)} H_{x}^{n-1/2}(i,j,k) + \frac{2\Delta t}{\left(2\mu(i,j,k) + \Delta t.\sigma^{*}(i,j,k)\right)\Delta z} \left(E_{y}^{n}(i,j,k+1) - E_{y}^{n}(i,j,k)\right) - \frac{2\Delta t}{\left(2\mu(i,j,k) + \Delta t.\sigma^{*}(i,j,k)\right)\Delta y} \left(E_{z}^{n}(i,j+1,k) - E_{y}^{n}(i,j,k)\right) - \frac{2\Delta t}{2\mu(i,j,k) + \Delta t.\sigma^{*}(i,j,k)} M_{source_{x}}^{n}(i,j,k)$$
(2.76)

Using the coefficient terms expressed below, the FDTD update equations for all components of the electromagnetic field equations can be written in the compact form.

$$E_{x}^{n+1}(i,j,k) = C_{exe}(i,j,k) \times E_{x}^{n}(i,j,k) + C_{exhz}(i,j,k) \times (H_{z}^{n+1/2}(i,j,k) - H_{z}^{n+1/2}(i,j-1,k)) + C_{exhy}(i,j,k) \times (H_{y}^{n+1/2}(i,j,k) - H_{y}^{n+1/2}(i,j,k-1)) + C_{exj}(i,j,k) \times J_{source}^{n+1/2}(i,j,k)$$

$$(2.77)$$

where

$$C_{exe}(i,j,k) = \frac{2\varepsilon(i,j,k) - \Delta t.\sigma(i,j,k)}{2\varepsilon(i,j,k) + \Delta t.\sigma(i,j,k)}$$
(2.78)

$$C_{exhz}(i,j,k) = \frac{2\Delta t}{\left(2\varepsilon(i,j,k) + \Delta t.\sigma(i,j,k)\right)\Delta y}$$
(2.79)

$$C_{exhy}(i,j,k) = -\frac{2\Delta t}{\left(2\varepsilon(i,j,k) + \Delta t.\sigma(i,j,k)\right)\Delta z}$$
(2.80)

$$C_{exj}(i,j,k) = -\frac{2\Delta t}{2\varepsilon(i,j,k) + \Delta t.\sigma(i,j,k)}$$
(2.81)

The FDTD updating equations for  $E_y^{n+1}(i, j, k)$ :

$$\frac{\partial E_{y}}{\partial t} = \frac{1}{\varepsilon} \left[ \frac{\partial H_{x}}{\partial z} - \frac{\partial H_{z}}{\partial x} - \left( J_{source_{y}} + \sigma E_{y} \right) \right]$$
 (2.40)

$$E_{y}^{n+1}(i,j,k) = C_{eye}(i,j,k) \times E_{y}^{n}(i,j,k) + C_{eyhx}(i,j,k) \times (H_{x}^{n+1/2}(i,j,k) - H_{x}^{n+1/2}(i,j,k-1)) + C_{eyhz}(i,j,k) \times (H_{z}^{n+1/2}(i,j,k) - H_{z}^{n+1/2}(i-1,j,k)) + C_{eyj}(i,j,k) \times J_{source_{y}}^{n+1/2}(i,j,k)$$

$$(2.82)$$

where

$$C_{eye}(i,j,k) = \frac{2\varepsilon(i,j,k) - \Delta t.\sigma(i,j,k)}{2\varepsilon(i,j,k) + \Delta t.\sigma(i,j,k)}$$
(2.83)

$$C_{eyhx}(i,j,k) = \frac{2\Delta t}{(2\varepsilon(i,j,k) + \Delta t.\sigma(i,j,k))\Delta z}$$
(2.84)

$$C_{exhz}(i,j,k) = -\frac{2\Delta t}{\left(2\varepsilon(i,j,k) + \Delta t.\sigma(i,j,k)\right)\Delta x}$$
(2.85)

$$C_{eyj}(i,j,k) = -\frac{2\Delta t}{2\varepsilon(i,j,k) + \Delta t.\sigma(i,j,k)}$$
(2.86)

The FDTD updating equations for  $E_z^{n+1}(i, j, k)$ :

$$E_{z}^{n+1}(i,j,k) = C_{eze}(i,j,k) \times E_{z}^{n}(i,j,k) + C_{ezhy}(i,j,k) \times (H_{y}^{n+1/2}(i,j,k) - H_{y}^{n+1/2}(i-1,j,k)) + C_{ezhx}(i,j,k) \times (H_{x}^{n+1/2}(i,j,k) - H_{x}^{n+1/2}(i,j-1,k)) + C_{ezj}(i,j,k) \times J_{source}^{n+1/2}(i,j,k)$$

$$(2.87)$$

where

$$C_{eze}(i,j,k) = \frac{2\varepsilon(i,j,k) - \Delta t.\sigma(i,j,k)}{2\varepsilon(i,j,k) + \Delta t.\sigma(i,j,k)}$$
(2.88)

$$C_{ezhy}(i,j,k) = \frac{2\Delta t}{\left(2\varepsilon(i,j,k) + \Delta t.\sigma(i,j,k)\right)\Delta x}$$
(2.89)

$$C_{ezhx}(i,j,k) = -\frac{2\Delta t}{\left(2\varepsilon(i,j,k) + \Delta t.\sigma(i,j,k)\right)\Delta y}$$
(2.90)

$$C_{ezj}(i,j,k) = -\frac{2\Delta t}{2\varepsilon(i,j,k) + \Delta t.\sigma(i,j,k)}$$
(2.91)

The FDTD updating equations for  $H_x^{n+1/2}(i, j, k)$ :

$$H_{x}^{n+1/2}(i,j,k) = C_{hxh}(i,j,k) \times H_{x}^{n-1/2}(i,j,k) + C_{hxey}(i,j,k) \times (E_{y}^{n}(i,j,k+1) - E_{y}^{n}(i,j,k)) + C_{hxez}(i,j,k) \times (E_{z}^{n}(i,j+1,k) - E_{z}^{n}(i,j,k)) + C_{hxm}(i,j,k) \times M_{source_{x}}^{n}(i,j,k)$$
(2.92)

where

$$C_{hxh}(i,j,k) = \frac{2\mu(i,j,k) - \Delta t.\sigma^{*}(i,j,k)}{2\mu(i,j,k) + \Delta t.\sigma^{*}(i,j,k)}$$
(2.93)

$$C_{hxey}(i,j,k) = \frac{2\Delta t}{\left(2\mu(i,j,k) + \Delta t.\sigma^*(i,j,k)\right)\Delta z}$$
(2.94)

$$C_{hxez}(i,j,k) = -\frac{2\Delta t}{\left(2\mu(i,j,k) + \Delta t.\sigma^*(i,j,k)\right)\Delta y}$$
(2.95)

$$C_{hxm}(i,j,k) = -\frac{2\Delta t}{2\mu(i,j,k) + \Delta t.\sigma^{*}(i,j,k)}$$
(2.96)

The FDTD updating equations for  $H_y^{n+1/2}(i,j,k)$ :

$$H_{y}^{n+1/2}(i,j,k) = C_{hyh}(i,j,k) \times H_{y}^{n-1/2}(i,j,k) + C_{hyez}(i,j,k) \times (E_{z}^{n}(i+1,j,k) - E_{z}^{n}(i,j,k)) + C_{hyex}(i,j,k) \times (E_{x}^{n}(i,j,k+1) - E_{x}^{n}(i,j,k)) + C_{hym}(i,j,k) \times M_{source_{x}}^{n}(i,j,k)$$
(2.97)

where

$$C_{hyh}(i,j,k) = \frac{2\mu(i,j,k) - \Delta t.\sigma^{*}(i,j,k)}{2\mu(i,j,k) + \Delta t.\sigma^{*}(i,j,k)}$$
(2.98)

$$C_{hyez}(i,j,k) = \frac{2\Delta t}{\left(2\mu(i,j,k) + \Delta t.\sigma^*(i,j,k)\right)\Delta x}$$
(2.99)

$$C_{hyex}(i,j,k) = -\frac{2\Delta t}{\left(2\mu(i,j,k) + \Delta t.\sigma^*(i,j,k)\right)\Delta z}$$
(2.100)

$$C_{hym}(i,j,k) = -\frac{2\Delta t}{2\mu(i,j,k) + \Delta t.\sigma^{*}(i,j,k)}$$
(2.101)

The FDTD updating equations for  $H_z^{n+1/2}(i,j,k)$ :

$$H_{z}^{n+1/2}(i,j,k) = C_{hzh}(i,j,k) \times H_{z}^{n-1/2}(i,j,k)$$

$$+ C_{hzex}(i,j,k) \times (E_{x}^{n}(i,j+1,k) - E_{x}^{n}(i,j,k))$$

$$+ C_{hzey}(i,j,k) \times (E_{y}^{n}(i+1,j,k) - E_{y}^{n}(i,j,k))$$

$$+ C_{hzm}(i,j,k) \times M_{source}^{n}(i,j,k)$$
(2.102)

where

$$C_{hzh}(i,j,k) = \frac{2\mu(i,j,k) - \Delta t.\sigma^{*}(i,j,k)}{2\mu(i,j,k) + \Delta t.\sigma^{*}(i,j,k)}$$
(2.103)

$$C_{hzex}(i,j,k) = \frac{2\Delta t}{\left(2\mu(i,j,k) + \Delta t.\sigma^*(i,j,k)\right)\Delta y}$$
(2.104)

$$C_{hzey}(i,j,k) = -\frac{2\Delta t}{\left(2\mu(i,j,k) + \Delta t.\sigma^*(i,j,k)\right)\Delta x}$$
(2.105)

$$C_{hzm}(i,j,k) = -\frac{2\Delta t}{2\mu(i,j,k) + \Delta t.\sigma^{*}(i,j,k)}$$
(2.106)

The first and second symbols in the subscripts used in the coefficient equations indicate the updated relevant field component, and the third and fourth subscripts indicate the type of the area where these coefficients are multiplied. After determining the FDTD equations, the time-marching algorithm can be created, every step of the time-marching algorithm the magnetic field components are updated for time instant  $(n+1/2)\Delta t$  and after one step the electric field components are updated for time instant  $(n+1)\Delta t$ . Since the problem space is finite dimensional, the field components on the boundaries of the problem space are calculated according to the type of boundary conditions during iteration. Any desired field can be stored or used after the electric field and magnetic field are updated using the FDTD algorithm. FDTD iterations can be continued until the conditions specified in the algorithm are achieved [89, 90].

#### 2.4.3 FDTD Updating Equations for Two-Dimensional Problems

When it is assumed that there is no change in one of the axes of the structure/geometry that is numerically modeled using the FDTD algorithm, the derivative terms with respect to this axis are equal to zero. In this case, the equations used in the algorithm are reduced from 3-dimensions to 2-dimensions. Equations in 2-dimensions can be expressed in two groups. All electric field components in the first group are transverse to the reference dimension, while in the second group all magnetic field components are transverse to the reference dimension. The first

group of equations is called the  $TE_z$  mode, the second group of equations is called the  $TM_z$  mode.

For  $TE_z$  mode the updating formula for the FDTD algorithm can be obtained by applying the central difference formula. The placement of  $TE_z$  mode field equations in cartesian coordinates is as shown in the Figure 2.4.

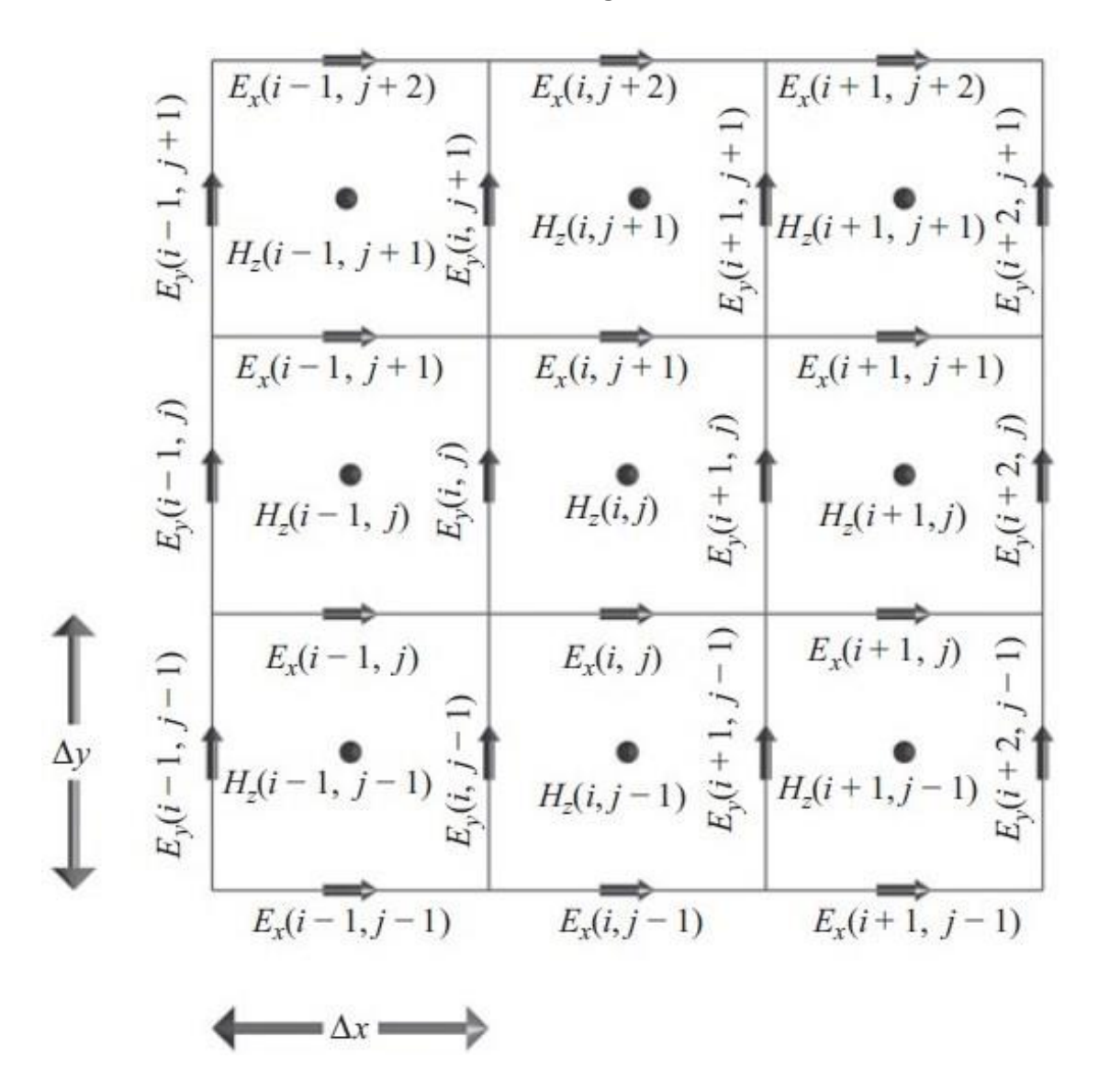


Figure 2.4 Two-Dimensional TE<sub>z</sub> FDTD Field Components [89]

The 2-D FDTD updating equations for  $E_x^{n+1}(i,j)$ :

$$E_{x}^{n+1}(i,j) = C_{exe}(i,j) \times E_{x}^{n}(i,j) + C_{exhz}(i,j) \times (H_{z}^{n+1/2}(i,j) - H_{z}^{n+1/2}(i,j-1)) + C_{exj}(i,j) \times J_{source}^{n+1/2}(i,j)$$
(2.107)

where

$$C_{exe}(i,j) = \frac{2\varepsilon(i,j) - \Delta t.\sigma(i,j)}{2\varepsilon(i,j) + \Delta t.\sigma(i,j)}$$
(2.108)

$$C_{exhz}(i,j) = \frac{2\Delta t}{\left(2\varepsilon(i,j) + \Delta t.\sigma(i,j)\right)\Delta y}$$
(2.109)

$$C_{exj}(i,j) = -\frac{2\Delta t}{\left(2\varepsilon(i,j) + \Delta t.\sigma(i,j)\right)}$$
(2.110)

The 2-D FDTD updating equation for  $E_y^{n+1}(i, j)$ :

$$E_{y}^{n+1}(i,j) = C_{eye}(i,j) \times E_{y}^{n}(i,j) + C_{eyhz}(i,j) \times (H_{z}^{n+1/2}(i,j) - H_{z}^{n+1/2}(i-1,j)) + C_{eyj}(i,j) \times J_{source,}^{n+1/2}(i,j)$$
(2.111)

where

$$C_{eye}(i,j) = \frac{2\varepsilon(i,j) - \Delta t.\sigma(i,j)}{2\varepsilon(i,j) + \Delta t.\sigma(i,j)}$$
(2.112)

$$C_{eyhz}(i,j) = -\frac{2\Delta t}{\left(2\varepsilon(i,j) + \Delta t.\sigma(i,j)\right)\Delta x}$$
(2.113)

$$C_{eyj}(i,j) = -\frac{2\Delta t}{\left(2\varepsilon(i,j) + \Delta t.\sigma(i,j)\right)}$$
(2.114)

The 2-D FDTD updating equation for  $H_z^{n+1/2}(i,j)$ :

$$H_{z}^{n+1/2}(i,j) = C_{hzh}(i,j) \times H_{z}^{n-1/2}(i,j) + C_{hzex}(i,j) \times \left(E_{x}^{n}(i,j+1) - E_{x}^{n}(i,j)\right) + C_{hzey}(i,j) \times \left(E_{y}^{n}(i+1,j) - E_{y}^{n}(i,j)\right) + C_{hzm}(i,j) \times M_{source}^{n}(i,j)$$
(2.115)

where

$$C_{hzh}(i,j) = \frac{2\mu(i,j) - \Delta t.\sigma^*(i,j)}{2\mu(i,j) + \Delta t.\sigma^*(i,j)}$$
(2.116)

$$C_{hzex}(i,j) = \frac{2\Delta t}{\left(2\mu(i,j) + \Delta t.\sigma^*(i,j)\right)\Delta y}$$
(2.117)

$$C_{hzey}(i,j) = -\frac{2\Delta t}{\left(2\mu(i,j) + \Delta t.\sigma^*(i,j)\right)\Delta x}$$
(2.118)

$$C_{hzm}(i,j) = \frac{2\Delta t}{\left(2\mu(i,j) + \Delta t.\sigma^*(i,j)\right)}$$
(2.119)

For  $TM_z$  mode the updating formula for the FDTD algorithm can be obtained by applying the central difference formula. The placement of  $TM_z$  mode field equations in cartesian coordinates is as shown in the Figure 2.5.

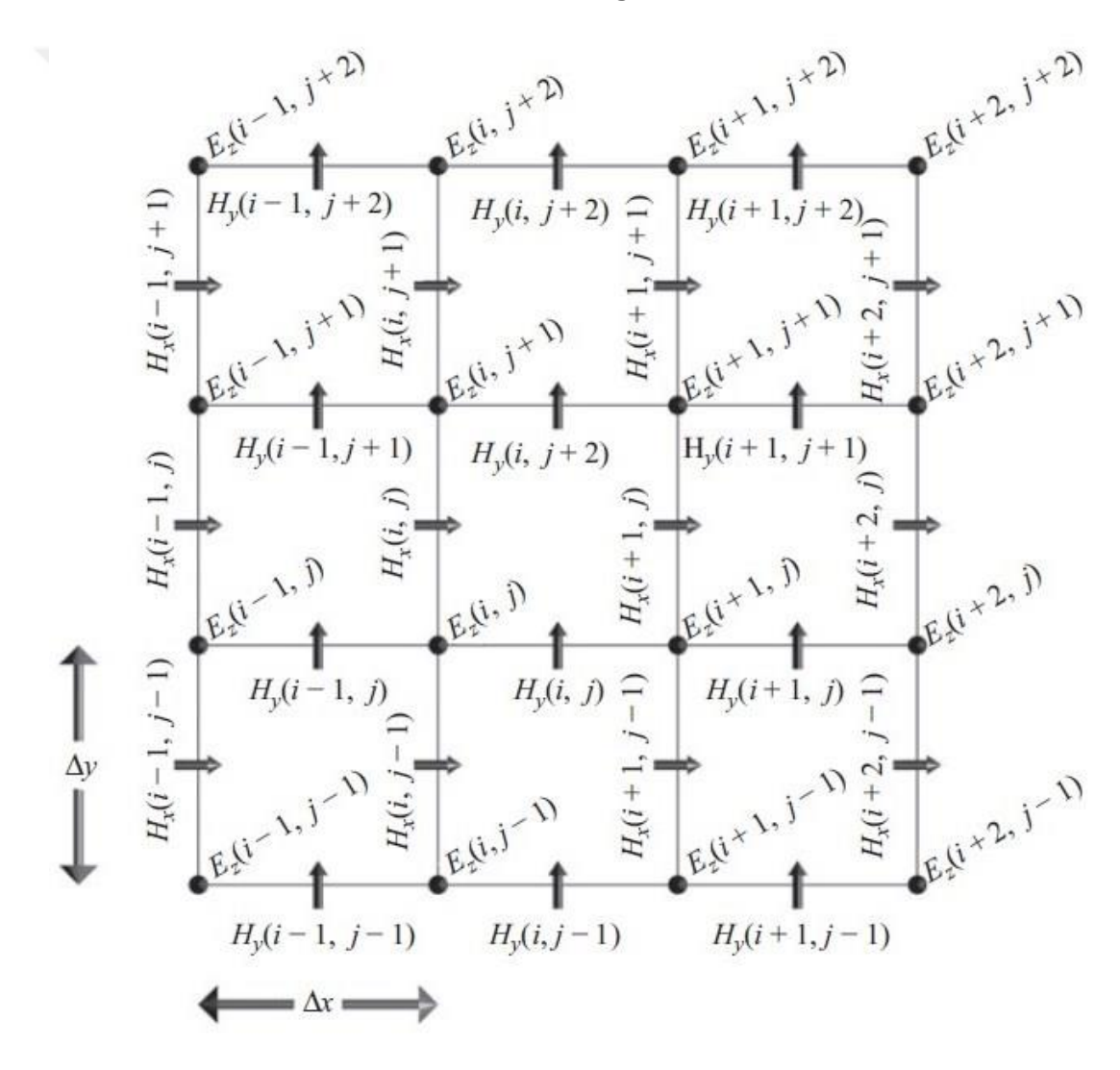


Figure 2.5 Two-Dimenssional TMz FDTD Field Components [89]

The 2-D FDTD updating equations for  $E_z^{n+1}(i,j)$ :

$$\begin{split} E_{z}^{n+1}\left(i,j\right) &= C_{eze}\left(i,j\right) \times E_{z}^{n}\left(i,j\right) + C_{ezhy}\left(i,j\right) \times \left(H_{y}^{n+1/2}\left(i,j\right) - H_{y}^{n+1/2}\left(i-1,j\right)\right) \\ &+ C_{ezhx}\left(i,j\right) \times \left(H_{x}^{n+1/2}\left(i,j\right) - H_{x}^{n+1/2}\left(i,j-1\right)\right) \\ &+ C_{ezj}\left(i,j\right) \times J_{source_{z}}^{n+1/2}\left(i,j\right) \end{split} \tag{2.120}$$

where

$$C_{eze}(i,j) = \frac{2\varepsilon(i,j) - \Delta t.\sigma(i,j)}{2\varepsilon(i,j) + \Delta t.\sigma(i,j)}$$
(2.121)

$$C_{ezhy}(i,j) = \frac{2\Delta t}{\left(2\varepsilon(i,j) + \Delta t.\sigma(i,j)\right)\Delta x}$$
(2.122)

$$C_{ezhx}(i,j) = -\frac{2\Delta t}{\left(2\varepsilon(i,j) + \Delta t.\sigma(i,j)\right)\Delta y}$$
(2.123)

$$C_{ezj}(i,j) = -\frac{2\Delta t}{\left(2\varepsilon(i,j) + \Delta t.\sigma(i,j)\right)}$$
(2.124)

The 2-D FDTD updating equations for  $H_x^{n+1/2}(i,j)$ :

$$H_{x}^{n+1/2}(i,j) = C_{hxh}(i,j) \times H_{x}^{n-1/2}(i,j) + C_{hxez}(i,j) \times (E_{z}^{n}(i,j+1) - E_{z}^{n}(i,j)) + C_{hxm}(i,j) \times M_{source_{z}}^{n}(i,j)$$

$$(2.125)$$

where

$$C_{hxh}(i,j) = \frac{2\mu(i,j) - \Delta t.\sigma^{*}(i,j)}{2\mu(i,j) + \Delta t.\sigma^{*}(i,j)}$$
(2.126)

$$C_{hxez}(i,j) = -\frac{2\Delta t}{\left(2\mu(i,j) + \Delta t.\sigma^*(i,j)\right)\Delta y}$$
(2.127)

$$C_{hxm}(i,j) = -\frac{2\Delta t}{\left(2\mu(i,j) + \Delta t.\sigma^*(i,j)\right)\Delta y}$$
(2.128)

The 2-D FDTD updating equations for  $H_{\nu}^{n+1/2}(i,j)$ :

$$H_{y}^{n+1/2}(i,j) = C_{hyh}(i,j) \times H_{y}^{n-1/2}(i,j) + C_{hyez}(i,j) \times (E_{z}^{n}(i+1,j) - E_{z}^{n}(i,j)) + C_{hym}(i,j) \times M_{source_{y}}^{n}(i,j)$$
(2.129)

where

$$C_{hyh}(i,j) = \frac{2\mu(i,j) - \Delta t.\sigma^*(i,j)}{2\mu(i,j) + \Delta t.\sigma^*(i,j)}$$
(2.130)

$$C_{hyez}(i,j) = \frac{2\Delta t}{\left(2\mu(i,j) + \Delta t.\sigma^*(i,j)\right)\Delta x}$$
(2.131)

$$C_{hym}(i,j) = -\frac{2\Delta t}{2\mu(i,j) + \Delta t.\sigma^*(i,j)}$$
(2.132)

### 2.4.4 FDTD Updating Equations for One-Dimensional Problems

In the one-dimensional problems, there is only one-dimensional change in problem geometry and field distributions. For example, only the x-axis has change for the geometry and field, the derivative with respect to y and z dimensions vanish in Maxwell's curl equations. The curl equations that reduced to one-dimension is given (2.54) -(2.56) and (2.59) -(2.61). In the (2.54) -(2.56) and (2.59) -(2.61) equations for  $E_x$  and  $H_x$  include time derivative but not include space derivative so FDTD updating equations not need for these equations because these equations do not represent the propagating fields. The equations for  $E_y$ ,  $H_z$ ,  $E_z$  and  $H_y$  represent propagating fields that transverse to the x-axis. Firstly, FDTD updating equations for TE mode components are given. The fields position in one-dimensional space is given in Figure 2.6.

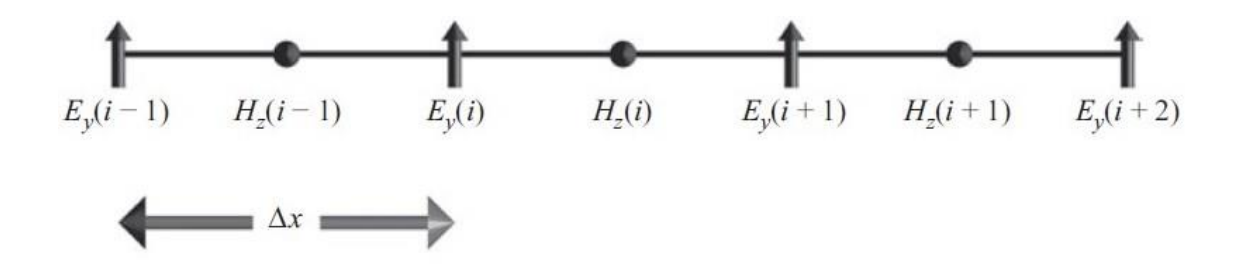


**Figure 2.6** One-Dimensional FDTD Positions of Field Components  $E_y$  and  $H_z$  [89]

The 1-D FDTD updating equations for  $E_y^{n+1}(i, j)$ :

$$E_{y}^{n+1}(i) = C_{eye}(i) \times E_{y}^{n}(i) + C_{eyhz}(i) \times (H_{z}^{n+1/2}(i) - H_{z}^{n+1/2}(i-1)) + C_{eyi}(i) \times J_{iy}^{n+1/2}(i)$$
(2.133)

where

$$C_{eye}(i) = \frac{2\varepsilon(i) - \Delta t.\sigma(i)}{2\varepsilon(i) + \Delta t.\sigma(i)}$$
(2.134)

$$C_{eyhz}(i) = -\frac{2\Delta t}{\left(2\varepsilon(i) + \Delta t.\sigma(i)\right)\Delta x}$$
(2.135)

$$C_{eyj}(i) = -\frac{2\Delta t}{2\varepsilon(i) + \Delta t.\sigma(i)}$$
(2.136)

The 1-D FDTD updating equations for  $H_z^{n+1/2}(i)$ :

$$H_{z}^{n+1/2}(i) = C_{hzh}(i) \times H_{z}^{n-1/2} + C_{hzey}(i) \times (E_{y}^{n}(i+1) - E_{y}^{n}(i)) + C_{hzm}(i) \times M_{source_{z}}^{n}(i)$$
(2.137)

where

$$C_{hzh}(i) = \frac{2\mu(i) - \Delta t.\sigma^{*}(i)}{2\mu(i) + \Delta t.\sigma^{*}(i)}$$
(2.138)

$$C_{hzey}(i) = -\frac{2\Delta t}{\left(2\mu(i) + \Delta t.\sigma^*(i)\right)\Delta x}$$
(2.139)

$$C_{hzm}(i) = -\frac{2\Delta t}{2\mu(i) + \Delta t.\sigma(i)}$$
(2.140)

Secondly, FDTD updating equations for TM mode components are given. The fields position in one-dimensional space is given in Figure 2.7.

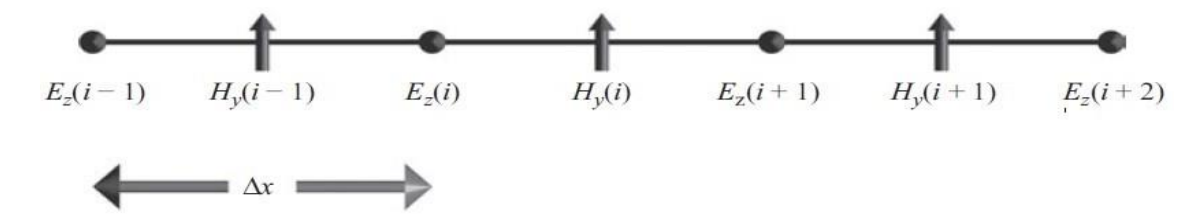


**Figure 2.7** One-Dimensional FDTD Positions of Field Components  $E_z$  and  $H_y$  [89]

The 1-D FDTD updating equations for  $E_z^{n+1}(i)$ :

$$E_{z}^{n+1}(i) = C_{eze}(i) \times E_{z}^{n}(i) + C_{ezhy}(i) \times (H_{y}^{n+1/2}(i) - H_{y}^{n+1/2}(i-1)) + C_{ezj}(i) \times J_{source_{z}}^{n+1/2}(i)$$
(2.141)

where

$$C_{eze}(i) = \frac{2\varepsilon(i) - \Delta t.\sigma(i)}{2\varepsilon(i) + \Delta t.\sigma(i)}$$
(2.142)

$$C_{ezhy}(i) = \frac{2\Delta t}{(2\varepsilon(i) + \Delta t.\sigma(i))\Delta x}$$
 (2.143)

$$C_{ezj}(i) = -\frac{2\Delta t}{2\varepsilon(i) + \Delta t.\sigma(i)}$$
(2.144)

The 1-D FDTD updating equations for  $H_v^{n+1/2}(i)$ :

$$H_{y}^{n+1/2}(i) = C_{hyh}(i) \times H_{y}^{n-1/2} + C_{hyez}(i) \times (E_{z}^{n}(i+1) - E_{z}^{n}(i)) + C_{hym}(i) \times M_{source_{y}}^{n}(i)$$
(2.145)

where

$$C_{hyh}(i) = \frac{2\mu(i) - \Delta t.\sigma^{*}(i)}{2\mu(i) + \Delta t.\sigma^{*}(i)}$$
(2.146)

$$C_{hyez}(i) = \frac{2\Delta t}{\left(2\mu(i) + \Delta t.\sigma^*(i)\right)\Delta x}$$
 (2.147)

$$C_{hym}(i) = -\frac{2\Delta t}{2\mu(i) + \Delta t.\sigma^*(i)}$$
(2.148)

# 2.5 Stability Criteria and Numerical Dispersion

## 2.5.1 Stability Criteria in FDTD Algorithm

The choice of space increment and time step in a finite different grid that modeled the one-dimensional scalar wave equation affects the propagation velocity of the numerical waves and thus the numerical error. Unstable solutions which is likely to occur in solutions of differential equations is undesirable. If the numerical stability is not provided, the results will be unlimited and irregular increase during the time-increment. Since the electric field and magnetic field at separate points in time and space are sampled using the FDTD algorithm, the sampling selection in time and space steps must be made according to certain rules in order to ensure solution stability [90].

Taking consideration, the wave equation stability criteria can be given simply.

$$\frac{\partial f(x,t)}{\partial t} + \frac{\partial f(x,t)}{\partial x} = 0, \quad f(x,t=0) = f_0(x)$$
 (2.149)

where f(x,t) is the unknown wave function,  $f_0(x)$  is the initial condition at t=0. This partial differential equation can be solved analytically.

$$f(x,t) = f_0(x-t)$$
 (2.150)

Discretizing the f(x,t) both in time and space domains, a time-domain numerical scheme can be developed to solve the wave equation numerically.

$$x_i = i\Delta x, \quad i = 1, 2, 3, ...$$
  
 $t_n = n\Delta t, \quad t = 1, 2, 3, ...$   
 $f_i^n = f(x_i, t_n)$  (2.151)

where  $\Delta t$  is the time cell size and  $\Delta x$  is the space cell size. To obtain the numerical solution of the (2.149) finite-difference scheme is needed for computing the derivatives.

$$\frac{f_i^{n+1} - f_i^{n-1}}{2\Delta t} + \frac{f_{i-1}^n - f_{i+1}^n}{2\Delta x} = 0$$
 (2.152)

Using the mathematical manipulations, the time domain numerical scheme can be obtained as follows:

$$f_i^{n+1} = f_i^{n-1} + \lambda \left( f_{i+1}^n - f_{i-1}^n \right), \quad \lambda = \frac{\Delta t}{\Delta x}$$
 (2.153)

where i shows the x position and n shows the time and there is a small numerical error represented by the  $\varepsilon$ . The error probably results from the truncation of real number. The error will continue to propagate in this time-domain algorithm; however, it can be observed that errors are always limited to the original error  $\varepsilon$ . Errors are always limited to the original error  $\varepsilon$ , and in the case where  $\lambda=1$ , the maximum absolute value of the propagation error is the same as the original error, when  $\lambda=2$ , the propagation of the error will continue to increase as time progresses. In cases where the error is large enough, the true value of u is lost and the time-domain algorithm deviates from the correct result due to a very small initial error [90].

According to the sampling theory the numerical stability of the FDTD algorithm specified in time by the following formula:

$$\Delta t < \frac{1}{2f_{\text{max}}} \tag{2.154}$$

where  $f_{\rm max}$  the maximum frequency content. For example when the maximum frequency  $f=6.0~{\rm GHz}$  the sampling rate must be less than  $3\times10^{-11}~{\rm sec}$  or  $3\times10^{-2}~{\rm ns}$ .

Another sampling criterion is about time increment  $\Delta t$  and space increment that is to say  $\Delta x$ ,  $\Delta y$  or  $\Delta z$ . This criterion is known as the Courant-Friedrichs-Levy (CFL) criteria and given as follows:

$$\Delta t \le \frac{1}{c\sqrt{\frac{1}{\left(\Delta x\right)^{2}} + \frac{1}{\left(\Delta y\right)^{2}} + \frac{1}{\left(\Delta z\right)^{2}}}}$$
(2.155)

$$\Delta t < \frac{1}{2f_{\text{max}}} c\Delta t \sqrt{\frac{1}{\left(\Delta x\right)^2} + \frac{1}{\left(\Delta y\right)^2} + \frac{1}{\left(\Delta z\right)^2}} \le 1$$
(2.156)

In three-dimensional problems for uniform spatial discretization  $\left(\Delta_x = \Delta_y = \Delta_z\right)$  one can get  $\Delta t \le \frac{\Delta x}{c\sqrt{3}}$  and for two-dimensional problems  $\Delta t \le \frac{\Delta x}{c\sqrt{2}}$  For instance if

 $\Delta x = 0.0015$ ,  $\Delta t$  must be less than  $3.538 \times 10^{-3}$  ns. In one-dimensional case where  $\Delta y \to \infty$  and  $\Delta z \to \infty$  the CFL criteria reduced to  $\Delta t \le \Delta x/c$  or  $c\Delta t \le \Delta x$ . According to this equation, a wave can travel in space at most one cell size during one time step.

#### 2.5.2 Numerical Dispersion

Although the FDTD method provides a good approach to examining the real physical behavior of fields, approaching the derivatives of continuous functions with finite differences causes a difference between the real solution and the numerical solution, and this difference is called error. The difference of the phase velocities obtained numerically by the FDTD method from the actual phase velocities is called the numerical dispersion. For example, assuming that a plane wave which is propagating in the free space along the *x*-axis given by

$$E_z(x,t) = E_0 \cos(k_x x - \omega t)$$
 (2.157)

$$H_{v}(x,t) = H_{0}\cos(k_{x}x - \omega t)$$
(2.158)

where  $E_z(x,t)$  satisfies the wave equation

$$\frac{\partial^2}{\partial x^2} E_z - \mu_0 \varepsilon_0 \frac{\partial^2}{\partial t^2} E_z = 0 \tag{2.159}$$

Substituting the  $E_z(x,t)$  given in (2.157) in the wave equation given in (2.159) the following equation van be obtained given in (2.160).

$$k_x^2 = \omega^2 \mu_0 \varepsilon_0 = \left(\frac{\omega}{c}\right)^2 \tag{2.160}$$

Eq. (2.160) is known as the dispersion relation.

The dispersion relation which is analytically exact determines the relation between the spatial frequency  $k_x$  and the temporal frequency  $\omega$  [89].

The numerical dispersion relation or in other words dispersion relation can be calculated according to the finite-difference approximation of Maxwell's curl equations. In the source-free medium the plane wave expressions given in (2.157) and (2.158) satisfy the Maxwell's curl equations in one-dimension.

$$\frac{\partial E_z}{\partial t} = \frac{1}{\varepsilon_0} \frac{\partial H_y}{\partial x} \tag{2.161}$$

$$\frac{\partial H_y}{\partial t} = \frac{1}{\mu_0} \frac{\partial E_z}{\partial x} \tag{2.162}$$

The FDTD algorithm for these equations can be obtained using the central difference formula.

$$\frac{E_z^{n+1}(i) - E_z^n(i)}{\Delta t} = \frac{1}{\varepsilon_0} \frac{H_y^{n+1/2}(i) - H_y^{n+1/2}(i-1)}{\Delta x}$$
 (2.163)

$$\frac{H_{y}^{n+1/2}(i) - H_{y}^{n-1/2}(i-1)}{\Delta t} = \frac{E_{z}^{n}(i+1) - E_{z}^{n}(i)}{\Delta x}$$
(2.164)

The plane wave equations given (2.157) and (2.158) can be discretized in space and time since they are continuous in space and time.

$$E_z^n(i) = E_0 \cos(k_x i \Delta x - \omega n \Delta t)$$
 (2.165)

$$E_z^{n+1}(i) = E_0 \cos(k_x i \Delta x - \omega(n+1) \Delta t)$$
(2.166)

$$E_z^n(i+1) = E_0 \cos(k_x(i+1)\Delta x - \omega n \Delta t)$$
(2.167)

$$H_y^{n+1/2}(i) = H_0 \cos(k_x(i+0.5)\Delta x - \omega(n+0.5)\Delta t)$$
 (2.168)

$$H_y^{n+1/2}(i-1) = H_0 \cos(k_x(i-0.5)\Delta x - \omega(n+0.5)\Delta t)$$
 (2.169)

$$H_y^{n-1/2}(i) = H_0 \cos(k_x(i+0.5)\Delta x - \omega(n-0.5)\Delta t)$$
 (2.170)

Using the equation (2.165), (2.166), (2.167) and (2.169) in the equation (2.171) can be obtained as follows.

$$\frac{E_0}{\Delta t} \left( \cos\left(k_x i \Delta x - \omega(n+1) \Delta t\right) - \cos\left(k_x i \Delta x - \omega n \Delta t\right) \right) \\
= \frac{H_0}{\varepsilon_0 \Delta x} \begin{pmatrix} \cos\left(k_x (i+0.5) \Delta x - \omega(n+0.5) \Delta t\right) \\
-\cos\left(k_x (i-0.5) \Delta x - \omega(n+0.5) \Delta t\right) \end{pmatrix} \tag{2.171}$$

Using the trigonometric identity  $\cos(x-y)-\cos(x+y)=2\sin(x)\sin(y)$ . In the (2.171) considering that  $x=k_xi\Delta x-\omega(n+0.5)\Delta t$ ,  $y=0.5\Delta t$  on the left side and  $x=k_xi\Delta x-\omega(n+0.5)\Delta t$ ,  $y=-0.5\Delta t$  one can obtain.

$$\frac{E_0}{\Delta t} \sin(0.5\omega\Delta t) = -\frac{H_0}{\varepsilon_0 \Delta x} \sin(0.5k_x \Delta x)$$
 (2.172)

Using the equation (2.165), (2.167), (2.168) and (2.170) in the equation (2.164), the equation (2.171) can be obtained as follows.

$$\frac{H_0}{\Delta t}\sin(0.5\omega\Delta t) = -\frac{E_0}{\mu_0\Delta x}\sin(0.5k_x\Delta x) \tag{2.173}$$

The numerical dispersion relation can be obtained like in the (2.174) using the (2.172) and (2.173) together.

$$\left(\frac{1}{c\Delta t}\sin\left(\frac{\omega\Delta t}{2}\right)\right)^2 = \left(\frac{1}{\Delta x}\sin\left(\frac{k_x\Delta x}{2}\right)\right)^2 \tag{2.174}$$

The relation given in (2.174) is called the numerical dispersion relation and this numerical dispersion relation is different from the ideal dispersion relation given by (2.160). This difference is due to the deviation between the real solution of the problem and the finite difference solution. But for the one dimensional case, using the  $\Delta t = \Delta x/c$  numerical dispersion relation reduces to the ideal dispersion relation and this means that there is no dispersion error for propagating in the free space. Similarly, the numerical dispersion relation for two-dimensional and three-dimensional cases can be obtained respectively [90].

$$\left(\frac{1}{c\Delta t}\sin\left(\frac{\omega\Delta t}{2}\right)\right)^{2} = \left(\frac{1}{\Delta x}\sin\left(\frac{k_{x}\Delta x}{2}\right)\right)^{2} + \left(\frac{1}{\Delta y}\sin\left(\frac{k_{y}\Delta y}{2}\right)\right)^{2}$$
(2.175)

In here there is no variation in the z-dimension.

For the special case 
$$\Delta x = \Delta y = \Delta$$
,  $\Delta t = \frac{\Delta}{c\sqrt{2}}$ , and  $k_x = k_y$ .

The ideal numerical dispersion equality for two-dimensional problems can be expressed as following:

$$k_x^2 + k_y^2 = \left(\frac{\omega}{c}\right)^2 \tag{2.176}$$

$$\left(\frac{1}{c\Delta t}\sin\left(\frac{\omega\Delta t}{2}\right)\right)^{2} = \left(\frac{1}{\Delta x}\sin\left(\frac{k_{x}\Delta x}{2}\right)\right)^{2} + \left(\frac{1}{\Delta y}\sin\left(\frac{k_{y}\Delta y}{2}\right)\right)^{2} + \left(\frac{1}{\Delta z}\sin\left(\frac{k_{z}\Delta z}{2}\right)\right)^{2} + \left(\frac{1}{\Delta z}\sin\left(\frac{k_{z}\Delta z}{2}\right)\right)^{2}$$
(2.177)

For the special case 
$$\Delta x = \Delta y = \Delta z = \Delta$$
,  $\Delta t = \frac{\Delta}{c\sqrt{3}}$ , and  $k_x = k_y = k_z$ 

The ideal numerical dispersion equality for three-dimensional problems can be expressed as following:

$$k_x^2 + k_y^2 + k_z^2 = \left(\frac{\omega}{c}\right)^2 \tag{2.178}$$

# 2.6 The Independence of FDTD Method from Divergence

One of the advantages of the FDTD algorithm is that the Gauss's Law for electric and magnetic field is provided automatically by the unit cell locations of the field components in source-free environments. Gauss's Law for the electric field can be seen as follows:

$$\nabla .\mathbf{D}(\mathbf{r},t) = 0 \Rightarrow \iiint_{v} \nabla .\mathbf{D}(\mathbf{r},t) dv = \iint_{s} \mathbf{D}(\mathbf{r},t) .d\mathbf{s} = 0$$
(2.179)

where  $\rho_e(\mathbf{r},t)=0$ .

Discretizing surface integral in terms of the unit Ye cell,

$$\iint_{s} \mathbf{D}(\mathbf{r},t) \cdot \mathbf{ds} = \left( D_{x}^{n} (i, j+1/2, k+1/2) - D_{x}^{n} (i-1, j+1/2, k+1/2) \right) \Delta y \Delta z$$

$$+ \left( D_{y}^{n} (i-1/2, j+1, k+1/2) - D_{y}^{n} (i-1/2, j, k+1/2) \right) \Delta x \Delta z$$

$$+ \left( D_{z}^{n} (i-1/2, j+1/2, k+1) - D_{z}^{n} (i-1/2, j+1/2, k) \right) \Delta x \Delta y$$
(2.180)

Taking the time derivative of all equations and writing in terms of the Maxwell equations:

$$\frac{\partial}{\partial t} \left( D_x^n (i, j+1/2, k+1/2) - D_x^n (i-1, j+1/2, k+1/2) \right) \Delta y \Delta z$$

$$= \begin{pmatrix} \frac{H_z^n (i, j+1, k+1/2) - H_z^n (i, j, k+1/2)}{\Delta y} \\ -\frac{H_y^n (i, j+1/2, k+1) - H_y^n (i, j+1/2, k)}{\Delta z} \end{pmatrix}$$

$$- \begin{pmatrix} \frac{H_z^n (i-1, j+1, k+1/2) - H_z^n (i-1, j, k+1/2)}{\Delta y} \\ -\frac{H_y^n (i-1, j+1/2, k+1) - H_y^n (i-1, j+1/2, k)}{\Delta z} \end{pmatrix}$$
(2.181)

$$\frac{\partial}{\partial t} \left( D_{y}^{n} \left( i - 1/2, j + 1, k + 1/2 \right) - D_{y}^{n} \left( i - 1/2, j, k + 1/2 \right) \right) \Delta x \Delta z$$

$$= \left( \frac{H_{x}^{n} \left( i - 1/2, j + 1, k + 1 \right) - H_{x}^{n} \left( i - 1/2, j + 1, k \right)}{\Delta z} \right)$$

$$- \left( \frac{H_{z}^{n} \left( i, j + 1, k + 1/2 \right) - H_{z}^{n} \left( i - 1, j + 1, k + 1/2 \right)}{\Delta x} \right)$$

$$- \left( \frac{H_{x}^{n} \left( i - 1/2, j, k + 1 \right) - H_{x}^{n} \left( i - 1/2, j, k \right)}{\Delta z} \right)$$

$$- \left( \frac{H_{z}^{n} \left( i, j, k + 1/2 \right) - H_{z}^{n} \left( i - 1, j, k + 1/2 \right)}{\Delta x} \right)$$
(2.182)

$$\frac{\partial}{\partial t} \left( D_z^n \left( i - 1/2, j + 1/2, k + 1 \right) - D_z^n \left( i - 1/2, j + 1/2, k \right) \right) \Delta x \Delta y$$

$$= \left( \frac{H_y^n \left( i, j + 1/2, k + 1 \right) - H_y^n \left( i - 1, j + 1/2, k + 1 \right)}{\Delta x} \right)$$

$$- \frac{H_x^n \left( i - 1/2, j + 1, k + 1 \right) - H_x^n \left( i - 1/2, j, k + 1 \right)}{\Delta y} \right)$$

$$- \left( \frac{H_y^n \left( i, j + 1/2, k \right) - H_y^n \left( i - 1, j + 1/2, k \right)}{\Delta x} \right)$$

$$- \left( \frac{H_x^n \left( i - 1/2, j + 1, k \right) - H_x^n \left( i - 1/2, j, k \right)}{\Delta y} \right)$$
(2.183)

Substituting these expressions in the integral equations given by (2.179),  $\frac{\partial}{\partial t} \iint_{s} \mathbf{D}(\mathbf{r},t) \cdot \mathbf{ds} = 0 \text{ is obtained. As a result, } \iint_{s} \mathbf{D}(\mathbf{r},t) \cdot \mathbf{ds} = \text{constant. Using the}$  $\mathbf{D}(\mathbf{r},t)\Big|_{t=0} = 0 \text{ initial condition, } \frac{\partial}{\partial t} \iint_{s} \mathbf{D}(\mathbf{r},t) \cdot \mathbf{ds} = 0 \text{ can be obtained. Hereunder, the}$ 

FDTD algorithm is independence from the divergence in the source free medium. Since the necessary condition is already provided within the FDTD algorithm automatically there is no need to create algorithms for divergence equations [90].

# SOURCE WAVEFORMS AND ABSORBING BOUNDARY CONDITIONS

In the approximate solutions of the problems using the FDTD algorithm, how to define electromagnetic wave excitations is important and source types vary depending on the type of problem under consideration. Sources are generally divided into two as near (voltage and current sources) and far (incident fields in scattering problems) in accordance with the type of problem being solved. Source excites electric and magnetic fields with a waveform as a function of time [90].

#### 3.1 Source Waveforms for FDTD Simulations

Sources are indispensable parts of FDTD simulations and are divided into two as far field and near field according to the type of problem to be solved. In both cases, a source excites electric and magnetic fields with a waveform as a function of time. The waveform type is specially selected according to the nature of the problem, considering some of the limitations of the FDTD method. The frequency spectrum of the source waveform used in FDTD simulation should include all frequencies used in the simulation. The selection of waveform types according to the type of problem to be solved is important. While the sine or cosine function refers to a single frequency waveform, Gaussian pulse, time derivative of Gaussian pulse, Gaussian pulse with cosine modulation are multi-frequency waveforms [89].

#### 3.1.1 Sinusoidal Waveform

A sinusoidal waveform is a single-frequency waveform. In FDTD simulation, the initial conditions for the sources are zero and the waveform can be excited for a limited time in the simulation. Therefore, in the simulation if sinusoidal signal  $(\sin(2\pi t), 0 < t < 4)$  waveform is used for a source its duration time is finite.

The Fourier transform of a continuous time function x(t) is  $X(\omega)$  given by

$$X(\omega) = \int_{-\infty}^{\infty} x(t)e^{-j\omega t}dt$$
(3.1)

and the inverse Fourier transform is

$$x(t) = \frac{1}{2\pi} \int_{-\infty}^{\infty} X(\omega) e^{j\omega t} d\omega$$
 (3.2)

The Fourier transform of the signal is a complex function. In an electromagnetic simulation induced using a sinusoidal waveform, the simulation must be run long enough for the transient response caused by the opening of the sources to disappear and only the sinusoidal response to persist [90].

#### 3.1.2 Gaussian Waveform

If simulations are desired to be made at broadband frequencies, the sinusoidal wave form is not suitable. The selection of the frequency spectrum of the source waveform is important for the results to be obtained from the FDTD algorithm to be valid and accurate. When the cell size in the computation domain is too large for part of a wavelength, the signal at that frequency cannot be accurately sampled in space. For this reason, the highest frequency in the source waveform spectrum should be chosen so that the cell size is less than or equal to a fraction of the highest frequency wavelength. A Gaussian waveform is the most suitable waveform as it can contain all frequencies down to the highest frequency that depends on a cell size by a factor.

A Gaussian waveform can be written as a function of time as

$$g(t) = \exp\left(-\left(\frac{t - t_0}{\tau_0}\right)^{1/2}\right)$$
 (3.3)

where  $t_0$  states how long after the start of the simulation the pulse will be included in the system,  $\tau_0$  is the parameter determining the pulse width. Since the product of time and time bandwidth is constant, as  $\tau_0$  gets smaller the frequency band widens.

If the Gaussian pulse is injected into the  $\,E_z\,$  component at a certain point, it is called soft source.

$$E_z^n(nxp, nyp) = E_z^n(nxp, nyp) + g(n)$$
(3.4)

where (nxp, nyp) is the point in the spatial that Gauss pulse is injected. At same time step, if the source is calculated after the  $E_z$  value is calculated then the source applied on the FDTD grid, it is called a hard source. In time domain g(n) is discrete Gauss function

$$E_z^n(nxp,nyp) = g(n) \tag{3.5}$$

Using the  $t_0=n_0\times\Delta t$ ,  $\tau_0=n_T\times\Delta t$  in (3.3) one can obtain (3.6) as follows,

$$g(n) = \exp\left(-\left(\frac{n - n_0}{n\tau}\right)^{1/2}\right)$$
 (3.6)

One of the important elements in electromagnetic problem simulation with FDTD is selection of the parameter [90]. The main purpose of simulating pulsed signals in time with FDTD is to examine the behavior of the studied structure in the wide frequency band. Since not every structure can be examined in every frequency region, the parameter selection should be chosen according to the desired frequency analysis. In this study, simulations that perform the FDTD algorithm for two-dimensional applications are made. For example, for TE case, the simulation contains  $E_x$ ,  $E_y$  and  $H_z$  components. In the case of TE, the Gaussian pulse is applied to the  $H_z$  component.

The minimum wavelength of the signal and the highest frequency signal need to be considered because these values are important for accurate and stable FDTD simulation. Source pulse duration is determined according to the highest frequency to be analyzed.

$$pulse \ duration = \tau_0 = \frac{1}{2f_{\text{max}}}$$
 (3.7)

Taking consideration, the maximum frequency  $f_{\text{max}} = 1.67 \text{ GHz}$  and pulse duration can be calculated using this value as in (3.6).

$$\tau_0 = \frac{1}{1.67 \times 10^9} = 0.3 \text{ ns} \tag{3.8}$$

The methods used for the selection of the cell step in the FDTD formulation are generally similar, but sufficient sampling points must be taken to obtain the desired results. The number of samples per wavelength depends on many factors but usually one tenth of the wavelength is a suitable approach [90]. In this case, the relation between position steps and wavelength is as follows.

$$\Delta x = \Delta y = 0.1 \times \lambda_{\min} \tag{3.9}$$

$$\lambda_{0,\min} = \frac{c}{f_{\max}} = \frac{3 \times 10^8}{1.67 \times 10^9} = 0.18m \tag{3.10}$$

$$\Delta x = \Delta y = 0.1 \times \lambda_{0,\text{min}} = 0.018m$$
 (3.11)

If the medium is a non-magnetic dielectric medium with a relative dielectric constant of  $\varepsilon_r = 4$ , the minimum wavelength and the position step are determined as in (3.12) and (3.13).

$$\lambda_{\min} = \frac{c/\sqrt{\varepsilon_r}}{f_{\max}} = \frac{3 \times 10^8/\sqrt{4}}{1.67 \times 10^9} \cong 0.1m$$
 (3.12)

$$\Delta x = \Delta y = dx = 0.1 \times \lambda_{\min} = 0.01m \tag{3.13}$$

In a non-magnetic dielectric medium, the phase velocity can be written as in (3.14) and in lossy dielectric medium the phase velocity is given in (3.15).

$$V_p = \frac{c}{\sqrt{\varepsilon_r}} \tag{3.14}$$

$$V_{p} = \frac{w}{\beta} \cong \frac{1}{\sqrt{\mu \varepsilon'}} \left[ 1 - \frac{1}{8} \left( \frac{\varepsilon''}{\varepsilon'} \right) \right] m/s \tag{3.15}$$

The phase velocity in the lossy medium is lower than the phase velocity of the lossless medium. In lossy materials  $(\sigma > 0)$ , the time step required for stability should be smaller than the Courant limit [93] but in many problems the time steps is determined by the speed of light. Since the velocity in conductive materials is smaller than the wave velocity in free space, in FDTD calculations that include both free space and conductive medium, the time step should be selected so that the Courant limit is provided throughout the calculation space.

The Gaussian pulse can be expressed with finite difference as in (3.16).

$$g(n\Delta t) = \exp\left(-\left(\frac{n \times \Delta t - t_0}{\tau_0}\right)^{1/2}\right)$$
 (3.16)

where  $t_0$  expresses how long after the Gaussian pulse will be injected after the simulation.

In Table 3.1 microwave frequency ranges used in the simulations and their wavelengths are given.

**Table 3.1** Microwave Frequency Ranges

Letter Display	Frequency Range	Wavelength Range	Wavelength Range (m)
L	1 GHz-2 GHz	15 cm -30 cm	0.15 m – 0.3 m
S	2 GHz-4 GHz	7.5 cm -15 cm	0.075 m – 0.15 m
С	4 GHz-8 GHz	3.75 cm – 7.5 cm	0.0375 m – 0.075 m
X	8 GHz-12 GHz	25 mm – 37.5 mm	0.025 m – 0.0375 m
Ku	12 GHz-18 GHz	16.7 mm – 25 mm	0.0167 m -0.025 m
К	18 GHz-26.5 GHz	11.3 mm – 16.7 mm	0.0113 m – 0.0167 m
Ка	26.5GHz-40 GHz	5 mm – 11.3 mm	0.005 m - 0.0113 m

# 3.2 Absorbing Boundary Conditions

Even if the computers used in simulations are high-capacity and fast, the FDTD calculation space must be finite since all simulations are performed in a limited area and in a limited time. In cases where the problem to be simulated is limited, the problem is solved by matching the boundary of the problem with the boundary of the FDTD calculation space, but in problems such as antenna problems and scattering problems, the computation space must be limited. In numerical wave propagation computations, an artificial boundary has to be defined to restrict the computation domain and absorb the outgoing waves. Physically, this process is like the walls of an anechoic chamber. Perfect electrically conductive (PEC) material and perfect magnetic conducting (PMC) material are used as boundary conditions to terminate the computation space [89]

In the perfect electric conductor boundary condition, boundaries can be closed with a perfect electric conductive material and a zero value can be assigned to electric field components tangent to the boundary planes. By applying this condition to all boundaries in the computational space, resonator type structures can be examined. When modeling the behavior of the electromagnetic wave in any waveguide, the boundary condition is not defined since the tangent electric field is zero on the walls.

In the perfect magnetic conductor boundary condition boundaries can be closed with a perfect magnetic conductive material and a zero value can be assigned to electric field components tangent to the boundary planes. According to PEC, PMC is a non-physical condition and is used to reduce the volume, especially in problems with structural symmetry. The plane in the middle of the symmetrical structure is closed with PMC and the symmetrical magnetic field values according to this plane are equal to each other [90].

Since it is not possible to simulate the infinite expansion of the problem space, the space must be restricted at a certain place where it will be sufficient for interactions and terminated appropriately. When the scattered and radiating fields reach the boundary, if the necessary boundary conditions are not applied, the fields can reflect

into the problem space. Usually, the boundary of the FDTD problem space is chosen in such a way that the scattered or radiating fields absorb them when they reach the boundary. In order to model the real infinity, the boundary conditions applied after the problem space is terminated in a certain region are called Absorbing Boundary Conditions (ABC). Absorbing boundary condition layer has a few mesh cells thickness and absorbs the electromagnetic waves on it with zero reflection in the entire frequency spectrum and at all angles [90].

The most commonly used absorbing boundary conditions are Mur type ABC, dispersive boundary condition (DBC) and perfectly matched layer (PML). The perfectly matched layer (PML) developed by Berenger [94, 95] has proven to be one of the strongest absorptive boundary conditions compared to other methods [95-99]. The perfectly matched layer (PML) is a finite thickness lossy material boundary layer that is perfectly matched to the solution space and surrounds the calculus space. PML uses artificial structural parameters to establish the wave impedance adaption condition, regardless of the frequency and angle of the incident wave. All the absorbing boundary conditions, types of which will be described below, must conform with the Courant stability condition.

## 3.2.1 Mur Type ABC

According to total field/scattered field (TF/SC) theory,

$$L^{-}f\Big|_{x=0} = 0 \Rightarrow \frac{\partial^{2}f}{\partial x \partial t} - \frac{1}{c} \frac{\partial^{2}f}{\partial t^{2}} + \frac{c}{2} \frac{\partial^{2}f}{\partial y^{2}} = 0$$
 (3.17)

taking consideration  $f=f_{\rm tan}$  at  $\left(1/2,j\right)$  cell and arranging the derivatives according to the central differences as follows

$$\frac{\partial^{2} f}{\partial x \partial t} \Big|_{1/2, j}^{n} = \frac{1}{2\Delta t} \left( \frac{\partial^{2} f}{\partial x} \Big|_{1/2, j}^{n+1} - \frac{\partial^{2} f}{\partial x} \Big|_{1/2, j}^{n-1} \right) 
= \frac{1}{2\Delta t} \left[ \left( \frac{f}{|_{1, j}^{n+1} - f} \Big|_{0, j}^{n+1} \right) - \left( \frac{f}{|_{1, j}^{n-1} - f} \Big|_{0, j}^{n-1} \right) \right]$$
(3.18)

$$\frac{\partial^{2} f}{\partial t^{2}}\Big|_{1/2,j}^{n} = \frac{1}{2} \left( \frac{\partial^{2} f}{\partial t^{2}} \Big|_{0,j}^{n} + \frac{\partial^{2} f}{\partial t^{2}} \Big|_{1,j}^{n} \right) \\
= \frac{1}{2} \left[ \left( \frac{f\Big|_{0,j}^{n+1} - 2f\Big|_{0,j}^{n} + f\Big|_{0,j}^{n-1}}{\Delta t^{2}} \right) + \left( \frac{f\Big|_{1,j}^{n+1} - 2f\Big|_{1,j}^{n} + f\Big|_{1,j}^{n-1}}{\Delta t^{2}} \right) \right]$$
(3.19)

$$\frac{\partial^{2} f}{\partial y^{2}}\Big|_{1/2,j}^{n} = \frac{1}{2} \left( \frac{\partial^{2} f}{\partial y^{2}} \Big|_{0,j}^{n} + \frac{\partial^{2} f}{\partial y^{2}} \Big|_{1,j}^{n} \right) \\
= \frac{1}{2} \left[ \left( \frac{f\Big|_{0,j+1}^{n} - 2f\Big|_{0,j}^{n} + f\Big|_{0,j-1}^{n}}{\Delta y^{2}} \right) + \left( \frac{f\Big|_{1,j+1}^{n} - 2f\Big|_{1,j}^{n} + f\Big|_{1,j-1}^{n}}{\Delta t^{2}} \right) \right]$$
(3.20)

Substituting (3.18) -(3.20) in the governing equation given in (3.17) and rearranging (3.17) according to the  $f|_{0,j}^{n+1}$  (3.21) can be obtained as follows.

$$f\Big|_{0,j}^{n+1} = -f\Big|_{1,j}^{n-1} + \frac{c\Delta t - \Delta x}{c\Delta t + \Delta x} \Big( f\Big|_{1,j}^{n+1} + f\Big|_{0,j}^{n-1} \Big) + \frac{2\Delta x}{c\Delta t + \Delta x} \Big( f\Big|_{0,j}^{n} + u\Big|_{1,j}^{n} \Big)$$

$$+ \frac{(c\Delta t)^{2} \Delta x}{2(\Delta y)^{2} (c\Delta t + \Delta x)} \left[ \frac{\left( f\Big|_{0,j+1}^{n} - 2f\Big|_{0,j}^{n} + f\Big|_{0,j-1}^{n} \right)}{+\left( f\Big|_{1,j+1}^{n} - 2f\Big|_{1,j}^{n} + f\Big|_{1,j-1}^{n} \right)} \right]$$

$$(3.21)$$

In the square mesh taking consideration  $\Delta x = \Delta y = \Delta$  and rearranging (3.21) according to this equality (3.22) can be obtained as follows.

$$f\Big|_{0,j}^{n+1} = -f\Big|_{1,j}^{n-1} + \frac{c\Delta t - \Delta}{c\Delta t + \Delta} \Big( f\Big|_{1,j}^{n+1} + f\Big|_{0,j}^{n-1} \Big) + \frac{2\Delta}{c\Delta t + \Delta} \Big( f\Big|_{0,j}^{n} + f\Big|_{1,j}^{n} \Big) + \frac{(c\Delta t)^{2}}{2\Delta (c\Delta t + \Delta)} \Bigg[ \Big( f\Big|_{0,j+1}^{n} - 2f\Big|_{0,j}^{n} + f\Big|_{0,j-1}^{n} \Big) + \Big( f\Big|_{1,j+1}^{n} - 2f\Big|_{1,j}^{n} + f\Big|_{1,j-1}^{n} \Big) \Bigg]$$

$$(3.22)$$

Considering the equations given above and equalizing to zero the first-order accuracy of the Mur type boundary condition of the derivatives which are in the y direction,  $f\Big|_{0,i}^{n+1}$  is finally obtained as in (3.23).

$$f\Big|_{0,j}^{n+1} = -f\Big|_{1,j}^{n-1} + \frac{c\Delta t - \Delta}{c\Delta t + \Delta} \Big(f\Big|_{1,j}^{n+1} + f\Big|_{0,j}^{n-1}\Big) + \frac{2\Delta}{c\Delta t + \Delta} \Big(f\Big|_{0,j}^{n} + f\Big|_{1,j}^{n}\Big)$$
(3.23)

(3.23) is the Mur type boundary condition for, Mur type boundary conditions can be obtained for can be obtained similarly [100].

# 3.3 Perfectly Matched Layer

Our problem is governed by Maxwell equations and they solved by using the FDTD in a computational domain to understand the interaction of the wave radiated from a point source and concrete structure. An absorbing layer encloses the computational domain and this calculation domain ends with perfect conductive conditions. In PML boundary condition the waves which have arbitrary incidence angle, frequency and polarization are matched at the boundary. Another advantage of the PML is the numerical computation domain can be composed of inhomogeneous, anisotropic, dispersive, or non-linear mediums. Such mediums cannot be modeled analytic ABCs

The Perfectly Matched Layer (PML) is a finite thickness lossy material boundary layer that is perfectly matched to the solution space and surrounds the computation space. It has been shown that the PML developed by Berenger [94] is one of the strongest absorbing boundary conditions then other boundary condition methods [98]. PML is based on the use of artificial structural parameters to establish the wave impedance adaption condition, regardless of the frequency and angle of the incident wave. The main advantage of PML over other ABCs is that it can absorb all waves any frequency, polarization, and angle on it ideally with zero reflection. Although there are various types of PML in the literature, the first PML application is applied to the problem space of FDTD by Berenger. There are some types of PML like Berenger PML [97] Stretched Coordinates PML [101], Conventional lossy

dispersionless absorbing medium [102], Uniaxial Anisotropic PML [99], Convolutional PML [103], Nearly PML [104].

Convolutional PML (CPML) is suitable for low frequency analysis. Berenger PML (BPML) requires modification of Maxwell's equations and field decomposition. Due to space separation, the memory requirement is doubled compared to traditional FDTD methods.

#### 3.3.1 Berenger PML

Berenger PML (BPML) is based on the principle of obtaining the reflection coefficient as zero by using non-physical splitting field components in the PML region with electrical and magnetic losses. [94]

$$Z_{problem} = \sqrt{\frac{\mu}{\varepsilon}} = \sqrt{\frac{\mu_0}{\varepsilon_0}} = \sqrt{\frac{\mu_r}{\varepsilon_r}}$$
 (3.24)

$$Z_{BPML} = \sqrt{\frac{\mu}{\varepsilon}} = \sqrt{\frac{\mu' + j\mu''}{\varepsilon' + j\varepsilon''}} = \sqrt{\frac{\mu_r \mu_0 + j\frac{\sigma^m}{\omega}}{\varepsilon_r \varepsilon_0 + j\frac{\sigma^e}{\omega}}} = \sqrt{\frac{\mu_0}{\varepsilon_0}} \sqrt{\frac{\mu_r + j\frac{\sigma^m}{\omega \mu_0}}{\varepsilon_r + j\frac{\sigma^e}{\omega \varepsilon_0}}}$$
(3.25)

(3.24) and (3.25) must be equal to provide the PML condition that is to say  $Z_{\it problem} = Z_{\it BPML}.$ 

$$Z_{problem} = Z_{BPML} \Rightarrow \sqrt{\frac{\mu_r}{\varepsilon_r}} = \sqrt{\frac{\mu_r + j\frac{\sigma^m}{\omega\mu_0}}{\varepsilon_r + j\frac{\sigma^e}{\omega\varepsilon_0}}}$$
(3.26)

Since impedance compatibility and reflection should be zero one need the (3.27).

$$\frac{\sigma^e}{\varepsilon_0} = \frac{\sigma^m}{\mu_0} \tag{3.27}$$

#### 3.3.2 Uniaxial PML

In the FDTD-UPML formulation, the entire spatial domain is considered to be anisotropic medium [90]. Since UPML is based on anisotropic material properties to define the absorptive layer, the lossy anisotropic environment can be perfectly matched to the isotropic environment by selecting the ambient parameters appropriately. The medium is anisotropic when the relationship between  ${\bf D}$  and  ${\bf E}$  (similarly  ${\bf B}$  and  ${\bf H}$ ) depends on the direction of  ${\bf E}$  and  ${\bf H}$ . Since  ${\bf D}$  and  ${\bf E}$  is not parallel to each other in the anisotropic medium, the structural parameters are expressed by the tensor dielectric constant  $(\bar{\varepsilon})$  and the tensor magnetic permeability  $(\bar{\mu})$ . According to the UPML algorithm, a uniaxial anisotropic medium is sufficient in terms of dielectric and magnetic permeability when there is only one interface. This means for a single interface the anisotropic medium is uniaxial.

Assuming that an arbitrary polarized plane wave propagating in Medium 1 impinging on Medium 2 with  $\theta_i$  angle. The magnetic field expression for the incident wave can be written in phasor form

$$\tilde{H}_{i} = \hat{a}_{z} H_{0} e^{-jk_{1x}x - jk_{1y}y} \tag{3.28}$$

where  $\overline{k}_1 = k_{1x}\hat{a}_x + k_{1y}\hat{a}_y$  is wave number vector of the Medium 1. The region where x > 0 is anisotropic medium and its electrical and magnetic permeabilities in uniaxial tensor structure are expressed as follows:

$$\frac{=}{\varepsilon_{2}} = \varepsilon_{2} \begin{bmatrix} a & 0 & 0 \\ 0 & b & 0 \\ 0 & 0 & b \end{bmatrix}, \quad \frac{=}{\mu_{2}} = \mu_{2} \begin{bmatrix} c & 0 & 0 \\ 0 & d & 0 \\ 0 & 0 & d \end{bmatrix}$$
(3.29)

Waves transmitted to the second medium are also planar waves and satisfy Maxwell's equations. The Maxwell's curl equations in phasor form can be given in (3.30) –(3.31).

$$\nabla \times \tilde{E} = -j\omega \mu_{2}\tilde{H} \tag{3.30}$$

$$\nabla \times \tilde{H} = j\omega \varepsilon_2 \tilde{E} \tag{3.31}$$

The scattering relationship of uniaxial media is obtained for TE and TM modes as follows.

$$\tilde{H}_{i} = \hat{a}_{z} H_{0} e^{-jk_{1x}x - jk_{1y}y} \tag{3.32}$$

$$\nabla \times \tilde{H} = j\omega \varepsilon_2 \tilde{E} \tag{3.33}$$

$$k_2^2 - (k_{2x})^2 b^{-1} d^{-1} - (k_{2y})^2 a^{-1} d^{-1} = 0 \text{ for TE}_z (\tilde{H}_x = 0, \tilde{H}_y = 0)$$
 (3.34)

$$k_2^2 - (k_{2x})^2 b^{-1} d^{-1} - (k_{2y})^2 b^{-1} c^{-1} = 0 \text{ for TM}_z (\tilde{H}_z = 0)$$
 (3.35)

where  $k_z^2 = \omega^2 \mu_z \varepsilon_z$ . As can be seen from (3.31) the scattering characteristics for TE and TM are similar to each other. Assuming that the incident wave is TE polarized wave, this wave has three field components  $E_x$ ,  $E_y$  and  $H_z$ .

The electric field for incident wave can be defined as follows:

$$\tilde{E}_i = E_0 \left( -\hat{a}_x \cos \theta_i + \hat{a}_y \sin \theta_i \right) e^{-jk_{1x}x - jk_{1y}y}$$
(3.36)

$$k_{1x} = k_1 \cos \theta_i \to \cos \theta_i = \frac{k_{1x}}{k_1} = \frac{k_{1x}}{\omega \sqrt{\mu_1 \varepsilon_1}}$$
(3.37)

$$k_{1y} = k_1 \sin \theta_i \to \sin \theta_i = \frac{k_{1y}}{k_1} = \frac{k_{1y}}{\omega \sqrt{\mu_1 \varepsilon_1}}$$
(3.38)

$$H_0 = \frac{E_0}{\eta_1} \to E_0 = \sqrt{\frac{\mu_1}{\varepsilon_1}} H_0 \tag{3.39}$$

where  $k_1$  is wave number of Medium 1 and  $\eta_1$  intrinsic impedance of the Medium 1. Substituting the (3.36)-(3.38) in (3.34) –(3.35) the incident electric field can be obtained and given in (3.40).

$$\tilde{E}_{i} = \left[ \sqrt{\frac{\mu_{1}}{\varepsilon_{1}}} H_{0} \left( -\hat{a}_{x} \frac{k_{1y}}{\omega \sqrt{\mu_{1} \varepsilon_{1}}} + \hat{a}_{y} \frac{k_{1x}}{\omega \sqrt{\mu_{1} \varepsilon_{1}}} \right) \right] e^{-jk_{1x}x - jk_{1y}y}$$
(3.40)

$$\tilde{E}_{i} = \left[ -\hat{a}_{x} \frac{k_{1y}}{\omega \varepsilon_{1}} + \hat{a}_{y} \frac{k_{1x}}{\omega \varepsilon_{1}} \right] H_{0} e^{-jk_{1x}x - jk_{1y}y}$$
(3.41)

The reflected field in phasor form in Medium 1 can be written in (3.41).

$$\tilde{H}_r = \hat{a}_z H_0 \Gamma e^{jk_{1x}x - jk_{1y}y} \tag{3.42}$$

The reflected electric field in the Medium 1 can be as follows:

$$\tilde{E}_{r} = \left[ \sqrt{\frac{\mu_{1}}{\varepsilon_{1}}} H_{0} \Gamma \left( -\hat{a}_{x} \frac{k_{1y}}{\omega \sqrt{\mu_{1} \varepsilon_{1}}} - -\hat{a}_{y} \frac{k_{1x}}{\omega \sqrt{\mu_{1} \varepsilon_{1}}} \right) \right] e^{jk_{1x}x - jk_{1y}y}$$
(3.43)

$$\tilde{E}_r = \left[ -\hat{a}_x \frac{k_{1y}}{\omega \varepsilon_1} - \hat{a}_y \frac{k_{1x}}{\omega \varepsilon_1} \right] H_0 \Gamma e^{jk_{1x}x - jk_{1y}y}$$
(3.44)

where  $\Gamma$  is reflection coefficient. The total magnetic field and electric field in Medium 1 are expressed as superposition of incident and reflected fields, respectively, as follows:

$$\tilde{H}_{1} = \hat{a}_{z} H_{0} \left( 1 + \Gamma e^{j2k_{1x}x} \right) e^{-jk_{1x}x - jk_{1y}y} \tag{3.45}$$

$$\tilde{E}_{1} = \left[ -\hat{a}_{x} \frac{k_{1y}}{\omega \varepsilon_{1}} \left( 1 + \Gamma e^{j2k_{1x}x} \right) + \hat{a}_{y} \frac{k_{1x}}{\omega \varepsilon_{1}} \left( 1 - \Gamma e^{j2k_{1x}x} \right) \right]$$
(3.46)

The total magnetic field and electric field in anisotropic medium is given in (3.46) and (3.47).

$$\tilde{H}_{2} = \hat{a}_{z} H_{0} \tau e^{-jk_{2}x^{z} - jk_{2}y}$$
(3.47)

$$\tilde{E}_{2} = \left(-\hat{a}_{x} \frac{k_{2y}}{\omega \varepsilon_{2} a} + \hat{a}_{y} \frac{k_{2x}}{\omega \varepsilon_{2} b}\right) H_{0} \tau e^{-jk_{2x}x - jk_{2y}y}$$
(3.48)

At x = 0 the tangent components of the **E** and **H** are continues and using the Snell law, refractive law one can obtain (3.48) and (3.49).

$$k_{2y} = k_{1y} = k_1 \sin \theta \tag{3.49}$$

$$\Gamma = \frac{k_{1x} - k_{2x}b^{-1}}{k_{1x} + k_{2x}b^{-1}}, \quad \tau = 1 + \Gamma = \frac{2k_{1x}}{k_{1x} + k_{2x}b^{-1}}$$
(3.50)

Snell reflection law  $(\theta_i = \theta_r)$  Snell refractive law  $\left(\frac{k_1}{k_2} = \frac{\sin \theta_t}{\sin \theta_i}\right)$  where  $\Gamma$  is reflection coefficient and  $\tau$  transmission coefficient. Substituting the (3.48) in (3.32), (3.50) can be obtained.

$$k_{2x} = \sqrt{k_1^2 b^2 - (k_{1y})^2 b^2} = b\sqrt{k_1^2 - (k_{1y})^2} = bk_{1x}$$
(3.51)

The parameter should be selected so that the reflection coefficient is zero  $\left(\Gamma = \frac{k_{1x} - k_{2x}b^{-1}}{k_{1x} + k_{2x}b^{-1}} = 0\right) \text{ for all incidence angles. For this condition } k_{2x} = bk_{1x} \text{ is enough.}$ 

If the parameters are selected as  $\varepsilon_1=\varepsilon_2$ ,  $\mu_1=\mu_2$ , d=b,  $a^{-1}=b$ , one can obtain  $k_1=k_2$  and  $\eta_1=\eta_2$ .

$$k_{2x} = \sqrt{k_1^2 b^2 - (k_{1y})^2 b^2} = b\sqrt{k_1^2 - (k_{1y})^2} = bk_{1x}$$
(3.52)

For all  $k_{\rm lx}$  values the reflection coefficient equal to zero. Thus, a non-reflective interface can be obtained at all incidence angles and frequencies. When a uniaxial medium with  $\varepsilon_2$  and  $\varepsilon_2$  and  $\varepsilon_2$  tensors is created, non-reflective wave transmission to Medium 2 occurs.

where  $s = \begin{bmatrix} s_x^{-1} & 0 & 0 \\ 0 & s_x & 0 \\ 0 & 0 & s_x \end{bmatrix}$ . s = 0 complex diagonal tensor,  $\mathcal{E}_1$  and  $\mathcal{H}_1$  are the electrical and

magnetic permeabilities of the isotropic medium adjacent to the UPML medium, respectively. The non-reflective feature is independent of the incident angle, polarization, and frequency of the incident wave [90].

#### 3.3.3 Discrete Uniaxial PML

TEz polarized wave has three field components  $E_x$ ,  $E_y$  and  $H_z$ . It is assumed that UPML is perpendicular to the x-plane. The FDTD method is based on discrete representations of Maxwell's equations. In the uniaxial medium, Ampere's law in matrix form given as follows:

$$\begin{bmatrix} \frac{\partial \tilde{H}_z}{\partial y} \\ -\frac{\partial \tilde{H}_z}{\partial x} \\ 0 \end{bmatrix} = j\omega \varepsilon_1 \begin{bmatrix} s_x^{-1} & 0 & 0 \\ 0 & s_x & 0 \\ 0 & 0 & s_x \end{bmatrix} \begin{bmatrix} \tilde{E}_x \\ \tilde{E}_y \\ 0 \end{bmatrix}$$
(3.54)

The second row (tangent to the boundary components) is derived from the standard FDTD update equations. However,  $E_x$  cannot be updated this way due to the non-linear frequency dependency of  $\mathcal{E}_{xx}$ . The  $E_x$  field component that perpendicular to the boundary can be updated in several ways. One of these ways updating the normal electric flux density  $D_x$  from the standard FDTD formulation and then  $E_x$  can be calculated from the relationship between  $D_x$  and  $E_x$  [99].

In the uniaxial medium, Faraday's law in matrix form is given in (3.54). The last row is obtained from the FDTD updating equations.

$$\begin{bmatrix} 0 \\ 0 \\ \frac{\partial \tilde{E}_{y}}{\partial x} - \frac{\partial \tilde{E}_{x}}{\partial y} \end{bmatrix} = j\omega \mu_{1} \begin{bmatrix} s_{x}^{-1} & 0 & 0 \\ 0 & s_{x} & 0 \\ 0 & 0 & s_{x} \end{bmatrix} \begin{bmatrix} 0 \\ 0 \\ \tilde{H}_{z} \end{bmatrix}$$
(3.55)

The FDTD update equations for  $D_x$ ,  $E_x$ ,  $E_y$  and  $H_z$  can be written as follows when the  $\frac{\sigma_x}{\varepsilon_1} = \frac{\sigma_x^*}{\mu_1}$  condition is satisfied for a compatible PML.

$$D_x^{n+1}(i+1/2,j) = D_x^n(i+1/2,j) + \frac{\Delta t}{\Delta y} \left( H_z^{n+1/2}(i+1/2,j+1/2) - H_z^{n+1/2}(i+1/2,j-1/2) \right)$$
(3.56)

$$E_{x}^{n+1}(i+1/2,j) = E_{x}^{n}(i+1/2,j) + \left(\frac{2\varepsilon_{0} + \sigma_{x}\Delta t}{2\varepsilon_{0}^{2}\varepsilon_{r}}\right)D_{x}^{n+1}(i+1/2,j) - \left(\frac{2\varepsilon_{0} - \sigma_{x}\Delta t}{2\varepsilon_{0}^{2}\varepsilon_{r}}\right)D_{x}^{n}(i+1/2,j)$$
(3.57)

$$E_{y}^{n+1}(i, j+1/2) = \left(\frac{2\varepsilon_{0} - \sigma_{x}\Delta t}{2\varepsilon_{0} + \sigma_{x}\Delta t}\right) E_{y}^{n}(i, j+1/2)$$

$$-\left(\frac{2\Delta t}{\varepsilon_{r}(2\varepsilon_{0} + \sigma_{x}\Delta t)\Delta x}\right) H_{z}^{n+1/2}(i+1/2, j+1/2)$$

$$+\left(\frac{2\Delta t}{\varepsilon_{r}(2\varepsilon_{0} + \sigma_{x}\Delta t)\Delta x}\right) H_{z}^{n+1/2}(i-1/2, j+1/2)$$
(3.58)

$$H_{z}^{n+1/2}(i+1/2,j+1/2) = \left(\frac{2\varepsilon_{0} - \sigma_{x}\Delta t}{2\varepsilon_{0} + \sigma_{x}\Delta t}\right) H_{z}^{n-1/2}(i+1/2,j+1/2)$$

$$+ \left(\frac{2\varepsilon_{0}\Delta t}{\mu_{0}\mu_{r}(2\varepsilon_{0} + \sigma_{x}\Delta t)\Delta y}\right) \left(E_{x}^{n}(i+1/2,j+1) - E_{x}^{n}(i+1/2,j)\right)$$

$$- \left(\frac{2\varepsilon_{0}\Delta t}{\mu_{0}\mu_{r}(2\varepsilon_{0} + \sigma_{x}\Delta t)\Delta y}\right) \left(E_{y}^{n}(i+1,j+1/2) - E_{y}^{n}(i,j+1/2)\right)$$
(3.59)

#### 3.3.4 Corner Regions

In the previous section, the condition of the wave coming to a single planar boundary is examined. However, for open region simulation in 2D-FDTD space, four sides of the computation domain must be restricted with UPML. In this case, UPML has 4 planar edges and 4 corner regions. A more general relationship is needed to eliminate uncertainty in corner regions that have more than one vertical interface.

In the corner regions Maxwell's curl equations can be written as (3.59).

$$\nabla \times \tilde{E} = -j\omega \mu_0 \mu_r \tilde{s} \tilde{H}$$
 (3.60)

$$\nabla \times \tilde{H} = j\omega \varepsilon_0 \varepsilon_r \tilde{s}\tilde{E}$$
 (3.61)

where 
$$\vec{s} = \begin{bmatrix} s_y/s_x & 0 & 0 \\ 0 & s_x/s_y & 0 \\ 0 & 0 & s_x s_y \end{bmatrix}$$
 and  $s_x = 1 + \sigma_x/j\omega\varepsilon_0$ ,  $s_y = 1 + \sigma_y/j\omega\varepsilon_0$  the

structural tensor is not uniaxial but anisotropic. The  $^{S_x}$  and  $s_y$  are related with x-plane and y-plane respectively. The FDTD update equations of the areas in the corner regions are obtained using the two-digit method used for perpendicular area components. Ampere's law in matrix form can be written as follows:

$$\begin{bmatrix} \frac{\partial \tilde{H}_z}{\partial y} \\ -\frac{\partial \tilde{H}_z}{\partial x} \\ 0 \end{bmatrix} = j\omega\varepsilon_1 \begin{bmatrix} s_y/s_x & 0 & 0 \\ 0 & s_x/s_y & 0 \\ 0 & 0 & s_x s_y \end{bmatrix} \begin{bmatrix} \tilde{E}_x \\ \tilde{E}_y \\ 0 \end{bmatrix}$$
(3.62)

Electric flux density is related to the electric field as given in (3.62).

$$\tilde{D}_{x} = \left(\frac{s_{y}}{s_{x}}\right) \tilde{E}_{x} \tag{3.63}$$

$$\tilde{D}_{y} = \left(\frac{s_{x}}{s_{y}}\right) \tilde{E}_{y} \tag{3.64}$$

The partial differential equations given in (3.62) are in the frequency domain and by using the  $j\omega \to \frac{\partial}{\partial t}$  transformation, the equations can be expressed in the time domain. Substituting the (3.63) –(3.64) in (3.62) the partial differential equations that are related to the magnetic field and magnetic flux density in time domain can be obtained.

$$\frac{\partial H_z}{\partial y} = \varepsilon_1 \frac{\partial}{\partial t} D_x \tag{3.65}$$

$$-\frac{\partial H_z}{\partial x} = \varepsilon_1 \frac{\partial}{\partial t} D_y \tag{3.66}$$

Using the (3.62) the time domain partial differential equations associated with the electric field strength components and the electric flux density components are obtained as follows:

$$\frac{\partial}{\partial t} D_x + \frac{\sigma_x}{\varepsilon_0} D_x = \left( \frac{\partial}{\partial t} E_x + \frac{\sigma_y}{\varepsilon_0} E_x \right)$$
 (3.67)

$$\frac{\partial}{\partial t} D_{y} + \frac{\sigma_{y}}{\varepsilon_{0}} D_{y} = \left( \frac{\partial}{\partial t} E_{y} + \frac{\sigma_{x}}{\varepsilon_{0}} E_{y} \right)$$
(3.68)

Faraday's law in matrix form can be written as follows:

$$\begin{bmatrix} 0 \\ 0 \\ \frac{\partial \tilde{E}_{y}}{\partial x} - \frac{\partial \tilde{E}_{x}}{\partial y} \end{bmatrix} = -j\omega\mu_{1} \begin{bmatrix} s_{y}/s_{x} & 0 & 0 \\ 0 & s_{x}/s_{y} & 0 \\ 0 & 0 & s_{x}s_{y} \end{bmatrix} \begin{bmatrix} 0 \\ 0 \\ \tilde{H}_{z} \end{bmatrix}$$
(3.69)

The magnetic flux density component is related to the magnetic field strength component as specified in (3.69).

$$\tilde{B}_z = \mu_1 s_v \tilde{H}_z \tag{3.70}$$

Substituting the (3.69) in (3.67)-(3.68) the time domain partial differential equation associated with the electric field strength components and the magnetic flux density components is obtained as follows.

$$\frac{\partial E_x}{\partial x} - \frac{\partial E_y}{\partial y} = \frac{\partial}{\partial t} B_z + \frac{\sigma_x}{\varepsilon_0} B_z$$
(3.71)

Using the (3.69) the time domain partial differential equations associated with magnetic field strength components and magnetic flux density components are obtained as follows:

$$\frac{\partial}{\partial t}B_z = \mu_1 \frac{\partial}{\partial t}H_z + \mu_1 \frac{\sigma_y}{\varepsilon_0}H_z$$
(3.72)

Finite difference time domain approximations of partial differential equations given in (3.63) -(3.64) are obtained as follows [90]:

$$D_{x}^{n+1}(i+1/2,j) = D_{x}^{n}(i+1/2,j) + \frac{\Delta t}{\varepsilon_{1}\Delta y} \left(H_{z}^{n+1/2}(i+1/2,j+1/2) - H_{z}^{n+1/2}(i+1/2,j-1/2)\right)$$
(3.73)

$$E_{x}^{n+1}(i+1/2,j) = \left(\frac{2\varepsilon_{0} - \sigma_{y}\Delta t}{2\varepsilon_{0} + \sigma_{y}\Delta t}\right) E_{x}^{n}(i+1/2,j) + \left(\frac{2\varepsilon_{0} + \sigma_{x}\Delta t}{2\varepsilon_{0} + \sigma_{y}\Delta t}\right) D_{x}^{n+1}(i+1/2,j) - \left(\frac{2\varepsilon_{0} - \sigma_{x}\Delta t}{2\varepsilon_{0} + \sigma_{y}\Delta t}\right) D_{x}^{n}(i+1/2,j)$$

$$(3.74)$$

# 3.4 Dielectric Properties of Concrete

Concrete is a heterogeneous material containing cement, water, fine aggregate, coarse aggregate and air. Aggregates are used as filling material in concrete and as a result of the reactions between cement and water, a mixture that holds the materials in the concrete together is formed. Concrete is brittle by nature and is resistant to compressive stresses and has low resistance to tensile stresses. Iron is used in concrete to increase the resistance of concrete to tensile stresses. Although the concrete has a heterogeneous structure, the curing time after production, the drying method (oven drying, air drying) and the environmental conditions during its use affect the physical properties of the concrete. In addition to other properties of concrete, its dielectric properties are the most influential feature in microwave radar inspection and simulation [105].

The dielectric property of a material relative to free space is a complex parameter consisting of its permittivity. The real part of this parameter is called the dielectric constant and the imaginary part is called the loss factor.

$$\varepsilon_r = \varepsilon_r' - j\varepsilon_r'' \tag{3.75}$$

$$\varepsilon_r = \varepsilon_r' (1 - j \tan \delta) \tag{3.76}$$

The dielectric properties of a material can be expressed by (3.75) and (3.76).

While the real part indicates the amount of energy that can be stored in a material in the form of an electric field, the imaginary part or loss factor is a parameter that expresses how much of the energy given to the material is consumed as heat in the material [106]. The loss factor can be expressed as:

$$\varepsilon'' = \frac{\sigma}{2\pi f \,\varepsilon_0} \tag{3.77}$$

Where  $\sigma$  is conductivity and f is frequency. The dielectric loss factor or loss tangent expresses the measure of the conversion of electromagnetic energy into heat energy due to dielectric losses and is the ratio of the dielectric loss factor to the dielectric constant and given as in (3.78) and  $\omega$  is the angular frequency of the wave.

$$\tan \delta = \frac{\varepsilon''}{\varepsilon'} = \frac{\sigma}{\omega \varepsilon'}$$
 (3.78)

Using the equation (3.76), it can be concluded that if  $\tan \delta \ll 1$  the medium is a good insulator, and if  $\tan \delta \gg 1$  the medium is a good conductor.

The dielectric constant of concrete sensitive to measurement frequency, water-to-cement ratio, moisture content, and measurement temperature [106]. Since the dielectric constant of water is high in the 0.1 GHz-20.0 GHz microwave frequency range, both the loss factor and the dielectric constant increase as the moisture level in a concrete sample increase. Concretes used in experimental measurements can be grouped according to their moisture content as saturated, wet, oven-dried or airdried. In concretes at the same humidity level, the dielectric constant varies depending on the frequency, but in cases where the concrete is dry, the dielectric constant is independent of the frequency [107, 108]. Considering the state of dielectric constant when the concrete is dry and when the moisture content of the concrete is highest, it has been observed that the dielectric constant varies between 5 and 25 [75]. The dielectric constant does not change depending on the frequency when the concrete is dry [109, 110]. After the concretes used in our study were molded, they were kept in the curing tank for 28 days and dried in air for more than six months.

# CONCRETE TYPES AND SIMULATION SETUPS

Concrete structures have a wide area of use in all areas of our lives. Since they have many different areas of use, their geometry changes depending on where they are used. Although its geometric shapes change according to the usage areas, it is also used in combination with different materials. When concrete material is used in areas that come into contact with water, such as bridge legs, it is used together with composite materials, making it usable for a longer time. Concrete materials used in building columns are reinforced with rebar. In cases where concrete is used on the building wall, concrete material can be used together with brick and mortar. In some cases, even when the concrete is newly prepared, defects such as being porous or having voids are observed. In concretes that have been used for a long time, exposed to strong energy such as earthquakes or weathered due to environmental factors, cracks are observed on the surface or in the interior [111].

In this section, concrete structures with cracks on the surface or inside, concrete structures that form a layered environment with different materials, and cylindrical concrete structures are examined respectively, and simulation results are given [112].

#### 4.1 Surface Crack Definition

Some of the physical models representing the types of cracks that could be found in any concrete structure are created. The simulation geometry of these crack types is explained in detail under subheadings.

#### 4.1.1 Crack Definition

For defining the surface crack, rectangular step function is used that is defined mathematically in Equ (4.1). The rectangular step functions are added which are shrinking evenly and successively downward. The definition of the crack is obtained geometrically with the addition of functions and presented in Figure 4.1.

$$rect(t) = \begin{cases} 0, \ t < -a/2 \\ 1/a, \ -a/2 \le t \le a/2 \\ 0, \ t > a/2 \end{cases}$$
 (4.1)

Rectangles with centers on the same axis are used. Rectangles of equal height, but tapering downward, are added end to end to form a ladder shape. The aim here is to examine how the rebar near and far from the surface is visualized in a concrete sample with a surface crack that narrows as one goes deeper.

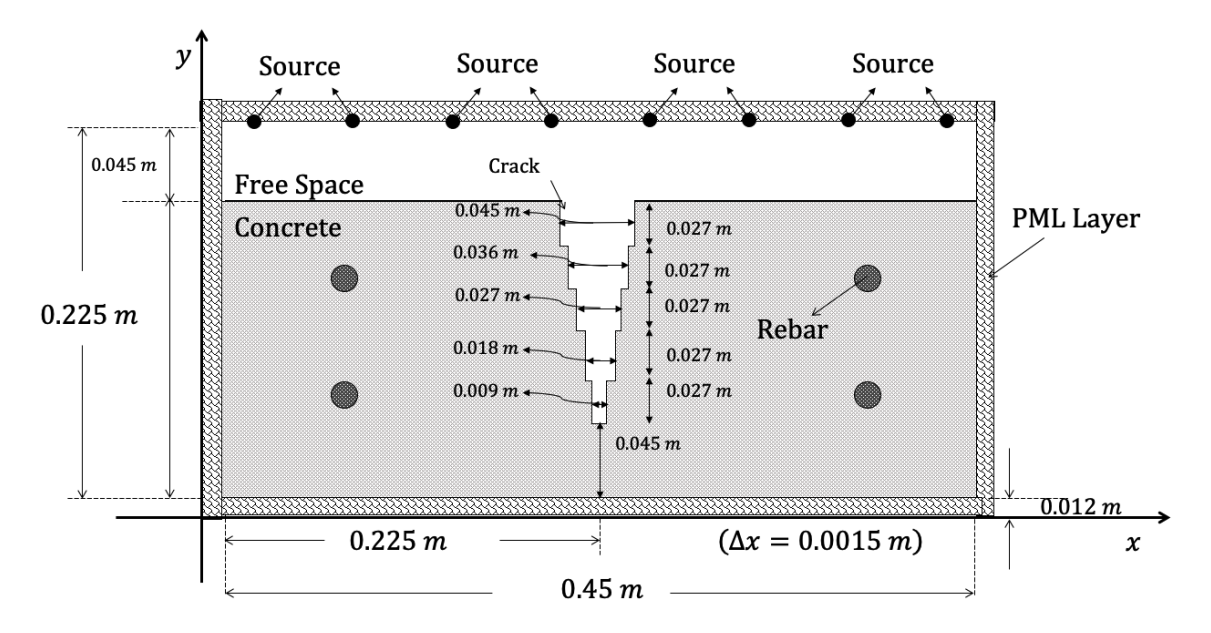


**Figure 4.1** Surface Crack Model Defined by Rectangular Step Function [114]

The dimensions of the numerical domain are 300 grids in other words 300-unit cell in the x-axis and 150 grids in the y-axis. For the spatial increment in the simulation domain, uniform discretization in space is appealed with  $\Delta x = \Delta y = 0.0015m$  and so computation domain physically corresponds to a rectangular region of  $0.45m \times 0.225m$ . In addition to these, domain contains four embedded rebar (radius of rebar is 8 mm). The operation frequencies for simulations are 1.5 GHz, 3.0 GHz and 6.0 GHz.

Another surface crack definition is made by moving the same centered circles on triangle edges. The tangent point of one of the circles is the center of another the successive circle in Figure 4.2. Although this surface crack is shallower than the previous surface crack, the area it covers on the surface is wider.

The positions of the rebars in the concrete and the concrete thickness are the same, only the shape and depth of the crack are different. Thanks to this difference in the shape and depth of the crack, the time needed to detect the rebars and the response of the electromagnetic wave sent from the source when it encounters the concrete medium can be compared. In both simulation setups, the computational domain is surrounded by the PML layer [94]. Thus, the electromagnetic wave coming to the calculation area is absorbed and re-entering the calculation area is prevented.

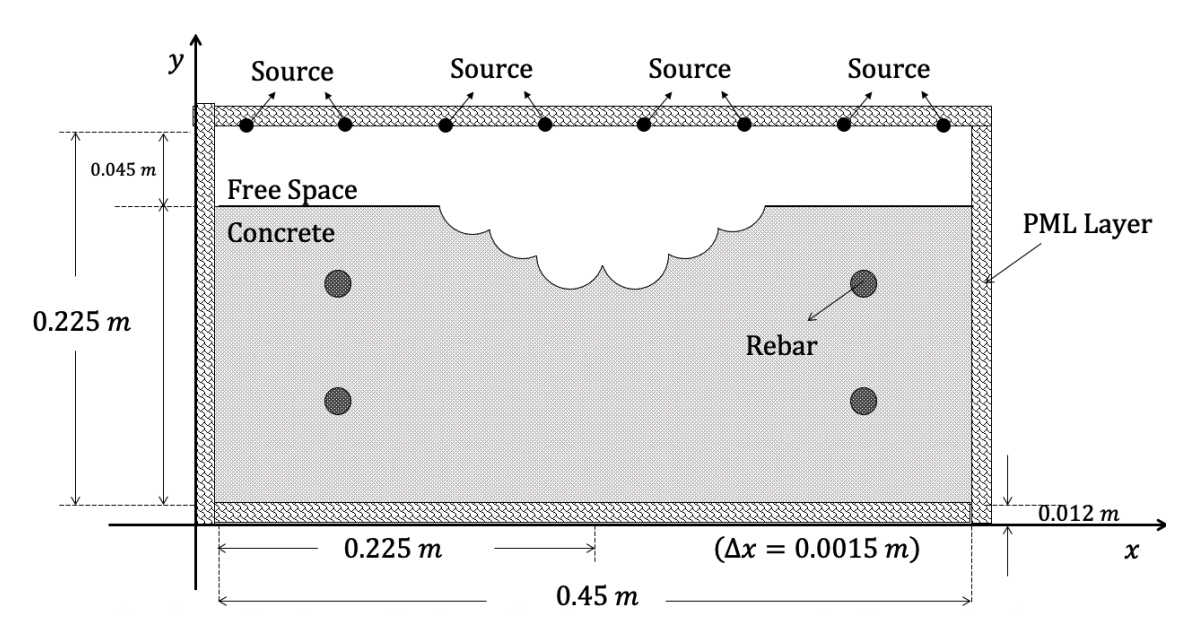


Figure 4.2 Surface Crack Model Defined by Dynamic Geometry [114]

The dimensions of the numerical domain are 300 grids in the *x*-axis and 150 grids in the *z*-axis. In the reality the computation domain corresponds to a rectangular region of  $0.45m \times 0.225m$  and  $\Delta x = \Delta y = 0.0015m$ . The experimental setup of Case B contains four embedded rebar (radius of rebar is 8 mm). The operation frequencies for simulations are 1.5GHz, 3.0 GHz, and 6.0 GHz.

#### 4.1.2 Simulation Results for Surface Cracks

The numerical simulation experiments are excited by TE and TM waves, and all electric and magnetic components are calculated for Case A to Case C.  $E_x$  field distribution from simulations using TE wave and  $E_z$  field distributions from simulations using TM wave are shown and compared. In the presented cases, the maximum wave velocity is equal to the speed of light propagated along with the free space [90]. The simulation results are obtained at 1.5 GHz, 3.0 GHz and 6.0 GHz

frequencies. The state of the field distributions changes according to the time steps. Results are presented with the best visibility of cracks, defects and rebars. The operation frequencies for simulations are 1.5 GHz, 3.0 GHz, 6.0 GHz and some of the results at specific times are given.

Simulation results are given for Case A function as follows:

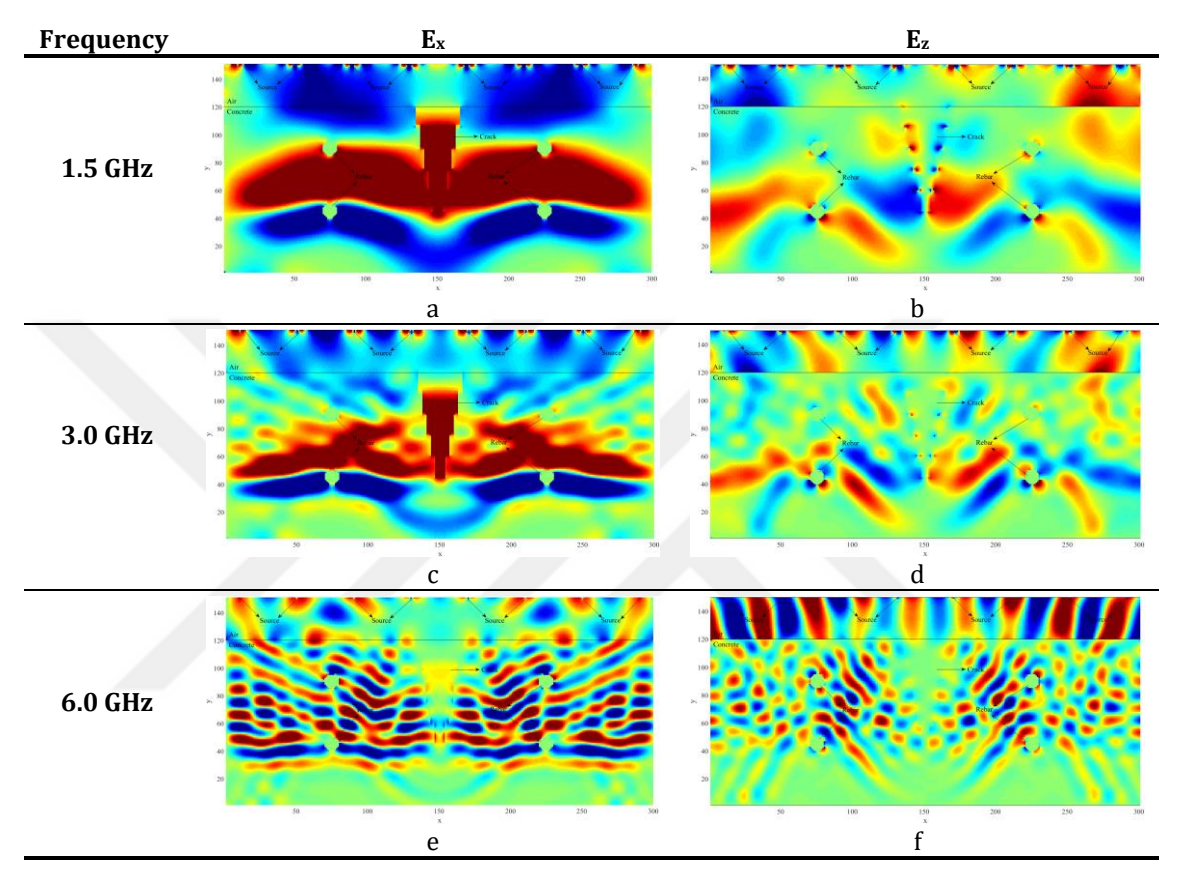


**Figure 4.3** Simulation Result for Case A at 600-Time Step: (a)  $E_x$  Field Distribution for 1.5 GHz, (b)  $E_z$  Field Distribution for 1.5 GHz, (c)  $E_x$  Field Distribution for 3.0 GHz, (d)  $E_z$  Field Distribution for 3.0 GHz, (e)  $E_x$  Field Distribution for 6.0 GHz, (f)  $E_z$  Field Distribution for 6.0 GHz [114]

Six different simulation results are given in Figure 4.3 for Case A. The thickness of the concrete and free space is 0.18 m and 0.045m, respectively. The simulation results for 1.5 GHz colors are more distinct, so crack and rebar are seen clearly in Figure 4.3a. When we compare the frequencies in the same time step for the  $E_x$  field distribution, the 1.5 GHz frequency is more suitable than the 3.0 GHz and 6.0 GHz frequencies. Figure 4.3a is a more reasonable result than Figures 4.3c and 4.3e.  $E_z$  field distribution obtained from TM mode at 1.5 GHz, 3.0 GHz and 6.0 GHz are given respectively in Figure 4.3b, Figure 4.3d and 4.3f. The variation of the waves

propagating from the air to the concrete appears to be more apparent in TM mode. On the other hand, rebars can be easily viewed in any situation.

Simulation results are given for Case B geometry as follows:

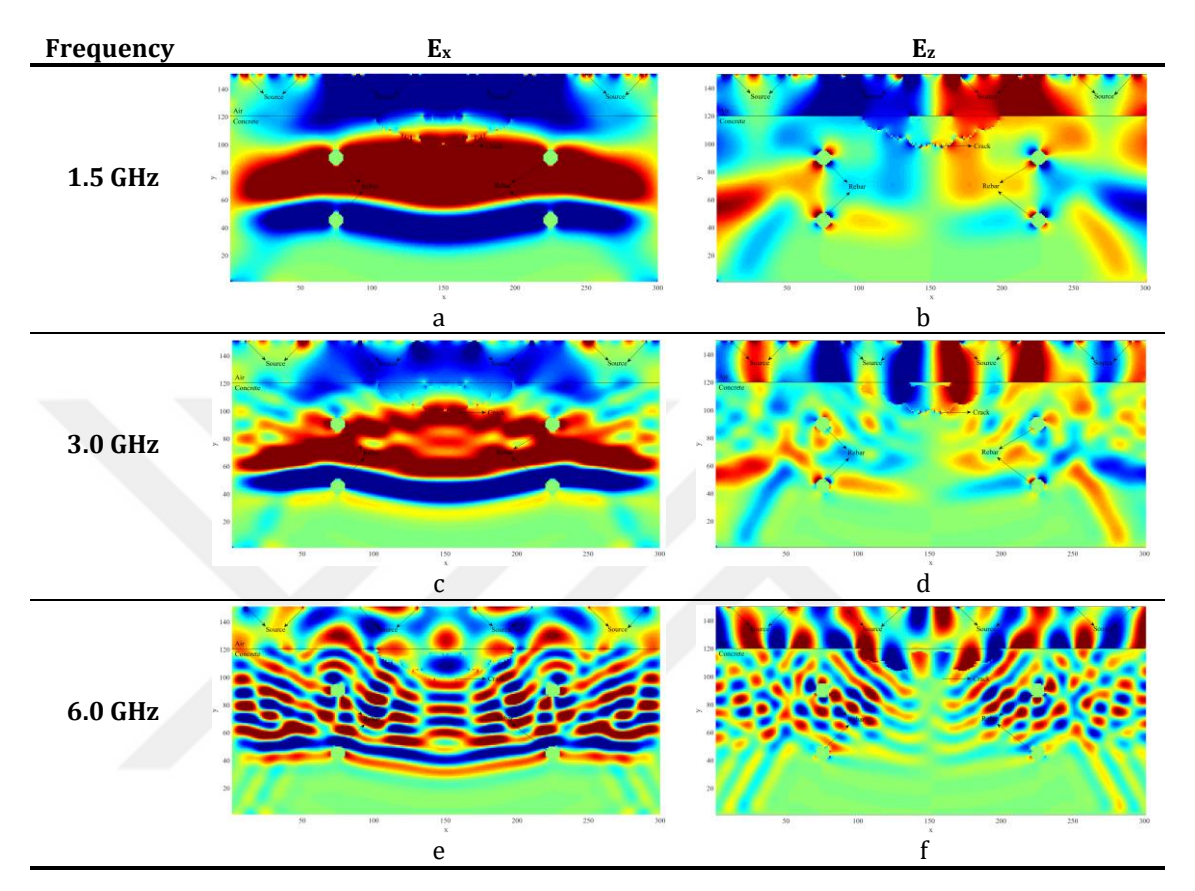


**Figure 4.4** Simulation Result for Case B at 600-Time Step: (a)  $E_x$  Field Distribution for 1.5 GHz, (b)  $E_z$  Field Distribution for 1.5 GHz, (c)  $E_x$  Field Distribution for 3.0 GHz, (d)  $E_z$  Field Distribution for 3.0 GHz, (e)  $E_x$  Field Distribution for 6.0 GHz, (f)  $E_z$  Field Distribution for 6.0 GHz [114]

As well as the simulation result given for Case A, the result is also obtained for Case B. The thickness of the concrete and free space is 0.18 m and 0.045 m, respectively. Although the rebars can be displayed in all results, the best result is obtained in Figure 4.4a. The transmission of the EM wave from one medium to another can be observed better in the field distribution obtained from TM mode. Since the crack in Case B is closer to the surface than in Case A and the TM mode is more suitable for observing the transition of the wave from the air to the concrete, the surface crack appears to be more appropriate in Figure 4.4b. Although the irons can be distinguished well in Figure 4.4c, the surface crack is not obvious. In Figure 4.4d,

although crack can be seen, the appearance of the rebars is not as clear as other shapes. At the same frequency, when the figures obtained from the TE and TM mode are compared, that is, when Figure 4.4e and Figure 4.4f are compared, the rebars appear more clearly in the results obtained from the TE mode. The best result for rebar detection is TE mode at 1.5 GHz frequency, and the best result for concrete detection is TM mode at 1.5 GHz frequency.

## 4.2 Interior Crack Definition

Internal fractures in concrete structures are damages that occur as a result of sudden energy changes such as earthquakes or as a result of situations such as collapse on the ground where the concrete structure is located. It poses a great risk for the safety of concrete structures as it is not possible to detect from the outside such as surface cracks. For these reasons, the detection of internal cracks is very important for both the safety of people and the service life of concrete structures.

## 4.2.1 Definition of the Interior Crack via Riemann Integral Domain

Interior concrete crack definition is made taking advantage of Riemann integral domain, in other words, the domain that is under a curve. Firstly, the area under the curve is defined using the Riemann integral expression, and then this definition is extended to the region expression between two curves. The area between the two curves is considered as an air-filled crack in simulations. To simulate this crack, which is the air-filled area, the integral of the function that assumed as a crack curve is used. The Riemann integral of a function requires the calculations of the area by dividing it into rectangles for this purpose. If one rectangle is used, the rudest approximation is achieved. But approximating the actual value of the area between two curves and making better refinements to the area, more rectangles should be added. These statements can be expressed mathematically as such: If the number of subintervals is increased, a more realistic area definition is made.

This statements can be expressed mathematically as such: f is a bounded function on [a,b], P is a [a,b] partition of and a partition of an interval [a,b] on the real axis can be defined as finite sequence  $x_0, x_1, x_2, ..., x_k$  of real numbers such that

 $a=x_0 < x_1 < x_2 < ... < x_k = b$ . P can be denotable as a set  $P=\{a=x_0,x_1,x_2,...,x_n=b\}$ . In other words, a partition of a compact interval I=[a,b] is a strictly increasing sequence of real numbers starts from  $x_0=a$  point and ends at  $x_k=b$ . Each interval of  $I\in[x_i,x_{i+1}]$  section will be referred to as a subinterval of X. If the number of subintervals is increased, a more realistic area definition is made. The subintervals are completed to rectangles from the bottom or top after dividing the area under the function curve into subintervals. Completing the sub-intervals to the rectangles from the bottom or using the minimum value of f(x) Lower Darboux Sum is obtained. In a similar way completing the subintervals to the rectangles from the top or using the maximum value of f(x) Upper Darboux Sum is obtained.

Namely, assuming that 
$$S \subseteq [a,b]$$
,  $m = (f,S) = \inf\{f(x): x \in S\}$  and  $M = (f,S) = \sup\{f(x): x \in S\}$ .

Lower Darboux Sum, Upper Darboux Sum and then transition to integral domain are given in the following equations group, respectively.

$$L(f,P) = \sum_{k=1}^{n} m(f,[t_{k-1},t_k]).(t_k - t_{k-1})$$
(4.2)

$$U(f,P) = \sum_{k=1}^{n} M(f,[t_{k-1},t_k]).(t_k - t_{k-1})$$
(4.3)

$$L(f,P) = m_1(t_1 - t_0) + m_2(t_2 - t_1) + \dots + m_n(t_n - t_{n-1})$$
(4.4)

$$U(f,P) = M_1(t_1 - t_0) + M_2(t_2 - t_1) + \dots + M_n(t_n - t_{n-1})$$
(4.5)

$$L(f) = \sup \{ L(f, P) : P \text{ is a partition of } [a, b] \}$$
 (4.6)

$$U(f) = \inf \{ U(f, P) : P \text{ is a partition of } [a, b] \}$$
(4.7)

$$\int_{a}^{b} f(x)dx = L(f) = U(f)$$
(4.8)

Related graphics are showed in Figure.4.5.

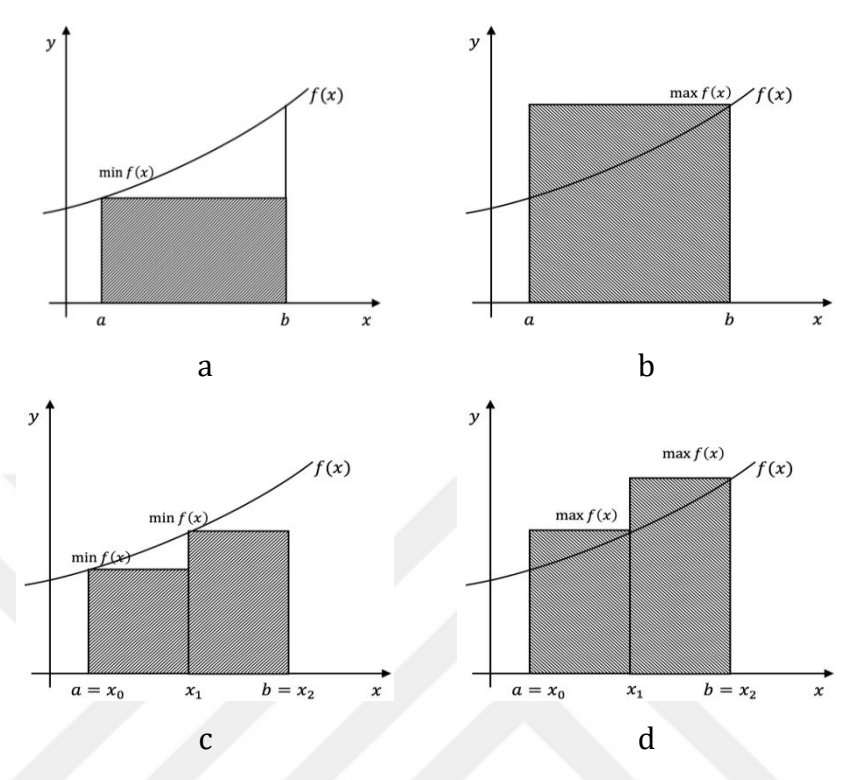


Figure 4.5 Riemann Integral Definition: Rude Partition

The subintervals are completed to rectangles from the bottom as in Figures 4.5 (a, c) or top as in Figures 4.5 (b, d) after dividing the area under the function curve into subintervals. Figures 4.5 (a, b) are the rudest approximation, Figures 4.5 (c, d) are a little better, but Figures 4.6 (a, b) are the best since calculating the area under the curve n piece of the rectangle are considered [113].

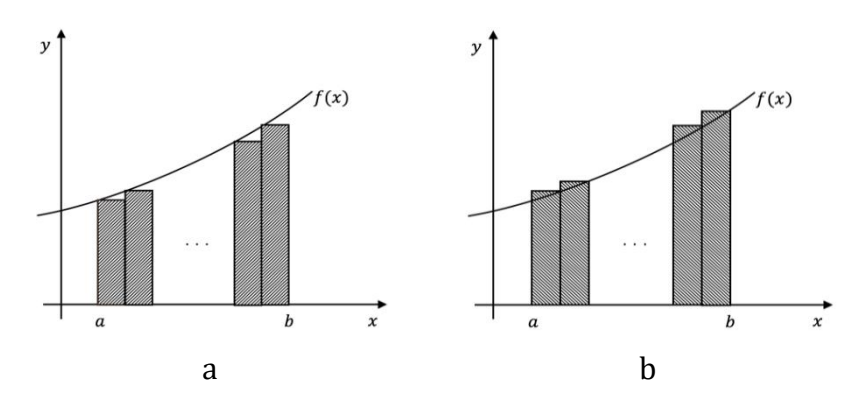
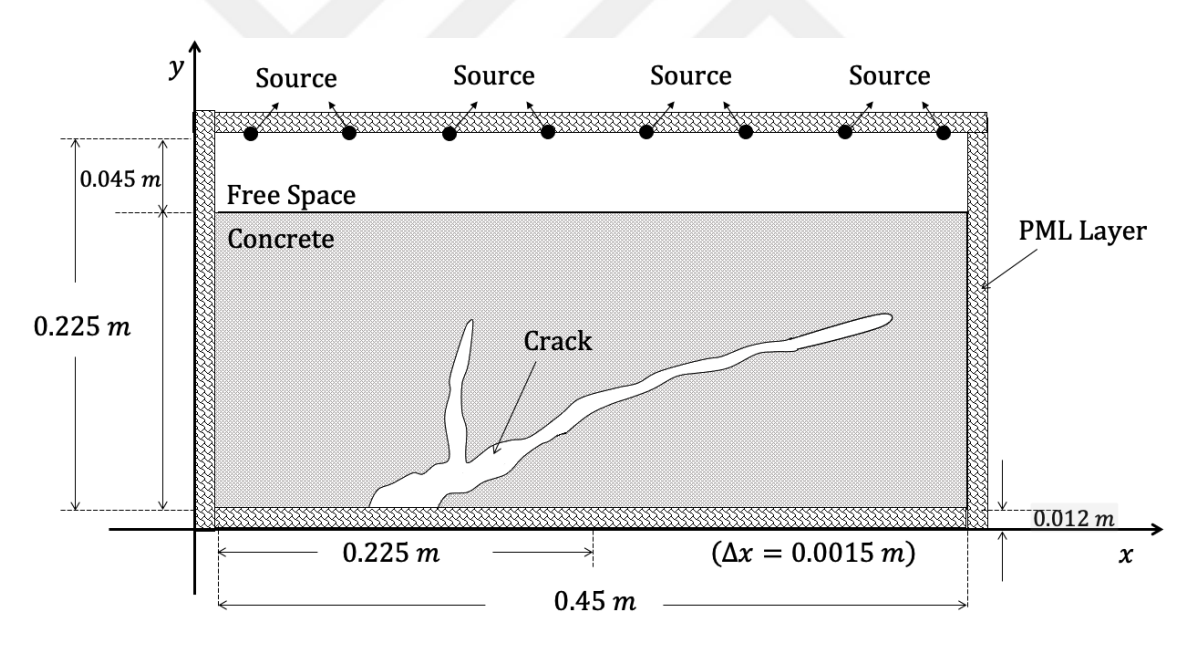


Figure 4.6 Riemann Integral Definition: Thin Partition

This means after dividing the curve expressed by the function into subintervals, completing the rectangle from the top and completing the rectangle from the bottom is almost same meaning. Electric field and magnetic field are computed with FDTD at all these subdomains [114].

As a result of these definitions, in Case C the most realistic crack explanation that can be encountered in any concrete structure is made and this type of crack refers to a branching internal crack caused by various external factors. The crack expressed in this simulation model is an internal crack and cannot be physically seen from the outside. For Case C the dimensions of the computational domain are 300 grids in the *x*-axis and 150 grids in the *y*-axis, and this physically corresponds to a rectangular region of  $0.45m \times 0.225m$  and  $\Delta x = \Delta y = 0.0015m$ . 0.045m of the computation domain is air, the rest of the domain in other words, thickness of the concrete is 0.18m. The simulation experiment for Case C is given in Figure 4.7.



**Figure 4.7** Interior Crack Model [114]

The curve expressed by the function that represents the concrete crack or delamination physically is divided into subintervals. These subintervals have completed the rectangle from the top and the bottom. By doing so, rectangular subdomains are obtained, and then electric field and magnetic fields are computed

at all these subdomains with FDTD. The operation frequency for simulation is 6.0 GHz and some of results at specific times are given.

#### 4.2.2 Simulation Results for Interior Crack

Simulation results are given for Case C as follows:

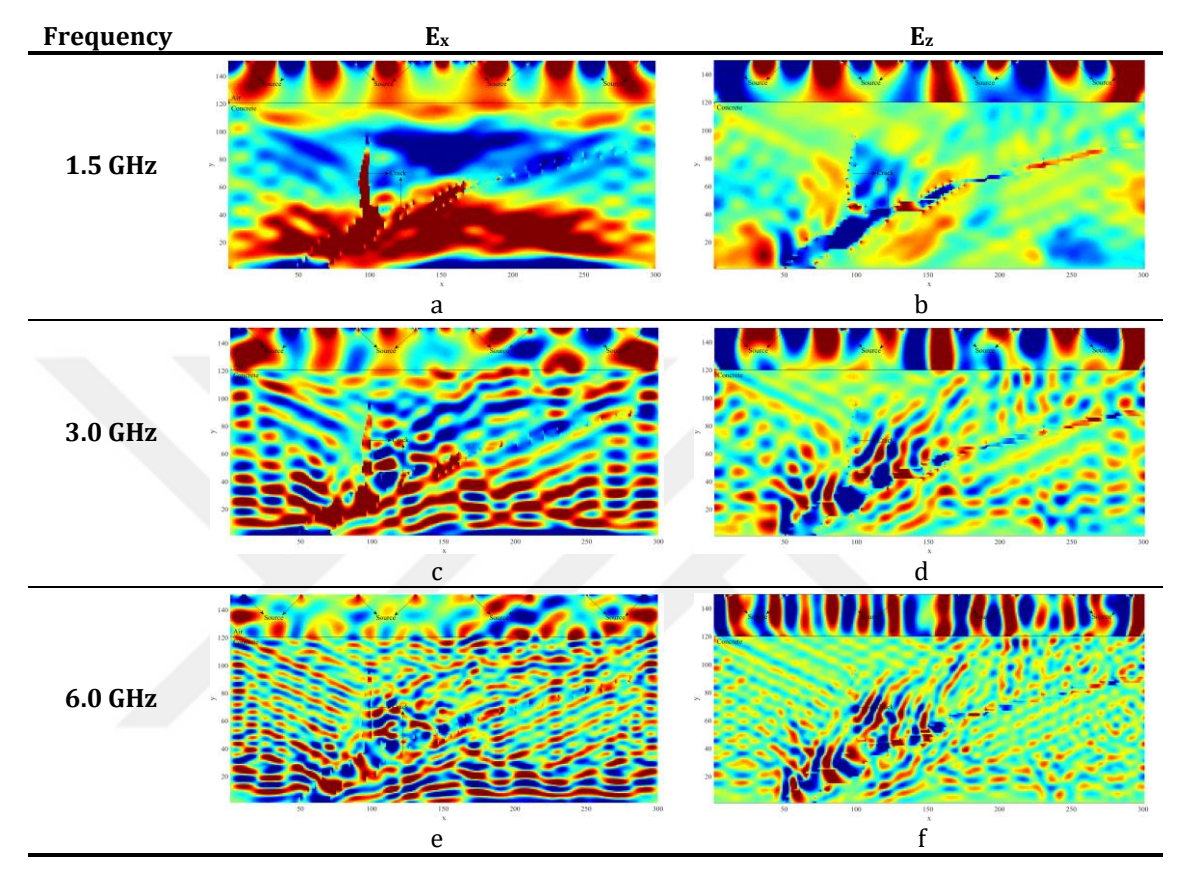


**Figure 4.8** Simulation Result for Case C at 700-Time Step: (a)  $E_x$  Field Distribution for 1.5 GHz, (b)  $E_z$  Field Distribution for 1.5 GHz, (c)  $E_x$  Field Distribution for 3.0 GHz, (e)  $E_x$  Field Distribution for 6.0 GHz, (f)  $E_z$  Field Distribution for 6.0 GHz [114]

Six different simulation results are given for Case C. The thickness of the concrete and free space is 0.18 m and 0.045 m respectively. In this experiment, rebar is not used to prevent the scattering of the wave in the structure so internal cracks are clearly visualized. The best result is in Figure 4.8a. In Figure 4.8b, the crack continuing to the right can be observed better. From the results of Figures 4.8c and 4.8d, it can be concluded that increasing frequency makes internal crack detection difficult. Although it is noticed that there is a damage in the concrete medium in Figure 4.8e and Figure 4.8f, which are simulation results at 6 GHz frequency, the

crack shape is not clear. Relatively lower frequencies give better results for internal crack detection.

The three-dimensional results of the simulation results of the surface cracks and internal crack described above are given in Figure 4.9.

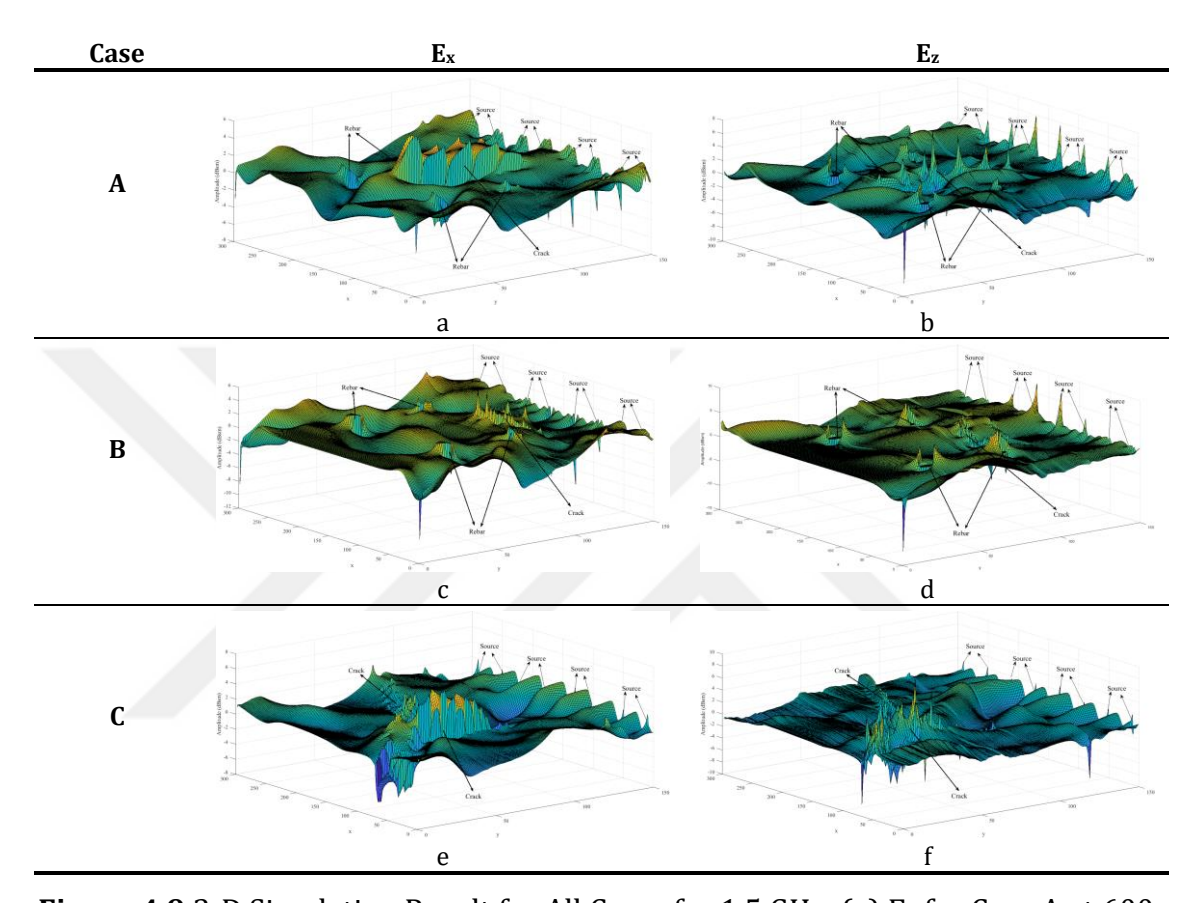


**Figure 4.9** 3-D Simulation Result for All Cases for 1.5 GHz: (a)  $E_x$  for Case A at 600-Time Step, (b)  $E_z$  for Case A at 600 Time Step, (c)  $E_x$  for Case B at 600 Time Step, (d)  $E_z$  for Case B at 600 Time Step, (e)  $E_x$  for Case C at 700 Time Step, (f)  $E_z$  for Case C at 700 Time Step [114]

In Figure 4. 9, 3-D simulation results at 1.5 GHz, for Case A, Case B and Case C are given respectively. Since the most suitable frequency for both crack and rebar detection is 1.5 GHz, it is preferred to provide 3-D figures of simulations at this frequency. The locations of the sources can be seen clearly in all results. In Case A, because the crack is deeper, the wave can propagate without attenuation too much, hitting the rectangular-shaped edges and creating a reflection. This situation can be seen in Figure 4.9a. While a similar situation can be observed for Case C as in Figure 4.9e, it could not be observed for Case B in Figure 4.9c. Since the EM wave is

scattered from rebars, they appear prominently in Figure 4.9a-d. As we know from the 2-D simulation results, the air-concrete separation can be determined more clearly in the Ez field distribution in Figures 4.9b, 4.9d, 4.9f.

# 4.3 Material Characterization of Rectangular Concrete Blocks Containing Different Materials

While examining concrete structures using microwave radar nondestructive testing technique, the main environment we focus on is concrete environments, but when we want to inspect a reinforced concrete building or a bridge, we encounter environments other than concrete. While there are materials such as iron and mortar on the walls of the concrete structure, paving stones can be found when examining the bridge decks. These paving stones can be either superficial or have a curved structure. In certain cases, the soil layer may be encountered. Considering all these situations, in addition to the concrete examination, it becomes necessary to examine the propagation of the electromagnetic wave in the case of mortar, pavement and soil layer. In this subsection, electromagnetic wave propagation in different materials with concrete structures will be examined and simulation setups containing different materials will be designed and results will be given.

## 4.3.1 Wave Propagation in Planarly Layered Media

The differences in the material properties of the four structural components (concrete, mortar, pavement, rebar) create challenging problems in predicting the behavior of the integrated structural system since concrete is a heterogeneous structure consisting of water, cement, sand, coarse aggregate and air in addition, the heterogeneous structure called mortar consists of water, cement, sand and air. Simple models, taken as cross-sections of large structures, can provide information about the behavior of a system that is lost in the details of more complex models and situations. Materials with many different dielectric properties have been successfully modeled in the same geometric structure. Therefore, the purpose of this section is to explain how the wave in microwave frequencies emitted from sources, in a layered environment composed of materials with different dielectric properties

and rebar. The response of layered media including pavement, concrete and soil is investigated by numerical simulation.

Planarly layered media is the simplest inhomogeneous media compared with the other inhomogeneous media. Electromagnetic waves propagating in a planarly layered, isotropic medium can be reduced to the studying of the two uncoupled scalar wave equations. These two uncoupled scalar wave equations can be reduced to one dimensional scalar wave equations.

When an electromagnetic wave comes to the plane boundary between two dielectric materials, some of the incident wave is transmitted while some is reflected. The boundary normal, incident wave, reflected wave, and transmitted wave lie in the same plane, and the plane is called the incidence plane or reflection plane. The i,r and t indices are used for incident wave, reflected wave and transmitted wave respectively. In addition, the material in which the incident and reflected wave propagates is indicated by i and r, and the material in which the transmitted wave is propagated with t. The electric field and magnetic field are given below for incident wave, reflected wave and transmitted wave.

$$\mathbf{E}_{i} = E_{i0} \exp\left\{i\left(\mathbf{k}_{i}.\mathbf{r} - \omega_{i}t\right)\right\} \tag{4.9}$$

$$\mathbf{E}_r = E_{r0} \exp\{i(\mathbf{k}_r \cdot \mathbf{r} - \omega_r t)\}$$
 (4.10)

$$\mathbf{E}_{t} = E_{t0} \exp\left\{i\left(\mathbf{k}_{t}.\mathbf{r} - \omega_{t}t\right)\right\} \tag{4.11}$$

$$\mathbf{B} = \frac{n}{c}\hat{\mathbf{k}} \times \mathbf{E} \tag{4.12}$$

The electromagnetic field must always satisfy the boundary conditions for  $\mathbf{E}, \mathbf{D}, \mathbf{B}$  and  $\mathbf{H}$  at every point between the two materials. For the boundary conditions to always hold,  $\omega$  must be the same for all three waves. In order for the boundary conditions to be valid at every point, the following equations must be satisfied.

$$\mathbf{k}_{r}.\Delta\mathbf{r} = \mathbf{k}_{r}.\Delta\mathbf{r} = \mathbf{k}_{r}.\Delta\mathbf{r} \tag{4.13}$$

$$k_i \cdot \sin \theta_i = k_r \cdot \sin \theta_r = k_t \cdot \sin \theta_t \tag{4.14}$$

Since the incident wave and reflected waves propagate in the same medium  $k_i = k_r$  and  $\sin \theta_i = \sin \theta_r$ , using the reflection law  $\theta_i = \theta_r$ . Using the  $k = \omega/v_p = \omega n/c$  and since the  $\omega$  is the same for all waves Equ. (4.12) can be obtained.

$$\mathbf{k}_{t}.\Delta\mathbf{r} = \mathbf{k}_{r}.\Delta\mathbf{r} = \mathbf{k}_{t}.\Delta\mathbf{r} \tag{4.15}$$

Using the reflection law and Snell law direction of the reflection wave and transmitted wave can be find. The polarization perpendicular to the plane of incidence is known as the  $(\sigma,s)$  or TE mode and is expressed by the  $(\bot)$  index in the equations. The polarization perpendicular to the plane of incidence is known as the  $(\pi,p)$  or TM mode and is expressed by the  $(\|\)$  index in the equations. Since TE mode means transverse electric,  $\mathbf E$  is perpendicular to the incidence plane, while TM mode means transverse magnetic,  $\mathbf B$  perpendicular to the incidence plane. In general, the incident electromagnetic wave can be considered as a superposition of two linearly polarized waves perpendicular and parallel to the incident plane. In transverse electromagnetic waves, both  $\mathbf E$  and  $\mathbf B$  are perpendicular to the direction of propagation  $\mathbf k$ .

When an electromagnetic wave comes to the interface between two dielectrics, the properties of the reflected and transmitted waves are determined by the boundary conditions of  ${\bf E}$  and  ${\bf B}$ . In the dielectric medium in which the incident wave exists, the electric and magnetic fields are the vectoral sum of the incident and reflected waves. In obtaining the boundary conditions for  ${\bf D}$  and  ${\bf B}$ , it is taken into account that the interface is very thin. Under this assumption free surface charge can be taken as  $\sigma_f=0$  Using the Gauss law for electric field  $\oint D.dS=0$  and magnetic field  $\oint B.dS=0$  together the Equ (4.16) and (4.17) can be obtained.

$$\varepsilon_i \left( \mathbf{E}_i + \mathbf{E}_r \right) \hat{\mathbf{e}}_1 = \varepsilon_t \mathbf{E}_t \hat{\mathbf{e}}_1 \tag{4.16}$$

$$(\mathbf{B}_{i} + \mathbf{B}_{r}) \cdot \hat{\mathbf{e}}_{1} = \mathbf{B}_{r} \cdot \hat{\mathbf{e}}_{1} \tag{4.17}$$

In obtaining the boundary conditions for  $\mathbf{E}$  and  $\mathbf{H}$  Ampere law  $\oint \mathbf{H} . d\mathbf{r} = \int \left( \mathbf{J}_f + \frac{\partial \mathbf{D}}{\partial t} \right) . d\mathbf{S}$  and Faraday law  $\oint \mathbf{E} . d\mathbf{r} = -\int \frac{\partial \mathbf{B}}{\partial t} . d\mathbf{S}$  are used together. On

the interface free charge density is  $\mathbf{J}_f = 0$ . Thus, the boundary conditions for  $\mathbf{H}$  and  $\mathbf{E}$  are calculated as below.

$$\left(\mathbf{B}_{i} + \mathbf{B}_{r}\right) / \mu_{i} \,\hat{\mathbf{e}}_{2} = \mathbf{B}_{t} / \mu_{t} \,\hat{\mathbf{e}}_{2} \tag{4.18}$$

$$(\mathbf{B}_i + \mathbf{B}_r)/\mu_i \cdot \hat{\mathbf{e}}_3 = \mathbf{B}_t/\mu_t \cdot \hat{\mathbf{e}}_3$$
 (4.19)

$$\left(\mathbf{E}_{t} + \mathbf{E}_{r}\right) \hat{\mathbf{e}}_{2} = \mathbf{E}_{t} \hat{\mathbf{e}}_{2} \tag{4.20}$$

$$\left(\mathbf{E}_{i} + \mathbf{E}_{r}\right)\hat{\mathbf{e}}_{3} = \mathbf{E}_{t}\hat{\mathbf{e}}_{3} \tag{4.21}$$

In the nonmagnetic and isotropic mediums for plane electromagnetic waves using the B = (n/c)E and  $\mu \approx \mu_0$  equality,  $\varepsilon \approx n^2 \varepsilon_0$  can be used.

How the electric field amplitudes of the reflected and transmitted waves will change according to the amplitude of the incident wave is determined by Fresnel's equations. In this case  $\mathbf{E}.\hat{\mathbf{e}}_1 = 0$ ,  $\mathbf{E}.\hat{\mathbf{e}}_3 = 0$  and  $\mathbf{B}.\hat{\mathbf{e}}_2 = 0$ . Thus, the equations between (4.16) -(4.121) are reduced to (4.22) -(4.24).

$$\left(E_i^{\perp} + E_r^{\perp}\right) \left(n_i/c\right) \cos\left(\pi/2 - \theta_i\right) = E_i^{\perp} \left(n_i/c\right) \cos\left(\pi/2 - \theta_i\right) \tag{4.22}$$

$$\left(-E_{i}^{\perp} + E_{r}^{\perp}\right) \left\lceil n_{i} / (c\mu_{0}) \right\rceil \cos \theta_{i} = -E_{t}^{\perp} \left\lceil n_{t} / (c\mu_{0}) \right\rceil \cos \theta_{t} \tag{4.23}$$

$$\left(E_i^{\perp} + E_r^{\perp}\right) = E_t^{\perp} \tag{4.24}$$

By solving (4.23) and (4.24) together, the following equations are obtained [114].

$$E_r^{\perp} = \frac{\cos\theta_i - (n_t/n_i)\cos\theta_t}{\cos\theta_i + (n_t/n_i)\cos\theta_t} E_i^{\perp}$$
(4.25)

$$E_t^{\perp} = \frac{2\cos\theta_i}{\cos\theta_i + (n_t/n_i)\cos\theta_t} E_i^{\perp}$$
(4.26)

Thanks to the Snell's law  $(n_i \sin \theta_i = n_i \sin \theta_i)$  cosine of the angle of refraction is given in (4.27).

$$\cos \theta_t = \sqrt{1 - n_i^2 / n_i^2 \sin^2 \theta_i} \tag{4.27}$$

Substituting the (4.27) into the (4.25) and (4.26) the reflection coefficient of perpendicular polarization can be obtained as (4.28).

$$r_{\perp} = \frac{E_r^{\perp}}{E_i^{\perp}} = \frac{\cos\theta_i - \sqrt{(n_t/n_i)^2 - \sin^2\theta_i}}{\cos\theta_i + \sqrt{(n_t/n_i)^2 - \sin^2\theta_i}}$$
(4.28)

$$t_{\perp} \equiv \frac{E_t^{\perp}}{E_i^{\perp}} = \frac{2\cos\theta_i}{\cos\theta_i + \sqrt{(n_t/n_i)^2 - \sin^2\theta_i}}$$
(4.29)

The transmittance coefficient for perpendicular polarization is given in (4.29). Similarly, the equations for parallel polarization are obtained as follows:

The equations  $\mathbf{B}.\hat{\mathbf{e}}_1 = 0$ ,  $\mathbf{B}.\hat{\mathbf{e}}_3 = 0$ , and  $\mathbf{E}.\hat{\mathbf{e}}_3 = 0$ , are reduced to (4.30)-(4.32).

$$\left(\varepsilon_{i} E_{i}^{\parallel} + \varepsilon_{i} E_{r}^{\parallel}\right) \sin \theta_{i} = \varepsilon_{t} E_{t}^{\parallel} \sin \theta_{t} \tag{4.30}$$

$$(E_i^{||} + E_r^{||})n_i = E_t^{||}n_t$$
(4.31)

$$\left(-E_i^{\parallel} + E_r^{\parallel}\right)\cos\theta_i = -E_t^{\parallel}\cos\theta_t \tag{4.32}$$

By solving (4.31) and (4.32) together, the following equations are obtained.

$$E_r^{\parallel} = \frac{(n_t/n_i)\cos\theta_i - \cos\theta_t}{(n_t/n_i)\cos\theta_i + \cos\theta_t} E_i^{\parallel}$$
(4.33)

$$E_t^{\parallel} = \frac{2\cos\theta_i}{(n_t/n_i)\cos\theta_i + \cos\theta_t} E_i^{\parallel}$$
 (4.34)

By substituting the (4.27) which is obtained by using the Snell's law into the (4.33) and (4.34) the reflection coefficient for parallel polarization can be obtained as follows:

$$r_{\parallel} = \frac{E_r^{\parallel}}{E_i^{\parallel}} = \frac{(n_t/n_i)^2 \cos \theta_i - \sqrt{(n_t/n_i)^2 - \sin^2 \theta_i}}{(n_t/n_i)^2 \cos \theta_i + \sqrt{(n_t/n_i)^2 - \sin^2 \theta_i}}$$
(4.35)

$$t_{\parallel} = \frac{E_{t}^{\parallel}}{E_{i}^{\parallel}} = \frac{2(n_{t}/n_{i})^{2} \cos \theta_{i}}{(n_{t}/n_{i})^{2} \cos \theta_{i} + \sqrt{(n_{t}/n_{i})^{2} - \sin^{2} \theta_{i}}}$$
(4.36)

The transmittance coefficient for parallel polarization is given in (4.36) [115].

## 4.3.2 Layered Media Definitions

The GPR method is a useful method that can be used to inspect construction structures and infrastructure. GPR systems also provide an important service for road surveys. For this purpose, asphalt, concrete, etc. determination of deformations in structures, road, etc. It is used to determine the voids under the structures, to control the quality of asphalt, and to map the thickness of asphalt and concrete pavements [116]. GPR systems, which can also be used in archaeological research, are used to locate objects and structures belonging to ancient civilizations. It is also used in archaeological field studies [117]. Another important area of use is the analysis of structures. In this context, it is used to display the iron reinforcement in columns and beams, to determine the existing building foundation type, and to investigate discontinuities in columns or beams. Finally, GPR systems are used in environmental research. For this purpose, it is used in underground pollution research, revealing filled areas and determining waste areas. Radio waves or microwaves, which are high-frequency waves, are used as a source in GPR. Frequency selection is made according to the depth of the research. A GPR system consists of transmit-receive antennas and a recording-analyzer. The transmitting antenna sends the electromagnetic wave underground. The receiving antenna detects the electromagnetic waves reflected from the underground and transmits them to the recording-analysis device. The signal sent underground is scattered, reflected and transmitted after it reaches objects with different dielectric properties. It is then recorded with the receiving antenna and recording-analyzer located on the surface. The GPR method has been used in many fields since its first use. Today, it is used in areas such as building and structural inspection, archeology, road and tunnel quality assessment, detection of gaps, pipe and cable detection, and satellite remote sensing [119, 121].

The two-dimensional computational domain is divided into cells of much smaller size than the wavelength. Six different simulations set up are introduced.

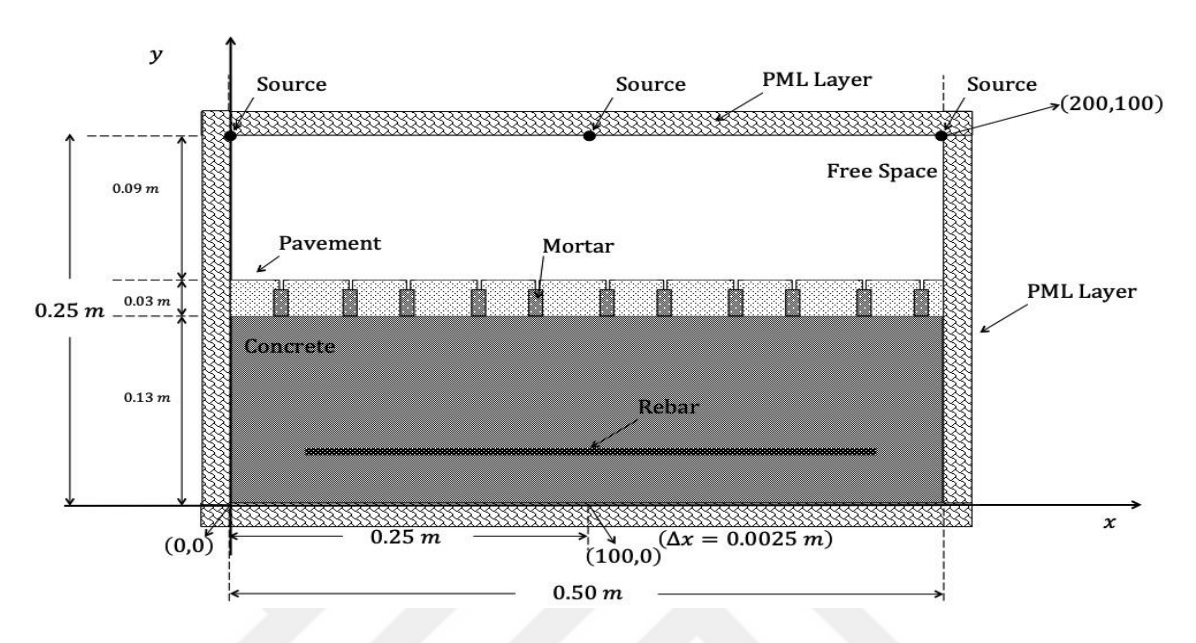


**Figure 4.10** Model A: Layered Media with Pavement, Mortar, Concrete and Horizontal Rebar [117]

In the first numerical experiment namely Model A in Figure 4.10, a two-layered rectangular specimen with pavement that contain mortar between and concrete including horizontal rebar is used to test the method. The thickness of the concrete is 0.13m, the height of the pavement 0.03 m, the height of the mortar 0.02m and extend of the free space in the y-axis is 0.09 m. The length of the rebar is 0.4 m. The entire computational domain is a rectangular region of  $0.5m \times 0.25m$ . The numerical domain is obtained by dividing into 200 grids in the *x*-axis and 100 grids in the *y*-axis,  $\Delta x = \Delta y = 0.0025m$ .

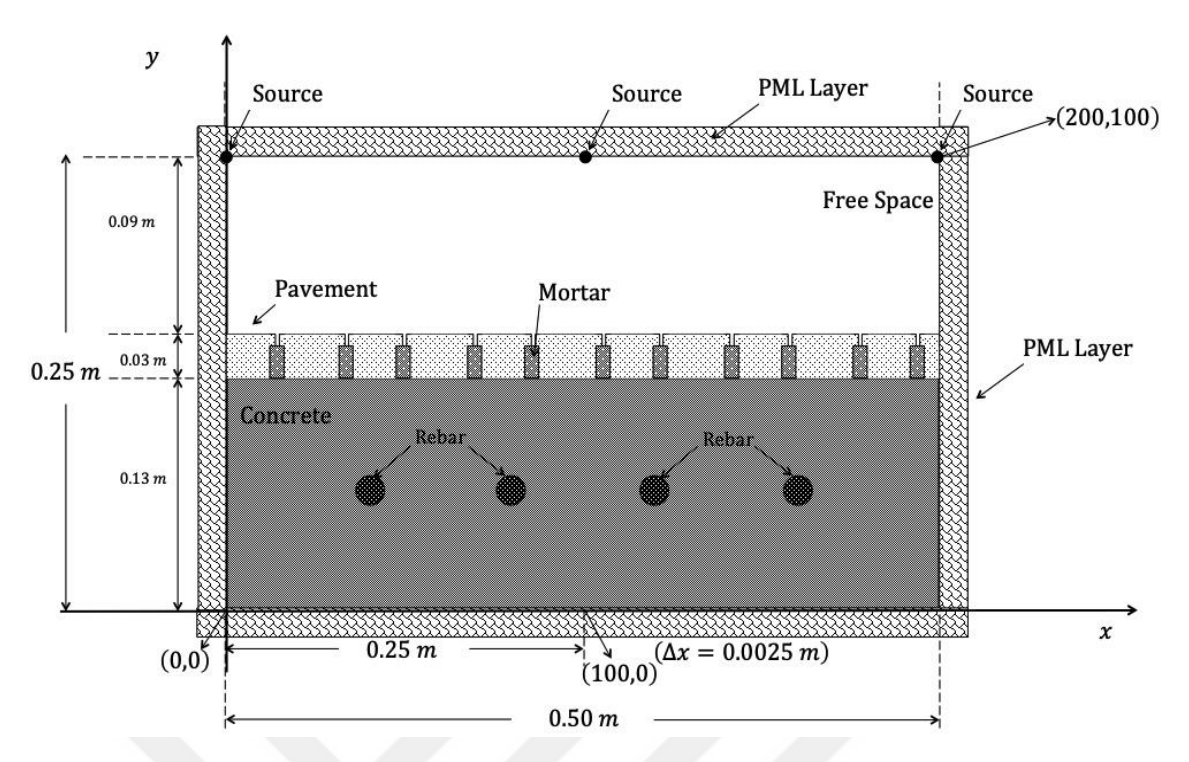


**Figure 4.11** Model B: Layered Media with Pavement, Mortar, Concrete and Vertical Rebar [117]

In Figure 4.11 physical model for Model B is introduced. a two-layered rectangular specimen with pavement that contain mortar between and concrete including horizontal rebar is used to test the method. The thickness of the concrete is 0.13 m, the height of the pavement 0.03 m, the height of the mortar 0.02 m and extend of the free space in the *y*-axis is 0.09 m. The characteristics of this physical model are the same as the Model A except for the location of the rebar. The diameter of each rebar is 0.015 m, distance between rebar and *x*-axis is equal and 0.05 m. The distances of the centers of the rebar to each other and to the calculation edge are equal and 0.1 m.

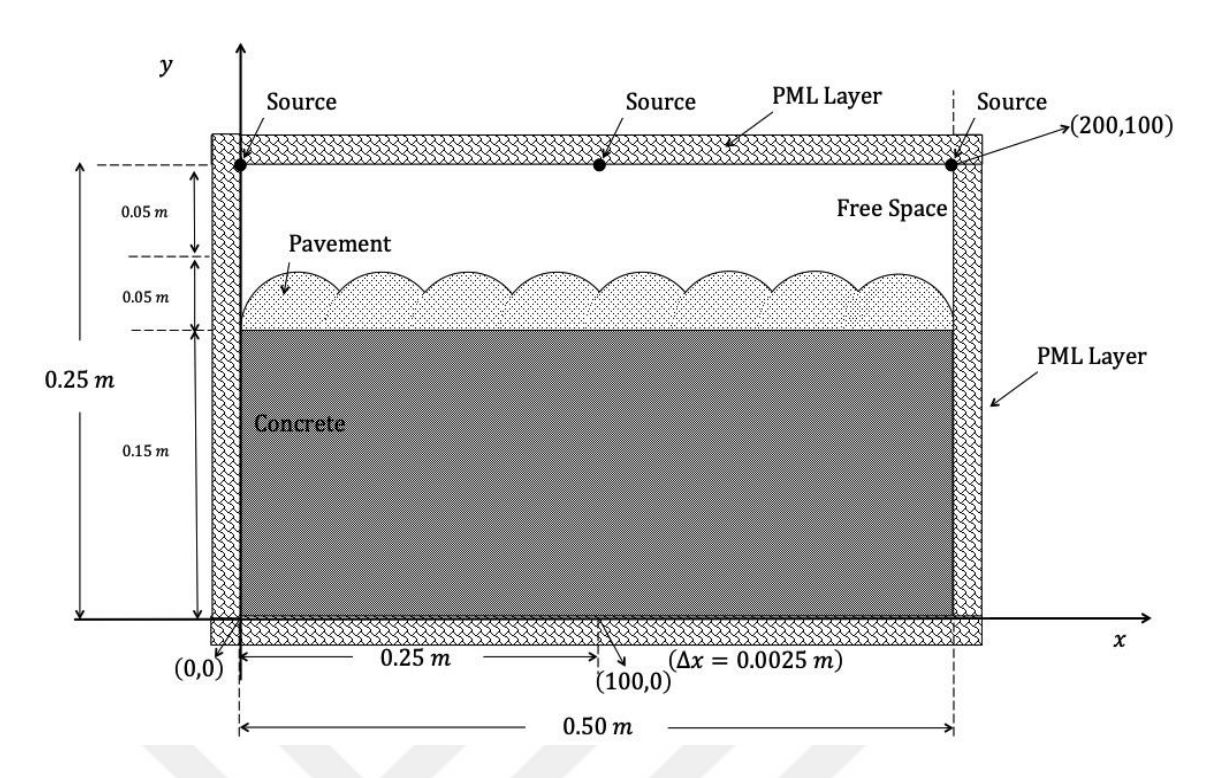


Figure 4.12 Model C: Layered Media with Circular Pavement and Concrete [117]

In Figure 4.12 the simulation setup for Model C is introduced. This model contains circular pavement on concrete layer, the thickness of the concrete is 0.15 m, the distance between maximum point of the pavement and interface of the concrete-pavement is 0.05 m. The computational domain is a rectangular region. The domain has 200 grids in the *x*-axis and 100 grids in the *y*-axis and  $\Delta x = \Delta y = 0.0025 m$ . The entire computational domain is a rectangular region of  $0.5 m \times 0.25 m$ .

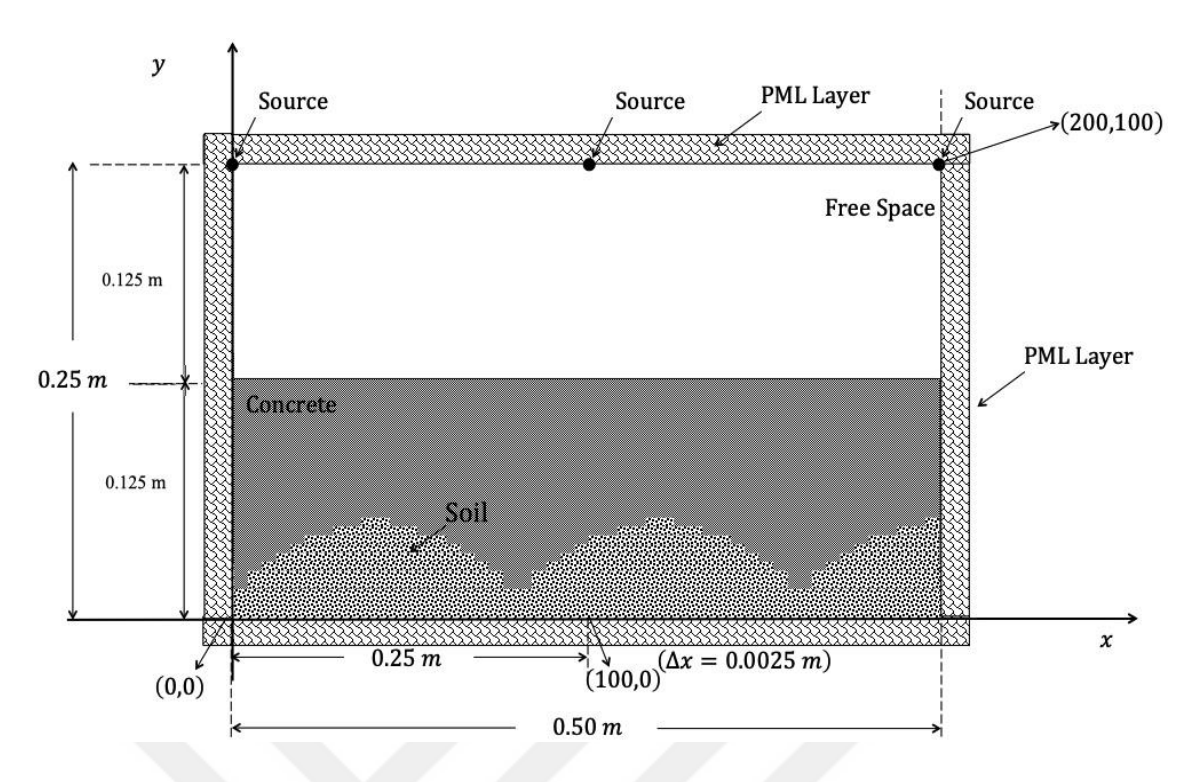


Figure 4.13 Model D: Layered Media with Concrete and Soil [117]

In Figure 4.13 the simulation setup for Model D is given, and this model consists of undulating soil surface under concrete layer. The maximum height of the area formed by soil and concrete is 0.125 m and the distance between x-axis and peak of the soil is 0.075 m. The entire computational domain is a rectangular region of  $0.5m \times 0.25m$ . The numerical domain is obtained by dividing into 200 grids in the x-axis and 100 grids in the y-axis,  $\Delta x = \Delta y = 0.0025m$ .

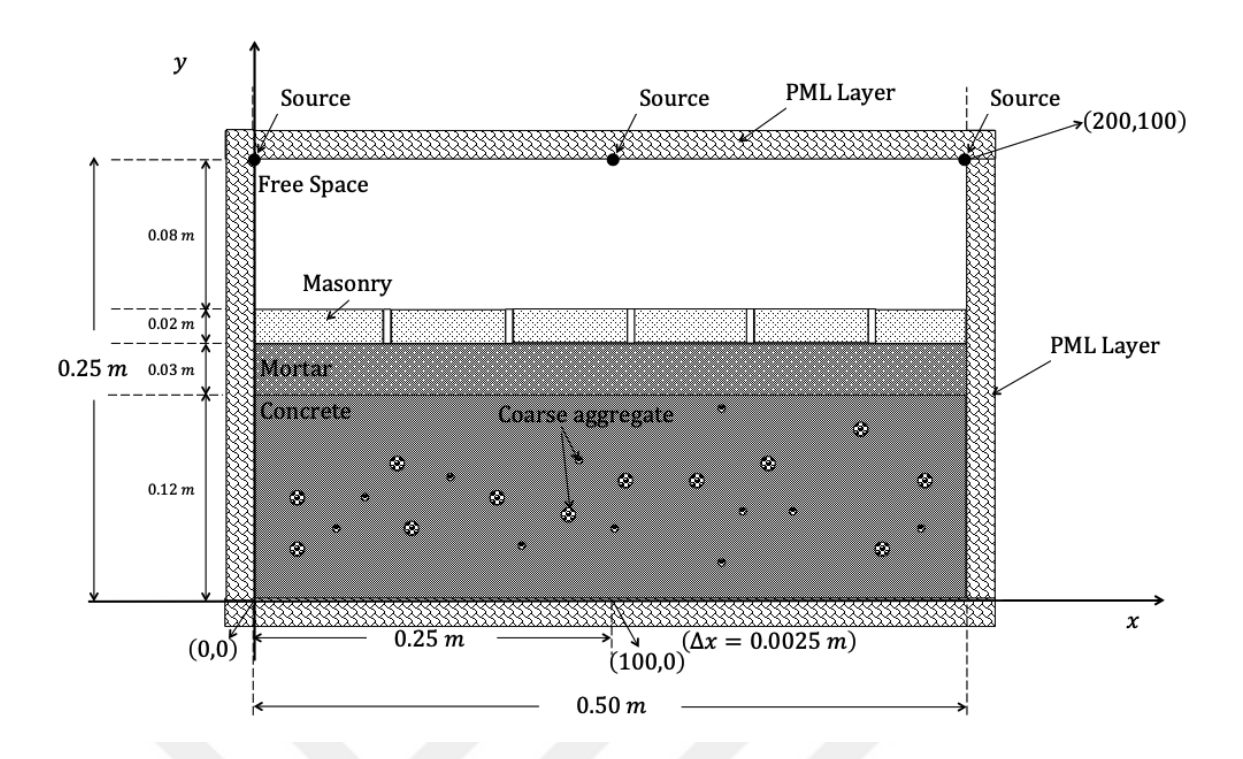
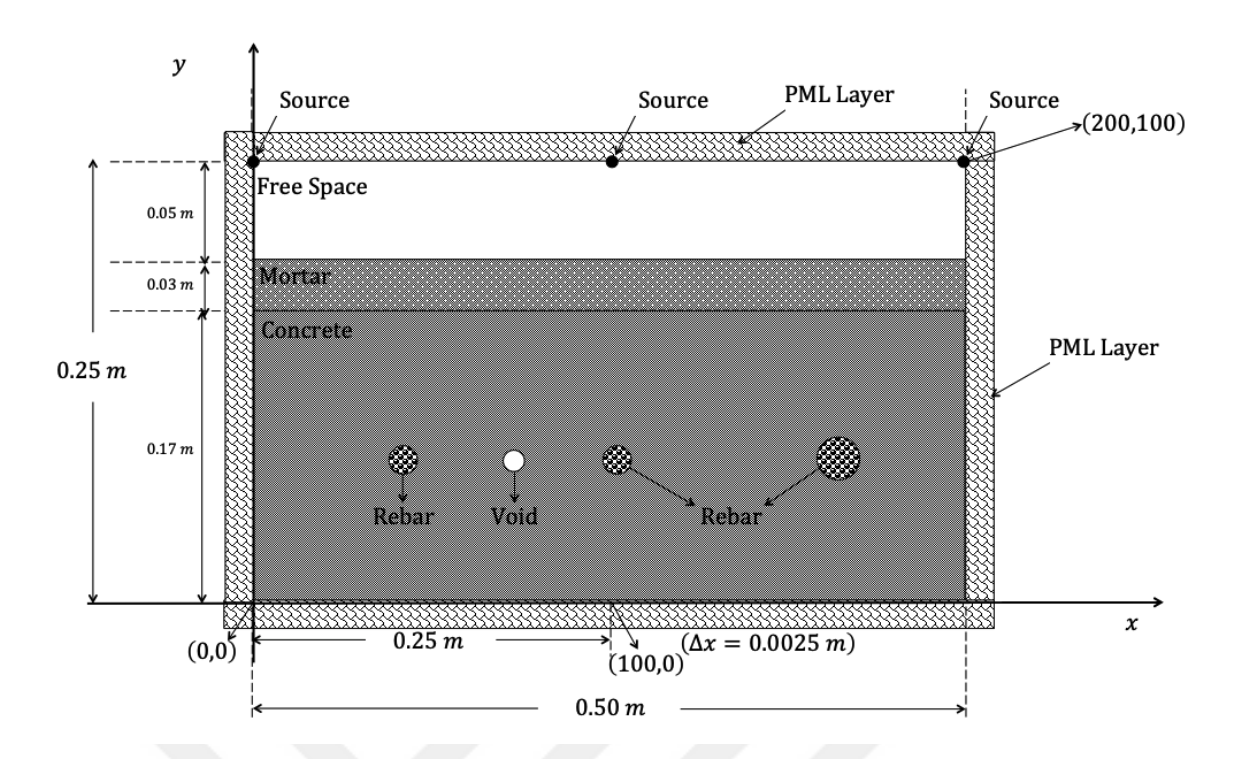


Figure 4.14 Model E: Layered Media with Concrete, Mortar and Masonry [118]

In Figure 4.14 a three-layered rectangular computational domain is presented. The calculation domain includes masonry, mortar and concrete which contains coarse aggregate respectively from top to bottom. There are air gaps between the masonries. This model has 0.5 m in the *x*-axis and 0.25 m in the *y*-axis. The computational domain is a rectangular region of  $0.5m \times 0.25m$ . The numerical domain is obtained by dividing into 200 grids in the *x*-axis and 100 grids in the *y*-axis,  $\Delta x = \Delta y = 0.0025m$ 



**Figure 4.15** Model F: Layered Media with Concrete, Mortar, Rebar and Void [118]

In the Model F experiment given in Figure 4.15 two-layered rectangular specimen that contain mortar and concrete layer is investigated. This sample includes a void and three rebar, two of which are of the same radius and the other one is thicker. This model has 0.5 m in the *x*-axis and 0.25 m in the *y*-axis. The computational domain is a rectangular region of  $0.5m \times 0.25m$ . The numerical domain is obtained by dividing into 200 grids in the *x*-axis and 100 grids in the *y*-axis,  $\Delta x = \Delta y = 0.0025m$ . The thicknesses of the concrete layer and mortar layer are 0.17 m and 0.03 m respectively. The height of the free space on the *y*-axis is 0.05 m.

#### 4.3.3 Simulation Results of Layered Media Samples

Simulation results for Model A for 500-time step at 1.5 GHz, 3.0 GHz and 6.0 GHz frequencies are given in Figure 4.16.

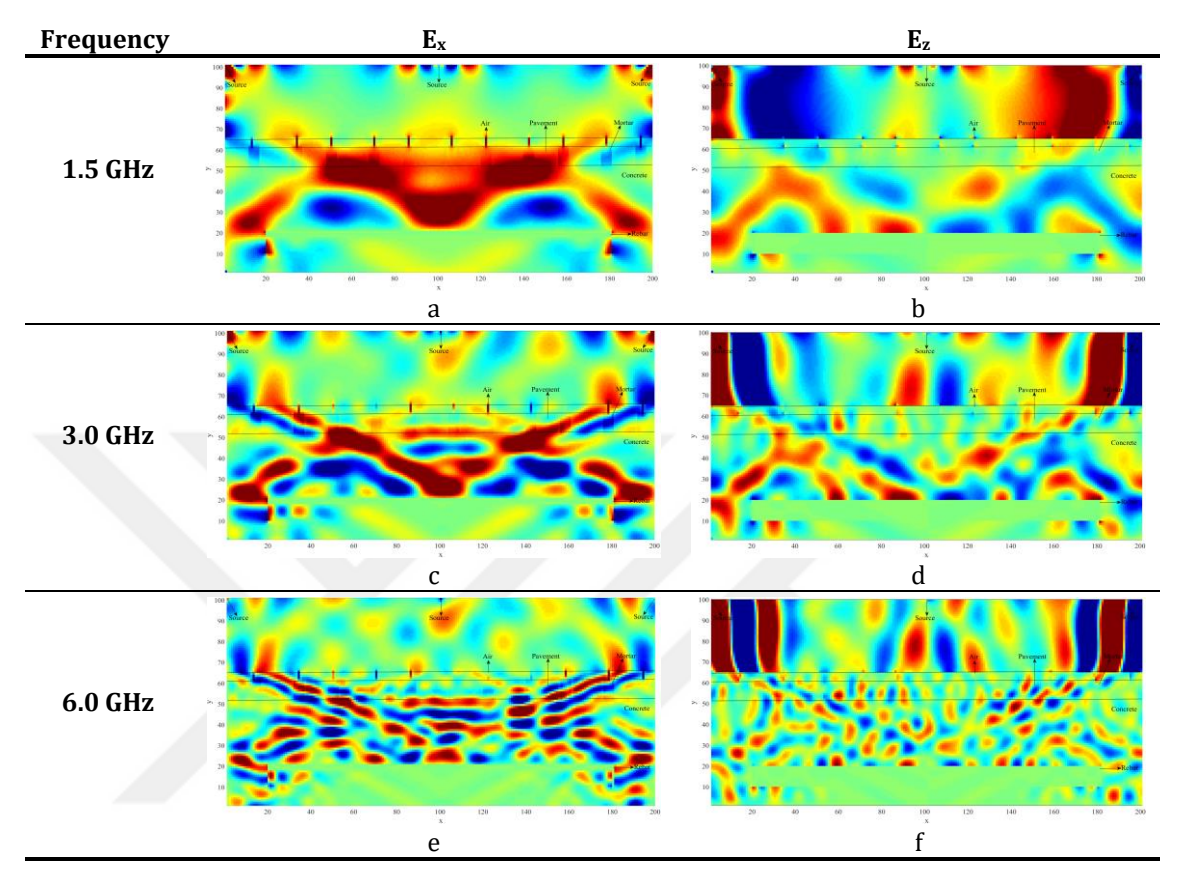


**Figure 4.16** Simulation Result for Model A at 500-Time Step: (a) E<sub>x</sub> Field Distribution for 1.5 GHz, (b) E<sub>z</sub> Field Distribution for 1.5 GHz, (c) E<sub>x</sub> Field Distribution for 3.0 GHz, (d) E<sub>z</sub> Field Distribution for 3.0 GHz, (e) E<sub>x</sub> Field Distribution for 6.0 GHz, (f) E<sub>z</sub> Field Distribution for 6.0 GHz [117]

Although the rebars can be displayed in all results, the best viewing for air gap between the pavement is obtained in Figure 4.16a. The transmission of the EM wave from one medium to another can be observed better in the field distribution obtained from TM mode. In Figure 4.16b Although the air gap between the pavement is not clearly visible, the transition from the air environment to the pavement and the encountering of the electromagnetic wave with the horizontal rebar are very evident. In Figures 4.16c and 4.16e, although the air gaps between the pavements are not as much as in the Figure 4.16a, they can be seen in Figures 4.16c and 4.16e. It is clear from the figures in the second column that the TM mode is suitable for different layer detection. In figures 4.16d and 4.16f the transition of the TM wave is

clearly observed in all the simulated frequencies. In this instance, lower frequencies are more convenient for material characterization and higher frequencies are suitable for rebar detection.

Simulation results for Model B for 400-time step at 1.5 GHz, 3.0 GHz and 6.0 GHz frequencies are given in Figure 4.17.

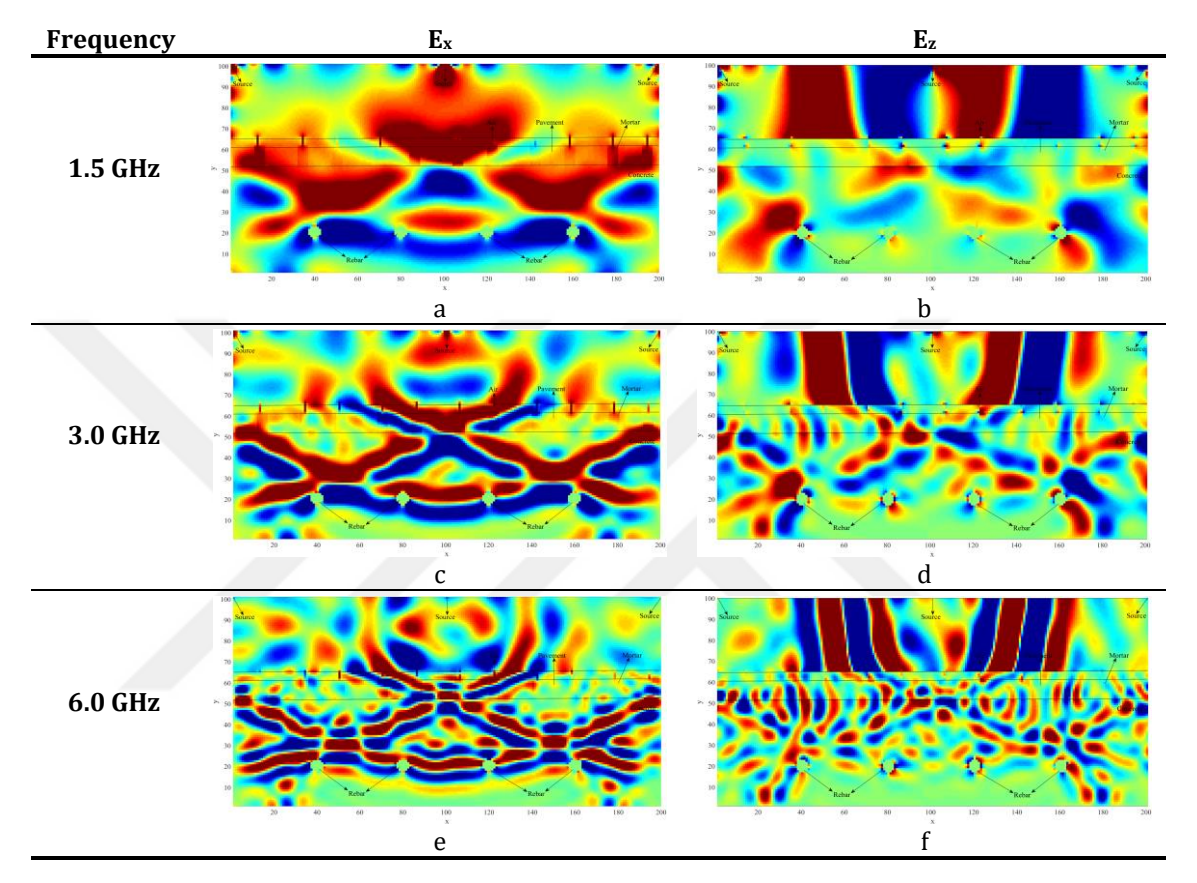


**Figure 4.17** Simulation Result for Model B at 400-Time Step: (a) E<sub>x</sub> Field Distribution for 1.5 GHz, (b) E<sub>z</sub> Field Distribution for 1.5 GHz, (c) E<sub>x</sub> Field Distribution for 3.0 GHz, (d) E<sub>z</sub> Field Distribution for 3.0 GHz, (e) E<sub>x</sub> Field Distribution for 6.0 GHz, (f) E<sub>z</sub> Field Distribution for 6.0 GHz [117]

In Figure 4.17 the electromagnetic wave provides less interaction with the rebar in terms of the cross-sectional area less time steps needed. The rebars can be displayed in all results, the best viewing for air gap between the pavement is obtained in Figure 4.17a. The transmission of the EM wave from one medium to another can be observed better in the field distribution obtained from TM mode as can be seen in figures obtained for Model A. In Figure 4.17b, the air gap between the pavement is not clearly visible, the transition from the air environment to the pavement and the encountering of the electromagnetic wave with the horizontal rebar are very

evident. In Figures 4.17c and 4.17e, although the air gaps between the pavements are not as much as in the Figure 4.17a, they can be seen in Figures 4.17c and 4.17e. It is clear from the figures in the second column that the TM mode is suitable for different layer detection. In figures 4.17d and 4.17f the transition of the TM wave is clearly observed in all the simulated frequencies. In this instance, lower frequencies are more convenient for material characterization and higher frequencies are suitable for rebar detection.

Simulation results for Model C for 250-time step at 1.5 GHz, 3.0 GHz and 6.0 GHz frequencies are given in Figure 4.18.

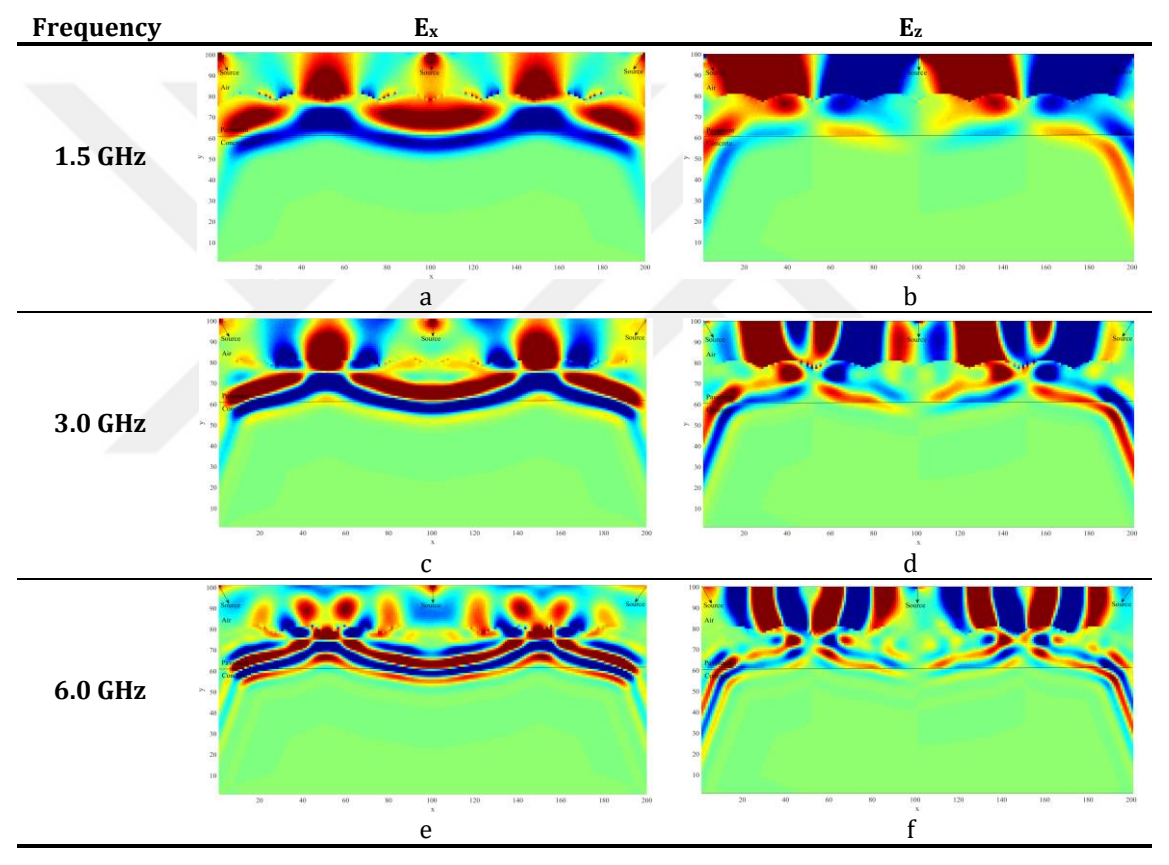


**Figure 4.18** Simulation Result for Model C at 250-Time Step: (a) E<sub>x</sub> Field Distribution for 1.5 GHz, (b) E<sub>z</sub> Field Distribution for 1.5 GHz, (c) E<sub>x</sub> Field Distribution for 3.0 GHz, (d) E<sub>z</sub> Field Distribution for 3.0 GHz, (e) E<sub>x</sub> Field Distribution for 6.0 GHz, (f) E<sub>z</sub> Field Distribution for 6.0 GHz [117]

In Figure 4.18a, 4.18c and 4.18e  $E_x$  field distributions at 250-time steps are obtained at 1.5 GHz, 3.0 GHz and 6.0 GHz respectively.  $E_z$  field distributions at 1.5 GHz, 3.0 GHz and 6.0 GHz for 250 time steps are given in 4.18b, 4.18d and 4.18f respectively. In this physical model, there is no further layer and rebar under the concrete, so no

more time steps are needed. Since lower frequencies are more suitable for material characterization Figure 4.18a and 4.18b are the best results for this physical model. Simulation results for Model D for 400-time step at 1.5 GHz, 3.0 GHz and 6.0 GHz frequencies are given in Figure 4.19.

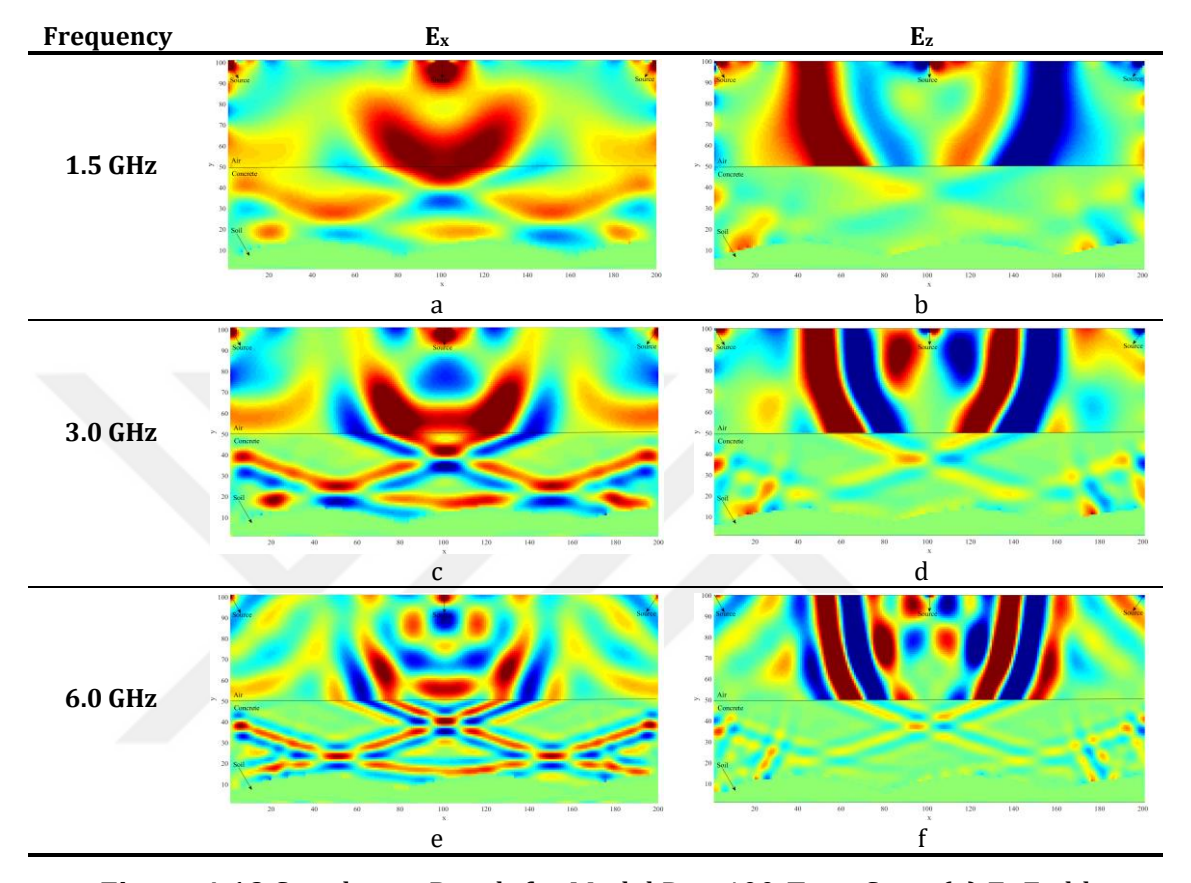


**Figure 4.19** Simulation Result for Model D at 400-Time Step: (a)  $E_x$  Field Distribution for 1.5 GHz, (b)  $E_z$  Field Distribution for 1.5 GHz, (c)  $E_x$  Field Distribution for 3.0 GHz, (d)  $E_z$  Field Distribution for 3.0 GHz, (e)  $E_x$  Field Distribution for 6.0 GHz, (f)  $E_z$  Field Distribution for 6.0 GHz [117]

In Figure 4.19a, 4.19c and 4.19e  $E_x$  field distributions at 400-time steps are obtained at 1.5 GHz, 3.0 GHz and 6.0 GHz respectively.  $E_z$  field distributions at 1.5 GHz, 3.0 GHz and 6.0 GHz for 250 time steps are given in 4.18b, 4.18d and 4.18f respectively. Since the layered part examined by sending electromagnetic wave is thinner than other physical models, the time step is shorter. In this model, a structure consisting of two different materials is examined. In this model, more time steps are required than the Model C because the material to be simulated is deeper. As a result, in Figure 4.19a and 4.19b the soil layer is clearer.

Simulation results for Model E for 450-time step at 1.5 GHz, 3.0 GHz and 6.0 GHz frequencies are given in Figure 4.20.

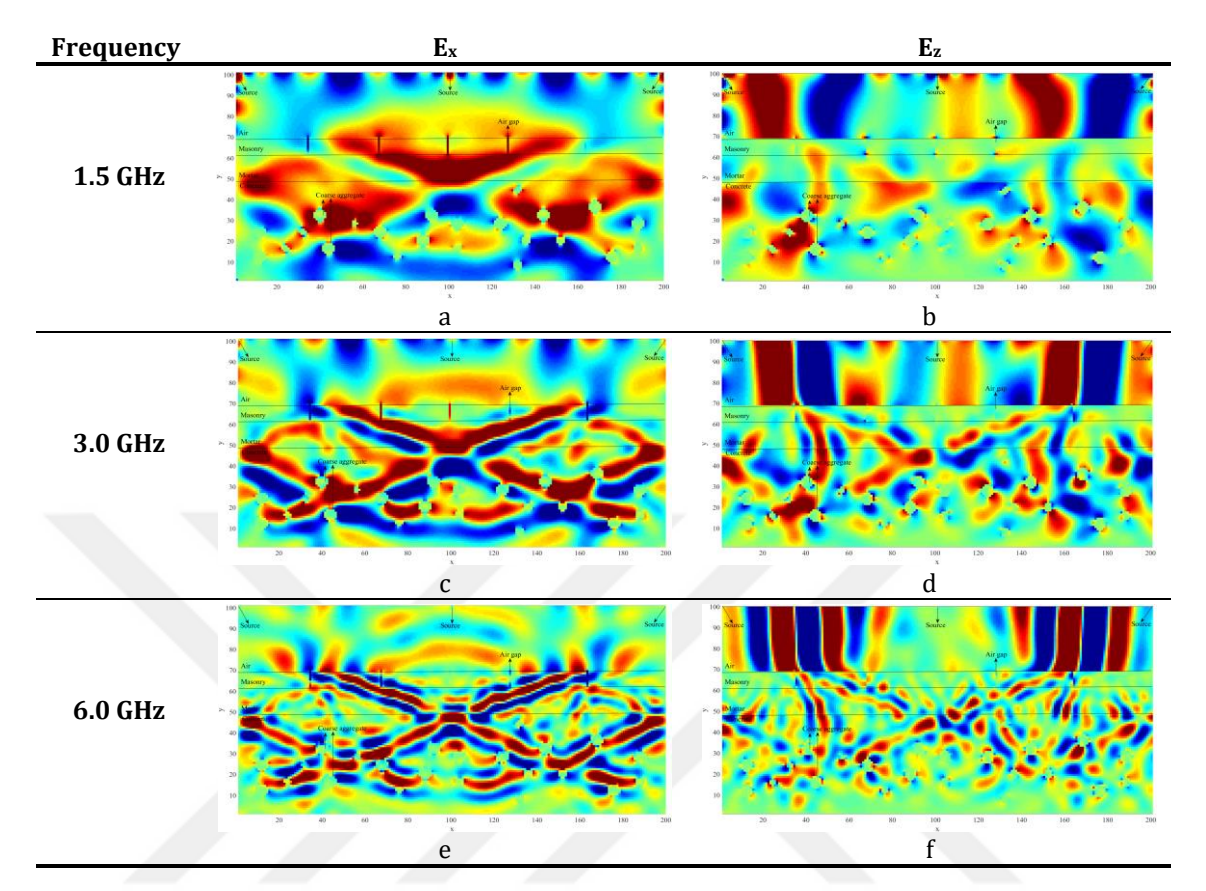


**Figure 4.20** Simulation Result for Model E at 450-Time Step: (a) E<sub>x</sub> Field Distribution for 1.5 GHz, (b) E<sub>z</sub> Field Distribution for 1.5 GHz, (c) E<sub>x</sub> Field Distribution for 3.0 GHz, (d) E<sub>z</sub> Field Distribution for 3.0 sGHz, (e) E<sub>x</sub> Field Distribution for 6.0 GHz, (f) E<sub>z</sub> Field Distribution for 6.0 GHz [118]

In Figure 4.20a, 4.20c and 4.20e  $E_x$  field distributions at 1.5 GHz, 3.0 GHz and 6.0 GHz frequencies for 450-time steps for Model F are given respectively. In Figures 4.20b, 4.20d and 4.20f the  $E_z$  electric field distribution of the TM mode at 1.5 GHz, 3.0 GHz and 6.0 GHz frequencies at 450-time steps are given. While the gaps between the masonries can be seen more clearly in the figures obtained from the TE mode, the separation of the layers can be better visualized in the TM mode. In Figure 4.20c even though the coarse aggregates are visible, the layers are almost indistinguishable so 1.5 GHz frequency is more suitable for material characterization than 3.0 GHz and in Figure 4.20e everything is seen seamlessly. In Figure 4.21e layers are no longer fully distinguishable but aggregates are slightly visible.

Simulation results for Model F for 450-time step at 1.5 GHz, 3.0 GHz and 6.0 GHz frequencies are given in Figure 4.21.

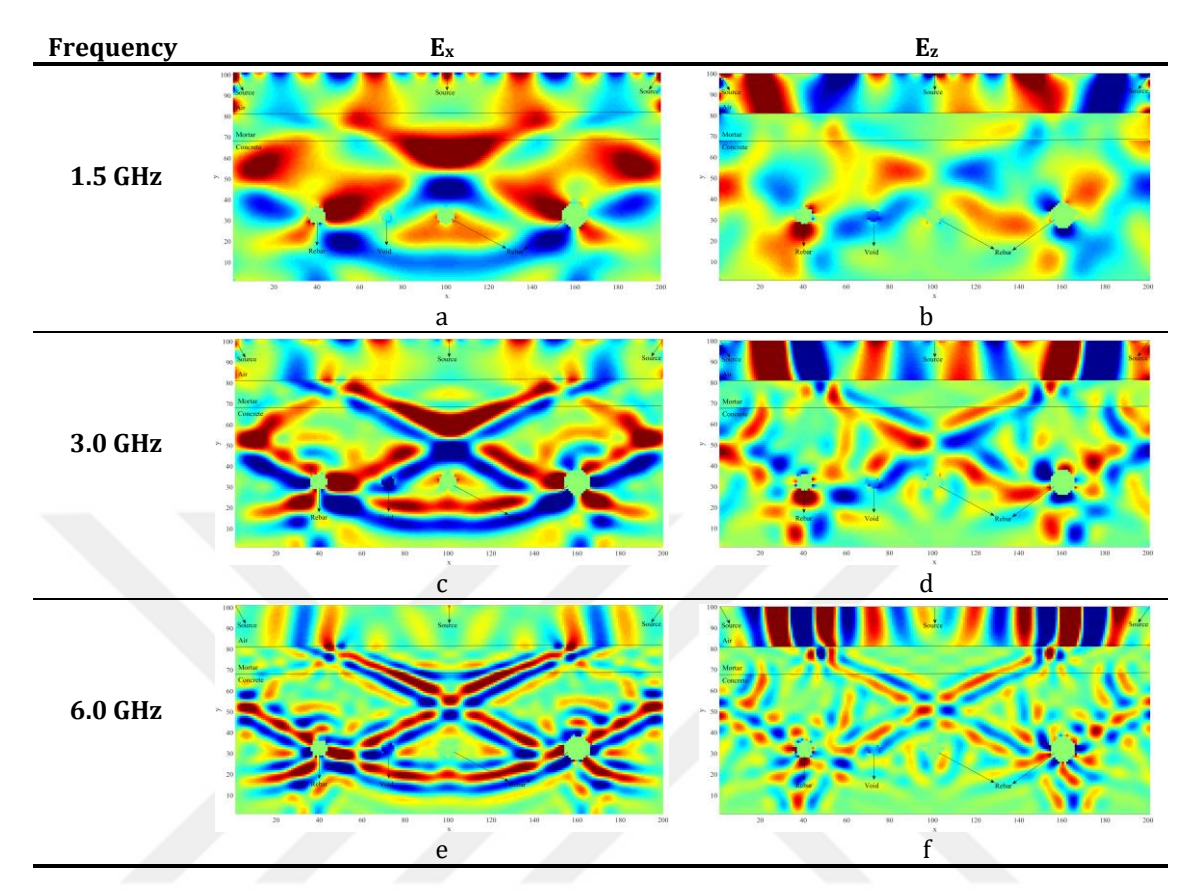


**Figure 4.21** Simulation Result for Model F at 450-Time Step: (a) E<sub>x</sub> Field Distribution for 1.5 GHz, (b) E<sub>z</sub> Field Distribution for 1.5 GHz, (c) E<sub>x</sub> Field Distribution for 3.0 GHz, (d) E<sub>z</sub> Field Distribution for 3.0 GHz, (e) E<sub>x</sub> Field Distribution for 6.0 GHz, (f) E<sub>z</sub> Field Distribution for 6.0 GHz [118]

In Figure 4.21a, 4.21c and 4.21e  $E_x$  field distributions at 1.5 GHz, 3.0 GHz and 6.0 GHz frequencies for 450-time steps for Model F are given respectively. In Figures 4.21b, 4.21d and 4.21f the  $E_z$  electric field distribution of the TM mode at 1.5 GHz, 3.0 GHz and 6.0 GHz frequencies at 450-time steps are given.

In Figure 4.21c the mortar layer is completely blurred but the rebars remains clearly visible and thickness differences between them can be observed in all results. At all frequencies that numerical models are simulated the rebar can be clearly but higher frequency namely at 6.0 GHz rebar is clearer.

The layered media may be encountered in bridge, road or different structures are designed as a numerical simulation experiment. The capability of the FDTD method

for simulation of layered media containing pavement, mortar concrete rebar and even soil is investigated. The layers of the rectangular structure with pavement, concrete and the rebar inside it are successfully viewed. In the physical models that contain rebar, the rebar can be displayed better at higher frequency in a word at 6.0 GHz. Also, different pavement and concrete surfaces are observed in such a way that the thickness of the layers is noticeable, and the best simulation results is obtained at 1.5 GHz and 3.0 GHz frequencies for microwave radar NDT technique.

## 4.4 Cylindrical Concrete Types

FRP composites are widely used for the improvement and strengthening of structures due to their lightness and robustness [122, 123]. Structural reinforcement using FRP composites is investigated for two different conditions. Structural reinforcement can be done by covering FRP composites outside of the concrete pile containing defects (delamination, void, crack) and FRP tubes. Although these composite structures are more robust to corrosion and biological threats than conventional piles, delamination or other defects in the concrete may occur. Materials that have different dielectric properties can be specified via radar NDT. The response of the concrete filled FRP tube including rebar and FRP wrapped concrete structure containing void and delamination is investigated by numerical methods [124, 125].

#### 4.4.1 Definition of Cylindrical Concrete Types with Defects

Covering the bored piles with plastic or using fiber-reinforced polymer piles is an important solution method in order to make the bored piles resistant to moisture, such as the seaside or river sides, which are extremely exposed to water and moisture. Composite pile research continues using many different types of materials. Composite piles are highly preferred in load bearing or fender application. FRP piles filled with concrete, reinforced plastic matrix piles, glass fiber reinforced plastic piles and glass fiber pultrude piles are the most commonly used composite piles. The preferred reasons for these piles are to be high weight resistant, suitable for deep foundations and resistance to environmental threats. The most commonly used composite pile is obtained by filling the fiber reinforced polymer heap of FRP with concrete. The glass fibers are used as the main reinforcement fiber in many FRP

shells is that they are light weight, low cost and heat resistant. FRP composites have higher tensile strength than steel, it is a structural advantage. The fiber reinforced shell is resistant to tensile, the concrete core is resistant to compressive. In this subsection, three different cylindrical concrete structures are examined, and simulation results are obtained [126].

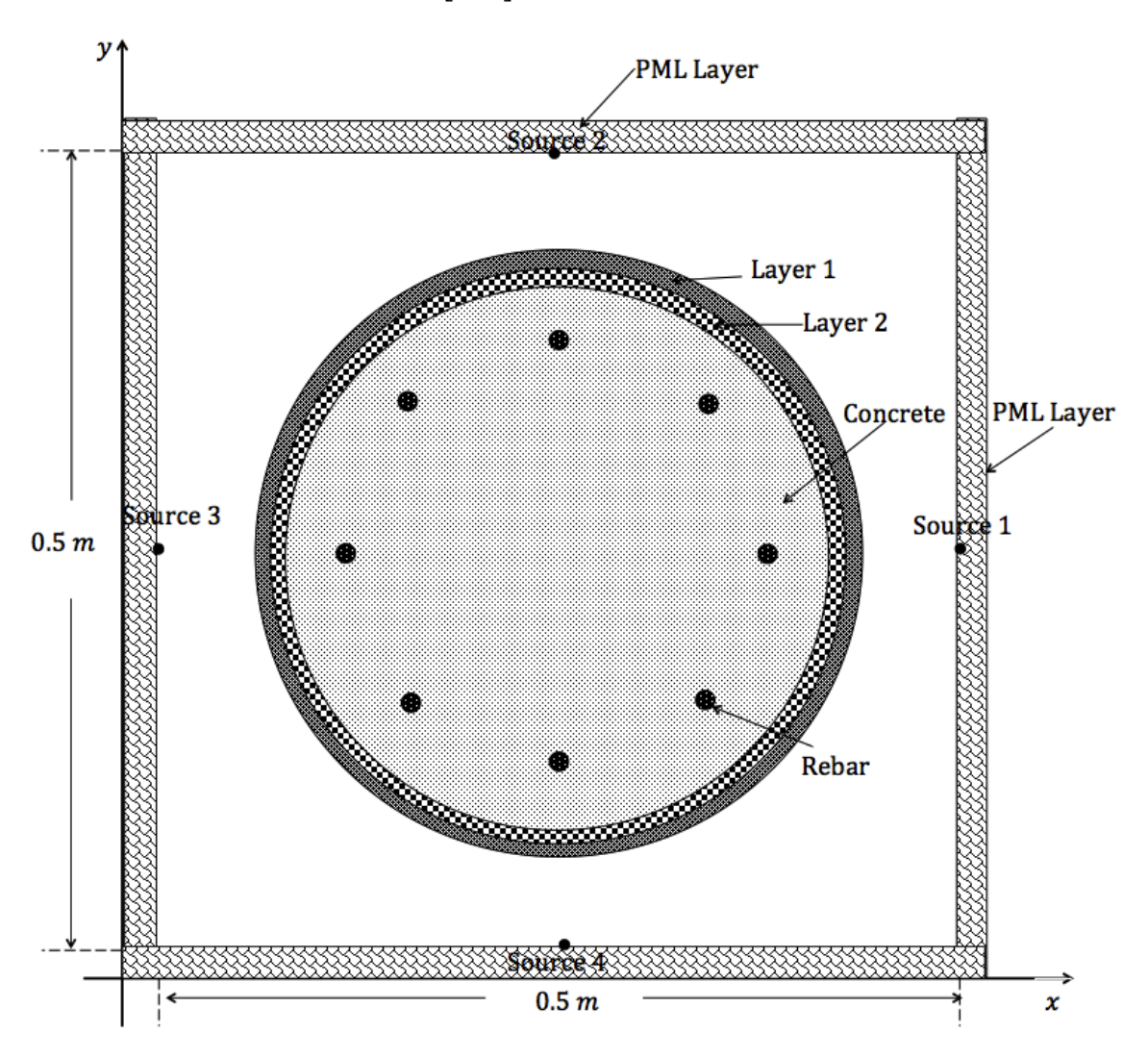


**Figure 4.22** Cylinder A: Two-Layered FRP Tube with Concrete Core and Rebar [126]

The two-dimensional geometry is divided into cells of much smaller size than the wavelength. The computational domain is a quadratic region of  $0.5m \times 0.5m$ . The numerical domain is obtained by dividing into 200 grids both the x-axis and the y-axis,  $\Delta x = \Delta y = 0.0025m$  and  $\Delta x = \Delta y \cong \lambda/120$ . In the first numerical experiment, a three-layered cylinder with eight embedded rebar is used to test the method. The

thickness of the FRP epoxy layer and epoxy layer is 0.025 m and the diameter of inner concrete cylinder is 0.35 m.

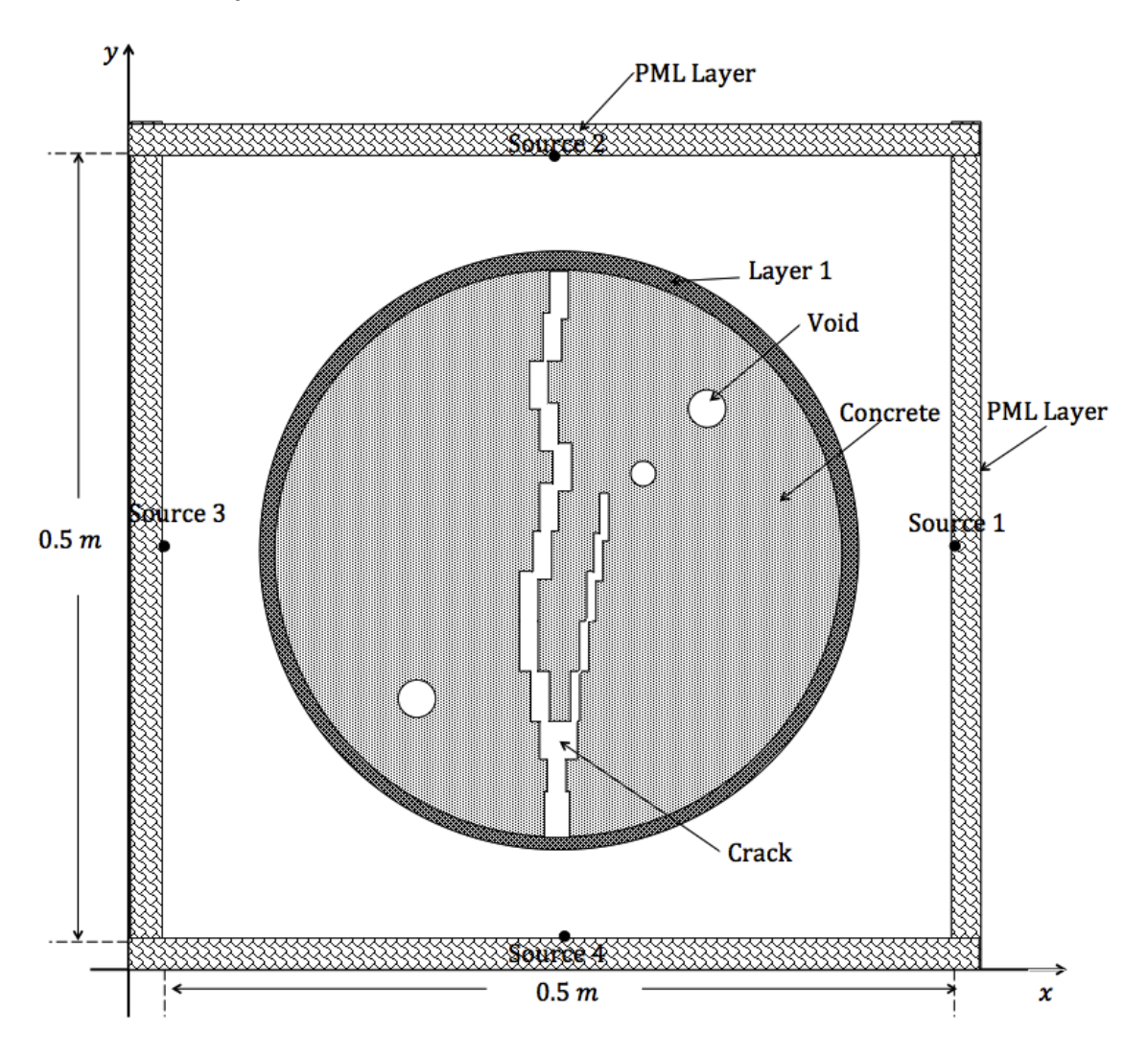


**Figure 4.23** Cylinder B: One-Layered FRP Tube with Concrete Core and Crack [126]

In experiment given in Figure 4.23 one-layered concrete cylinder is investigated. The thickness of the FRP epoxy layer that used to strengthen the concrete is 0.025 m and diameter of the concrete column is 0.4 m. A branching crack is identified in the middle of the concrete core, and the part advancing to the right is defined more thinly than the crack in the middle. The purpose of defining the size of the crack differently is to investigate whether it is possible to detect the thinness and thickness, that is, the size difference, in simulation. In addition to the crack, three voids are identified. Two of these voids are the same size, but one is smaller. Here too, it is aimed to observe the size difference between the voids.

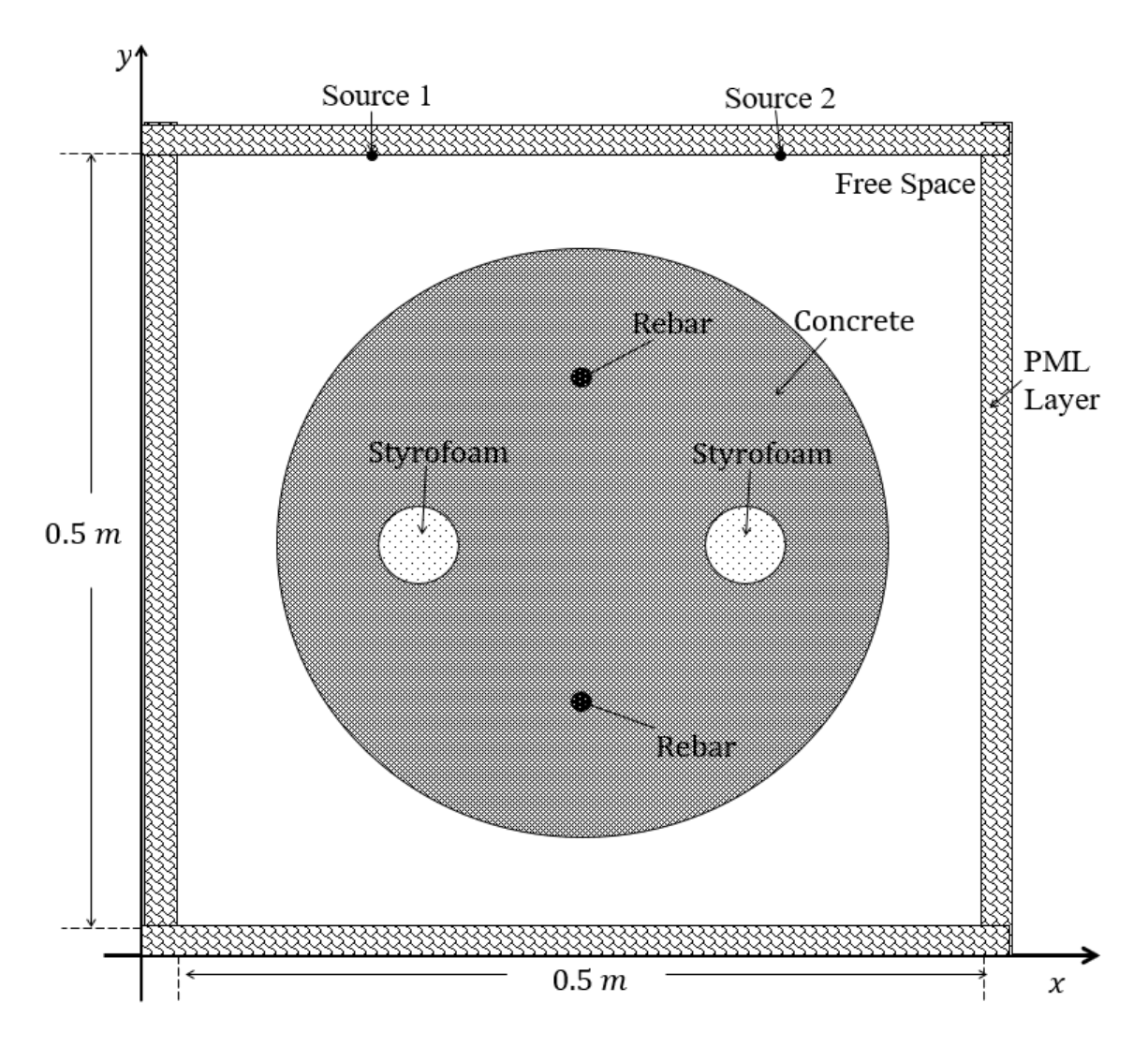
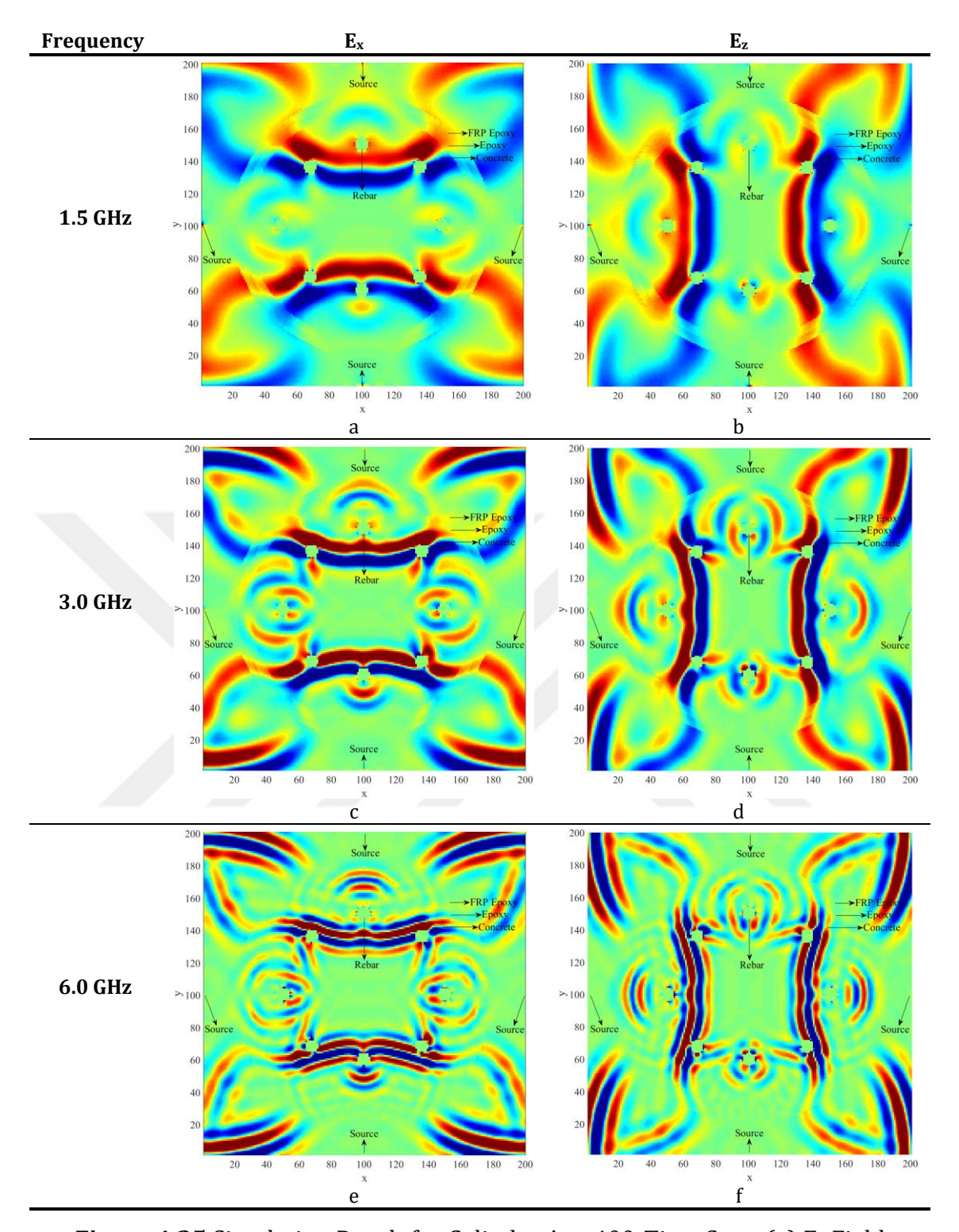


Figure 4.24 Cylinder C: Concrete Cylinder with Styrfoam and Rebar

In the cylinder C, only concrete cylinder is examined, and it does not contain FRP shell. The numerical domain is divided into 200 grids both the *x*-axis and the *y*-axis,  $\Delta x = \Delta y = 0.0025 \, m$ . The concrete cylinder contains two rebars and two styrofoam balls. Since the dielectric constant of the styrofoam is very close to the dielectric constant of the air, a styrofoam ball is used to express the void in the concrete structure.

### 4.4.2 Simulation Results of Cylindrical Concretes

Simulation results for Cylinder A for 400-time step at 1.5 GHz, 3.0 GHz and 6.0 GHz frequencies are given in Figure 4.25.



**Figure 4.25** Simulation Result for Cylinder A at 400-Time Step: (a)  $E_x$  Field Distribution for 1.5 GHz, (b)  $E_z$  Field Distribution for 1.5 GHz, (c)  $E_x$  Field Distribution for 3.0 GHz, (d)  $E_z$  Field Distribution for 3.0 GHz, (e)  $E_x$  Field Distribution for 6.0 GHz, (f)  $E_z$  Field Distribution for 6.0 GHz [126]

Although the results obtained from the TE and TM modes differ in rectangular models and the TM mode gives better results in material characterization, there is no significant difference between the results in the cylindrical models. In Figure 4.25a, 4.25c and 4.25e  $E_x$  field distributions at 1.5 GHz, 3.0 GHz and 6.0 GHz frequencies for 400-time steps for Cylinder C are given respectively. In Figure 4.25b, 4.25d and 4.25f  $E_z$  field distributions at 1.5 GHz, 3.0 GHz and 6.0 GHz frequencies for 400-time steps for Cylinder A are given respectively. In Figure 4.25a and 4.25b the layers of FRP tube and rebars can be seen clearly, the layers are best determined at 1.5 GHz frequency. At 3.0 GHz, the distinction between layers becomes indistinct, and at 6.0 GHz, the layers cannot be determined at all. For the observation of the rebars, the frequency does not matter, but at 6.0 GHz the layers are not visible, so the rebars come to the fore.

Simulation results for Cylinder B for 400-time step at 1.5 GHz, 3.0 GHz and 6.0 GHz frequencies are given in Figure 4.26, 4.27.

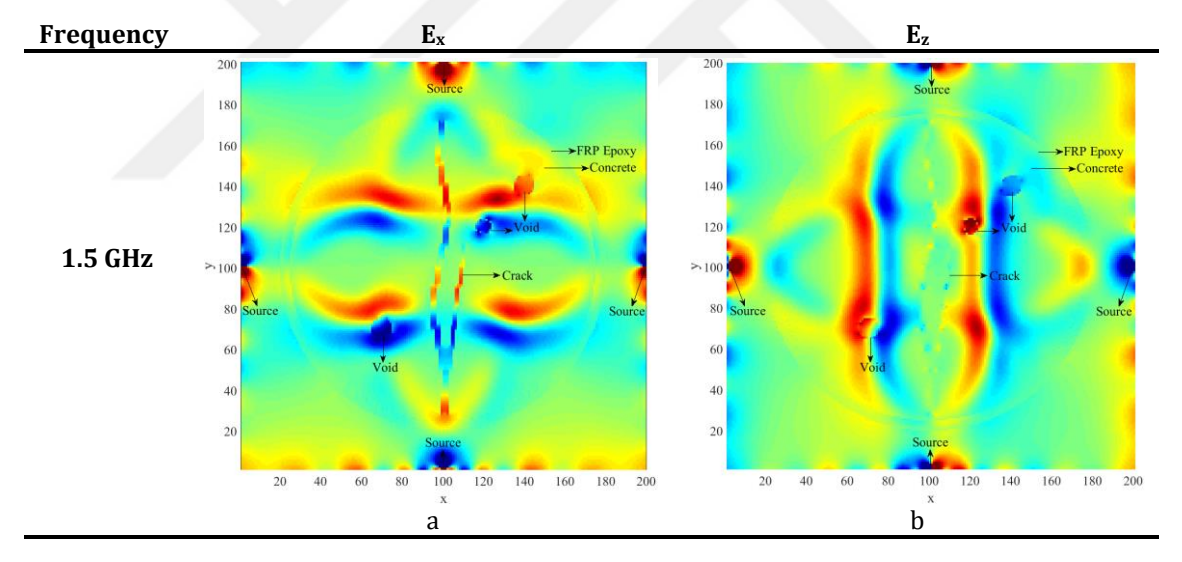


**Figure 4.26** Simulation Result for Cylinder B at 400-Time Step: (a)  $E_x$  Field Distribution for 1.5 GHz, (b)  $E_z$  Field Distribution for 1.5 GHz [126]

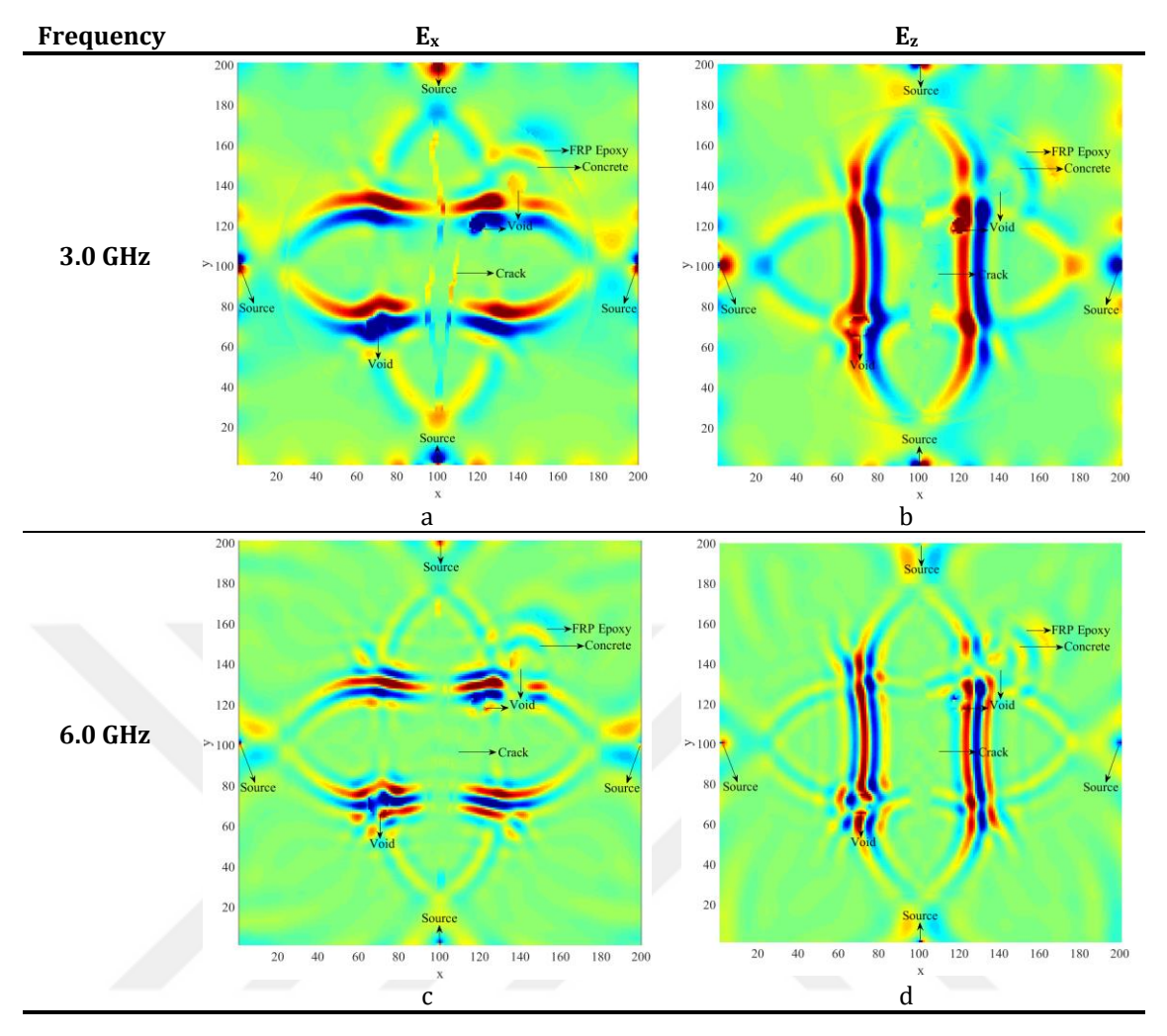


**Figure 4.27** Simulation Result for Cylinder B at 400-Time Step: (a) E<sub>x</sub> Field Distribution for 3.0 GHz, (b) E<sub>z</sub> Field Distribution for 3.0 GHz, (c) E<sub>x</sub> Field Distribution for 6.0 GHz, (d) E<sub>z</sub> Field Distribution for 6.0 GHz [126]

In Figure 4.26a, 4.27a and 4.27c  $E_x$  field distributions at 1.5 GHz, 3.0 GHz and 6.0 GHz frequencies for 400-time steps for Cylinder B are given respectively. In Figure 4.26b, 4.27b and 4.27d  $E_z$  field distributions at 1.5 GHz, 3.0 GHz and 6.0 GHz frequencies for 400-time steps for Cylinder B are given respectively. In the Cylinder B the crack inside the composite pile is like delamination and the right part of the crack is thinner than the left part. In the case of Cylinder, A, no significant difference is observed between the results obtained from the TE and TM mode, but differences emerge here. In Figure 4.26a both crack and voids can be seen clearly. In Figure 4.26b while the crack is not clearly visible, the voids can be seen. When the results at 3.0 GHz frequency are compared, both fracture and gap can be detected in TE mode, while no fracture is detected in TM mode.

Simulation results for Cylinder C for 400-time step at 1.5 GHz, 3.0 GHz and 6.0 GHz frequencies are given in Figure 4.28.

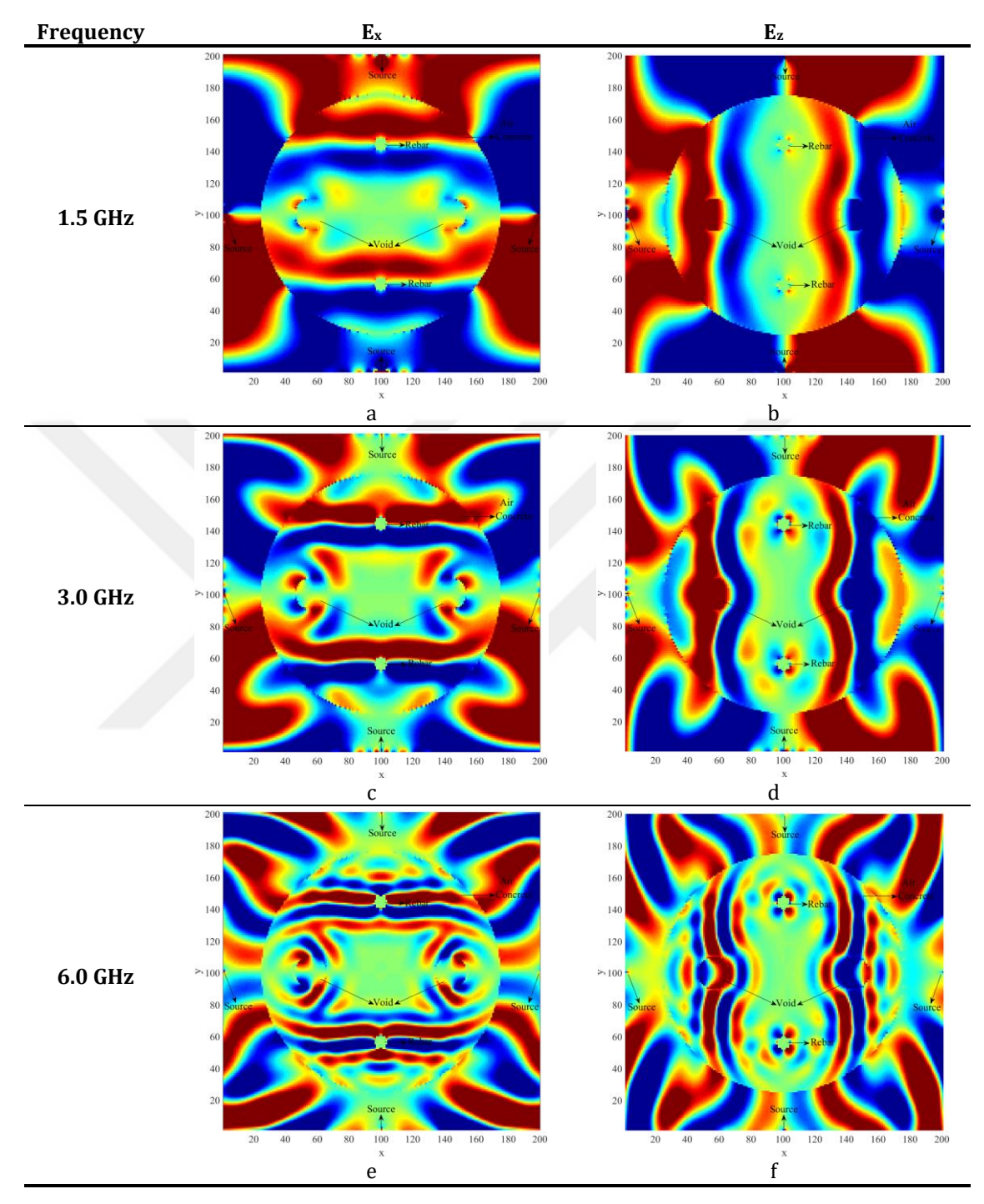


**Figure 4.28** Simulation Result for Cylinder C at 400-Time Step: (a)  $E_x$  Field Distribution for 1.5 GHz, (b)  $E_z$  Field Distribution for 1.5 GHz, (c)  $E_x$  Field Distribution for 3.0 GHz, (d)  $E_z$  Field Distribution for 3.0 GHz, (e)  $E_x$  Field Distribution for 6.0 GHz

In Figure 4.28a, 4.28c and 4.28e  $E_x$  field distributions at 1.5 GHz, 3.0 GHz and 6.0 GHz frequencies for 400-time steps for Cylinder C are given respectively. In Figure 4.28b, 4.28d and 4.28f  $E_z$  field distributions at 1.5 GHz, 3.0 GHz and 6.0 GHz frequencies for 400-time steps for Cylinder C are given respectively. Since there is no FRP shell in the simulation setup here and the electromagnetic wave interacts directly with the concrete, iron and foam can be displayed in almost all the results. The optimal frequency for void imaging is 1.5 GHz, while rebar detection is almost frequency independent.

# CONCRETE STRUCTURE SPECIMENS AND MEASUREMENTS

Concrete samples are heterogeneous material containing fine aggregate, coarse aggregate, sand, cement, water and a certain amount of chemicals in it. Concretes are divided into three main groups according to their unit weights. Those weighing approximately 2400 kg/m³ are called normal concrete and are the most commonly used concrete type for carrier purposes. Lightweight concretes are those with a unit weight of less than 2400 kg/m³. Concrete with a unit weight of more than 2600 kg/m³ is called heavy concrete [127].

Ground Penetrating Radar (GPR), a remote sensing technology, is an important method used to view underground, concrete blocks and asphalt floors. In the GPR system, electromagnetic waves are sent to the ground, and the signals reflected from the soil are collected and processed, so that the underground or inside the sample is displayed. In this way, information such as depth, shape, size and water density of the target object is obtained. Targets can be classified as a long, thin, spherical or cylindrical object or a planar soil layer according to their electrical and geometric structure. System performance depends on basic antenna and radar parameters such as frequency band, transmitter power, antenna gain, dynamic range calculated by taking into account the electrical loss of the environment (soil, asphalt, concrete, etc.) and the scattering characteristics of the buried object. The capabilities of the software and hardware units determine the performance of the whole system. GPR technology is used in many research areas such as researching the infrastructure of cities, researching tunnels, mining surveys, detecting underground pipes and cables, asphalt control surveys, archaeological research, and military field research [119]. The features of GPR systems differ according to the features of the applications in which they are used. The GPR method is also used in underground mapping studies, finding the anomaly mass underground, mapping the karst areas, finding metallic or

non-metallic structures (gas pipes, waste pipes, telephone cables, etc.), mapping the underground mine areas, determining the changes of lateral discontinuities, determining the bedrock depth. It is used for mapping river and lake floors, investigating and mapping landslide planes [121]. Since this method does not cause any damage, it is also used in bridge and tunnel research. For this reason, it is used in the examination of new tunnels and bridges, in deciding the suitability of the ground on which the structures will be built, in determining the final state of the structure in renovation works, and in researching columns and connection places. In addition, it is used in tunnel surveys, determination of parking and garage areas, foundation thickness determination studies, determination of the places behind concrete or walls and measuring concrete thicknesses [119].

# **5.1** Molding the Concrete Samples

Four of the concrete models simulated in Chapter 4 are created and measured at microwave frequencies, and the results are expressed in this section. It is determined that the produced concretes gained most of their compressive strength when they were 28 days old. Concrete is a material that gains strength over time. The strength gain, which is very fast in the first 7 days, continues slowly. Concrete reaches approximately 70% of its strength at 28 days of age, which is generally predicted in 7 days. For this reason, the 28-day strength of the concrete significantly affects the humidity and temperature of the environment, especially in the first week. In all international and national regulations, the 28-day strength standard strength is accepted. The 28-day characteristic compressive strength of concrete used in reinforced concrete generally varies between 140 and 500 kgf./cm². The compressive strength of concrete is measured on 28-day-old cylindrical (15 cm diameter, 30 cm height) or cube (15 cm sided) specimens stored under standard curing conditions (in 20 °C ±2 °C lime-saturated water) [129]. Concrete strength and classes are shown in Table 5.1.

**Table 5.1** Concrete Types and Strengths

<b>Concrete Types</b>	f <sub>ck</sub> , cylinder (N/mm <sup>2</sup> )	f <sub>ck</sub> , cube(N/mm <sup>2</sup> )
BS 16 (C 16)	16	20
BS 18 (C 18)	18	22
BS 20 (C 20)	20	25
BS 25 (C 25)	25	30
BS 30 (C 30)	30	37
BS 35 (C 35)	35	45
BS 40 (C 40)	40	50
BS 45 (C 45)	45	55
BS 50 (C 50)	50	60

The general name of materials such as sand, gravel, crushed stone used in concrete production is aggregate. Approximately 60-70% of a concrete sample consists of aggregates and is an important component of concrete. In order to obtain a durable and economical concrete, the aggregates used in the mixture must have certain properties. Durable, workable and high quality concrete can be obtained by using suitable aggregates. The use of more sand and less coarse aggregate than conventional concrete also increases the ability to pass through the reinforcement, that is, it affects the fluidity of the concrete. However, decreasing the coarse aggregate ratio reduces the compressive strength. It is the best solution to use both crushed and natural aggregate together for the optimization of workability and compressive strength of concrete [129].

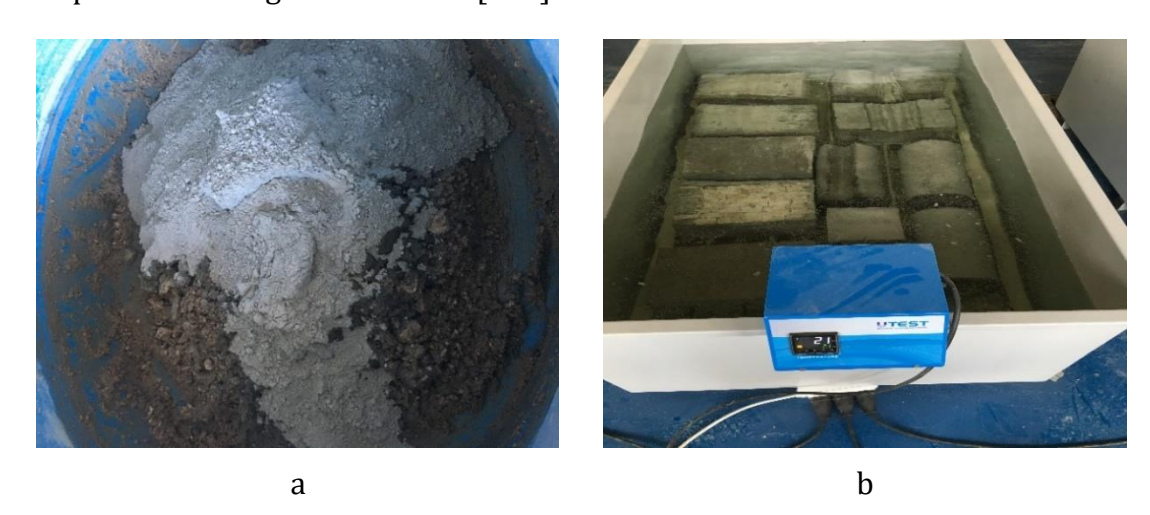


**Figure 5.1** Preparation of Concrete Samples: (a) Preparation of Concrete Mix, (b) Keeping the Samples in the Curing Tank

Another important component of concrete is cement. Generally, cement dosage is recommended to be between 350 kg/m³ and 450 kg/m³. Since the cement dosage of 500 kg/m³ or more will increase the drying shrinkage of the concrete, the risk of cracks and fractures in the concrete increases. Portland cement is used in the concrete samples prepared for the measurement in our study. A photograph of the preparation phase of the concrete used when creating the measured samples and a photograph of the concrete samples being kept in the curing tank for 28 days after preparation are given in Figure 5.1.



Figure 5.2 Physical Structure of Rectangular Models: (a) Case A, (b) Case B [114]

Concrete specimens are prepared in accordance with the simulation setup in given in Case A and Case B. In Figure 5.2a a defect is created on the concrete surface by using rectangles that narrow down in width but remain constant in height and Figure 5.2b, using successive circles a wider crack is created. Four rebars are used in both specimens. Instead of using standard molds while creating concrete samples, molds are created from styrofoam and samples are prepared in accordance with the dimensions given in the simulation setups. In order to obtain the cracks on the surface of the concrete samples, styrofoam cuts are made in accordance with the simulation measurements. The extruded form of the rectangular concrete samples, which were measured, is presented in Figure 5.2.

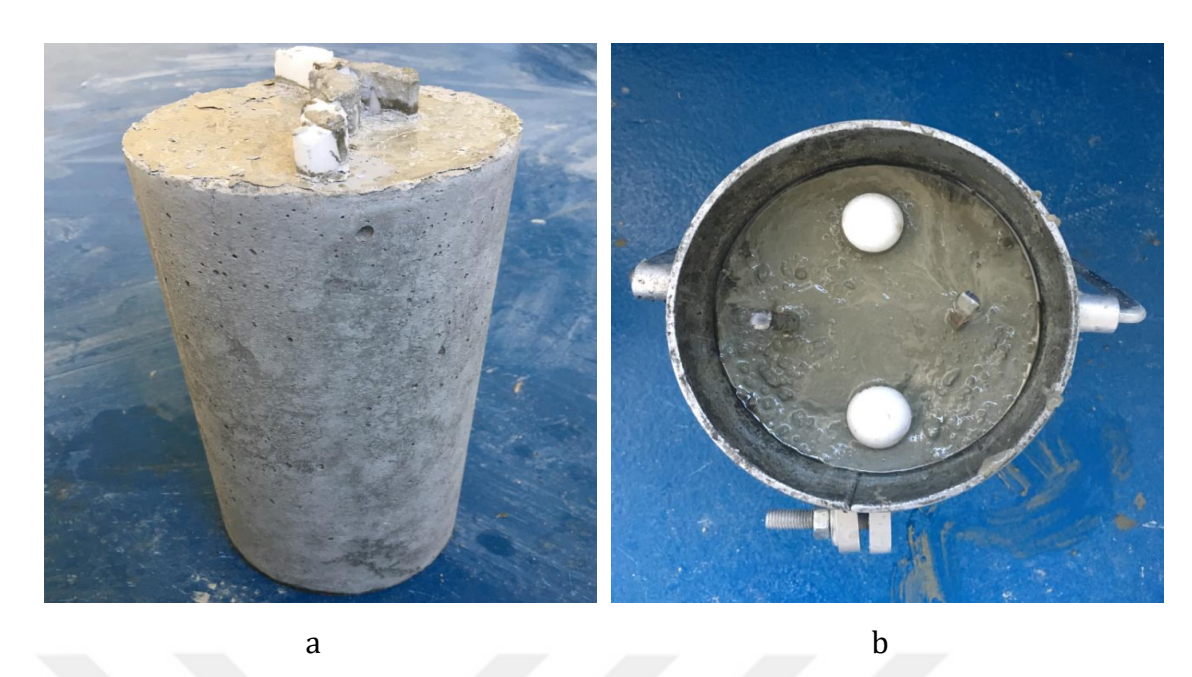


Figure 5.3 Physical Structure of Cylindrical Models: (a) Cylinder B, (b) Cylinder C

Two of the samples measured are selected from the cylindrical models. Cylindrical concrete samples are prepared in accordance with the simulation setup given in Cylinder B and Cylinder C. Cylindrical samples are prepared using standard cylindrical molds, which are also used in pressure measurements. Although the first of the model presented in Figure 5 is given out of the mold, a photograph of the second sample in its preparation stage is given. The internal crack, which is very complexly expressed in the simulation setup, is obtained by using styrofoam in the sample. In the second sample, standard rebar is used and styrofoam is used to obtain the void. After the concrete solidified in the molds, it is taken out, kept in the curing tank for 28 days, then dried in air for more than six months and made ready for measurement.

# 5.2 Measurement of Concrete Samples

In many microwave applications, the electromagnetic properties of the material need to be known. Especially in simulations, knowing the complex electromagnetic parameters  $(\varepsilon,\mu,\sigma)$  of the material is important for the accuracy of the simulation results. Measurements of these parameters at microwave frequencies are made using free space, cavity resonators, open-ended coaxial probe and transmission line techniques. The simplest material characterization technique in the broad and

medium frequency bands is transmission line techniques. These techniques can be divided into reflection (single port measurements) and pass reflection (two port measurements) techniques. In the transmission and reflection techniques, the scattering parameters are measured by placing the material inside a coaxial line or a waveguide. This measurement is usually performed using a network analyzer. One of the most valuable devices in the microwave NDT technique is the microwave network analyzer with one or more ports and each port can pass, absorb and reflect electromagnetic energy. The advantages of this device are that it has the flexibility required to test the use of microwave NDT in specific applications, it contains microprocessors that provide calibration and customization for each application, which make it easy to use.

## 5.2.1 Vivaldi Antenna and Vivaldi Antenna Array

The development of ultra-wideband radar systems, the development of additional antenna designs that can provide appropriate performance, and the fact that a lot of work has been done on the propagation of high-energy electromagnetic waves have also led to the development of the GPR method.

Extremely wideband antennas stand out and become very attractive for two reasons. they are coming. First, features such as high communication speed, low power consumption and low cost make extreme broadband antennas increasingly in demand. Second, today's devices require antennas operating at different frequencies for various wireless transmission functions. For this reason, working bands and functions are increasing gradually, which causes difficulties in antenna design such as antenna space limitation, multi-antenna interference. Many broadband antennas can be used to replace very narrowband antennas, which can effectively reduce the number of antennas. The operating frequency range where the antenna parameters such as input impedance, radiation pattern, gain and efficiency are at the desired level can be defined as the bandwidth of an antenna. Vivaldi antenna, Pacman antenna, round bowtie antenna, slit bowtie antenna, horn antennas are the most widely used extreme broadband antennas today.

For a GPR system to work successfully, it must have an appropriate signal-to-noise ratio, an adequate signal-to-noise ratio, adequate target resolution, and depth

resolution. The energy source can be an amplitude, frequency or phase modulated wave signal. The choice of bandwidth, repetition rate and average power depends on path loss and target sizes. The transmitting and receiving antenna are usually the same antenna and are selected to meet the characteristics of the generated waveform. The receiving antenna must be suitable for the modulation type and have a sufficient dynamic range for the path losses to be encountered. Range performance of the GPR system; can be obtained by considering factors such as path loss, target reflectivity, clutter and range of the system. Spatial analysis of radar system; can be determined by considering depth and plan analysis separately.

A series of broadband antennas have been designed for Ground Penetrating Radar applications. While the wave can penetrate deeper in measurements made in the low frequency band, designs are made in the high frequency band to provide better resolution imaging for GPR systems. While trying to increase the gains of the antennas used in GPR systems, on the other hand, efforts are being made to further increase the bandwidth. Considering the bandwidth and gain conditions, studies have been carried out on different antenna types such as bow tie antennas, horn antennas and Vivaldi antennas for GPR applications. Bow tie antennas are widely used for GPR applications due to their high gain value. Large antennas are often used in the GPR system to increase the scan depth or to easily scan shallow targets. Horn antennas with high gain value and bandwidth are also used, as the energy must be spread on the ground for detection. Vivaldi antenna is frequently used in GPR systems because of its high efficiency, high antenna gain, wide bandwidth and simple geometry.

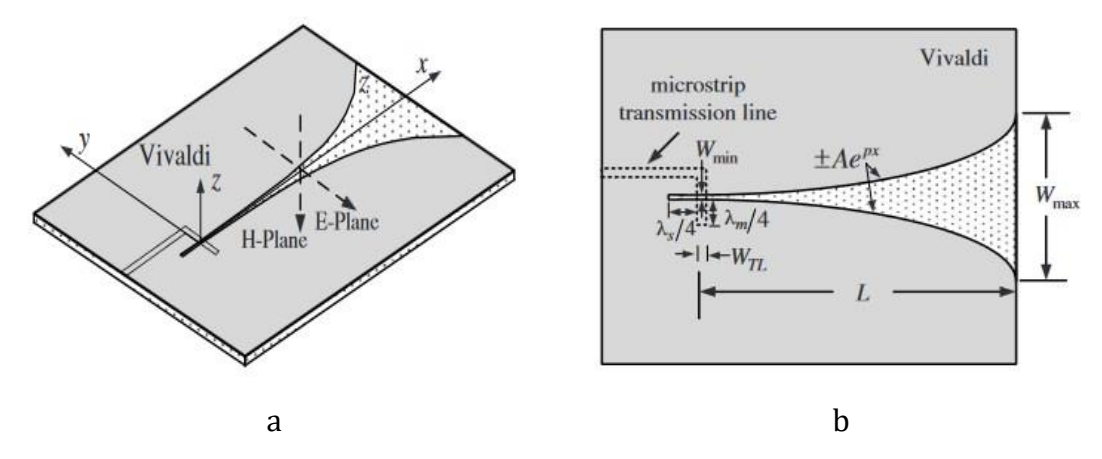


Figure 5.4 Vivaldi Antenna Geometry: (a) 3-D view (b) Top view [130]

The Vivaldi antenna is an example of a broadband antenna. The first designed Vivaldi antenna showed a gain of 10 dB and a bandwidth from 2 GHz to 40 GHz with –20 dB side-lugs. In later broadband applications, antenna arrays are designed using Vivaldi antenna geometry [130]. Vivaldi antennas have radiation characteristics such as high gain, broadband performance, constant beam width and low side lobe level. The general view of the Vivaldi antenna is presented in Figure 5.4. A planar waveguide feeding can also be used in the Vivaldi antenna design, which provides a wide bandwidth. In Vivaldi antennas, the beam width is almost constant over the entire bandwidth. Also, Vivaldi antennas exhibit symmetrical radiation, that is, the beam width is approximately the same in both the E plane and the H plane. As the antenna length increases, the beam width becomes narrower. The taper ratio has a significant effect on the antenna's bandwidth and beam width. In general, as the taper ratio increases, the beam width in the E-plane increases, the beam width in the H-plane decreases, and the bandwidth increases.

Generally, the main beam of a single antenna is relatively wide, and each antenna has low gain values. Antenna arrays are used to increase the gain and reduce the main beam width. An antenna array is created by placing several of a single Vivaldi antenna at equal intervals in one direction and feeding them with signals of the same phase and size. This structure is called a regular linear sequence. Antenna arrays have many advantages over a single antenna. Antenna gain can be increased, and beam width can be reduced with antenna array design. The radiation pattern of the antenna array is affected by the radiation pattern of a single antenna and the radiation pattern of the array factor. The array factor depends on the number of elements, the spacing between the elements, the magnitude of the signal sent to each element, and the phase of the signal sent to each element.

While designing the antenna array, the design is made by considering the wavelength at the highest operating frequency. The distance between the antennas should be smaller than the wavelength at the highest operating frequency. Otherwise, the maximum points will appear on the side flaps as well. The number of elements in the antenna array determines the array orientation. Increasing the number of antennas and antenna spacing results in a narrowing of the main beam

and an improvement in array orientation. The number of antennas must be adjusted to achieve the desired beam width and side-auricular levels [131]. At the same time, increasing the number of antennas results in an increase in the area required to implement the designed array. However, since the increase in the number of antennas will increase the cost, an optimum selection must be made.

#### **5.2.2** Measurement Setup

In the solution of many electromagnetic problems, the main aim is to develop optimization algorithms suitable for the best result by modeling system performances. From this point of view, it is necessary to optimize the system so that the power transmission systems used in electromagnetic circuit systems can be designed with as little loss as possible, so that the used amplifiers and matching circuits can reach the desired power transmission. For this purpose, the parameters of N-port circuits are defined by impedance, admittance and scattering matrices, as is known from classical circuit theory [131]. However, some undesirable situations arise in the definition of these parameters. Defining impedance and admittance matrices as terminated with zero or infinite load does not guarantee that they work for every circuit. In order to eliminate this problem, scattering parameters are used because scattering matrices are defined for gates terminated with a finite load and can be used for almost any circuit. The problems arising in the direct measurement of voltage and current values at microwave frequencies, the difficulties in expressing them and the possibility of direct measurement of scattering (S) parameters have significantly increased the use of the S matrix in solving problems.

In its most general definition, the scattering parameters represent the waves arriving at the gates on the circuit and reflected from the gates on the circuit and are the most practical parameters to use. From a design and software process perspective, using scattering parameters provides benefits related to results in numerical stability and error optimization. The scattering matrix, in its simplest form, can be defined as the measure of the interrelationships of the waves arriving at and reflected from the circuit gates.

Network analyzers designed for this purpose are used to detect these sizes on the circuit. In addition, the elements in the S matrix correspond to quantities that have

a physical meaning. It is possible to summarize this situation with two items: Firstly, the values in the diagonal of the matrix obtained by terminating the other gates in a non-reflective way in a circuit with N gates represent the reflection coefficients of the non-terminated gate. Secondly, all elements except the diagonal show the coefficients that reveal the extent of the transmission between the gates. Sparameters are the most common way of representing VNA measurements, and they can be measured directly with the VNA. The S-parameters obtained from the VNA measurement are usually in the form of a symmetric matrix with rows and columns equal to the number of ports [133].

In a circuit with N gates, the waves arriving at and reflected from the gates are denoted by  $a_i$  and  $b_i$ , respectively. The  $a_i$  and  $b_i$  values can be defined in terms of incident and reflected voltage  $(V_i^+, V_i^-)$  or current  $(I_i^+, I_i^-)$  waves and characteristic impedances as in equations (5.1) and (5.2).

$$a_{i} = \frac{V_{i}^{+}}{\sqrt{Z_{0i}}} = I_{i}^{+} \sqrt{Z_{0i}}$$
 (5.1)

$$b_i = \frac{V_i^-}{\sqrt{Z_{0i}}} = I_i^- \sqrt{Z_{0i}}$$
 (5.2)

The generalized scattering matrix of a circuit with N gates and the general form of each element of the matrix can be expressed by equations (5.3) and (5.4).

$$\begin{bmatrix} b_1 \\ \cdot \\ b_N \end{bmatrix} = \begin{bmatrix} S_{11} & S_{12} & \cdot & S_{1N} \\ S_{21} & \cdot & \cdot & \cdot \\ \cdot & \cdot & \cdot & \cdot \\ S_{N1} & \cdot & \cdot & S_{NN} \end{bmatrix} \begin{bmatrix} a_1 \\ \cdot \\ \cdot \\ a_N \end{bmatrix}$$
(5.3)

$$S_{ij} = \frac{b_i}{a_j} \bigg|_{a_k = 0, k \neq j} = \frac{V_i^- / \sqrt{Z_{0i}}}{V_j^+ / \sqrt{Z_{0j}}} \bigg|_{V_k^+ = 0, k \neq j} = \frac{I_i^- / \sqrt{Z_{0i}}}{I_j^+ / \sqrt{Z_{0j}}} \bigg|_{V_k^+ = 0, k \neq j}$$
(5.4)

Similarly, in particular, the S matrix and elements of the S matrix of a two-port microwave circuit can be expressed as in equations (5.5) and (5.6).

$$\begin{bmatrix} b_1 \\ b_2 \end{bmatrix} = \begin{bmatrix} S_{11} & S_{12} \\ S_{21} & S_{22} \end{bmatrix} \begin{bmatrix} a_1 \\ a_2 \end{bmatrix}$$
 (5.5)

$$S_{11} = \frac{b_1}{a_1}\Big|_{a_2=0}, S_{21} = \frac{b_2}{a_1}\Big|_{a_2=0}, S_{12} = \frac{b_1}{a_2}\Big|_{a_1=0}, S_{22} = \frac{b_2}{a_2}\Big|_{a_1=0}$$
 (5.6)

In this study, reflection and transmission coefficients are obtained from the parameters obtained by measuring [132].

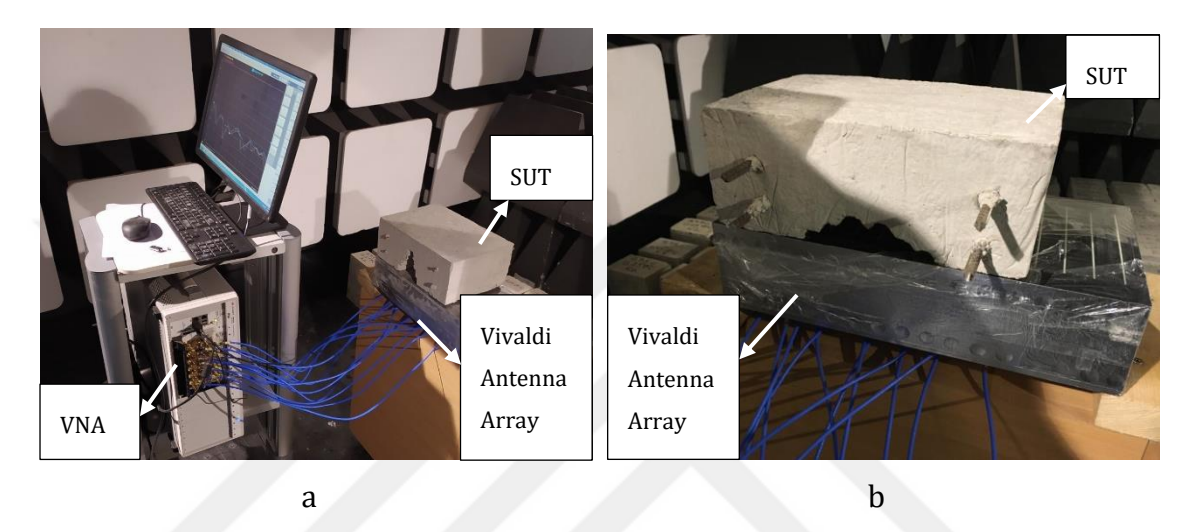


**Figure 5.5** Measurement Setup for Rectangular Models: (a) Case A, (b) Case B [114]

For the S-parameter  $S_{ij}$ , the subscript i indicates the exciting port (input port) and the subscript j denotes the output port. Diagonal elements of the S-matrix represent reflection and off-diagonal elements of this matrix are used to explain transmission from port j to port i. For example,  $S_{11}$  is the reflection seen looking into port 1.  $S_{21}$  can be find by applying an incident wave at port 1 and measuring the outcoming wave at port 2. This is equivalent to the transmission from port 1 to port 2. Because of the symmetry  $S_{21}$  is equivalent to the  $S_{12}$ . In order to calculate reflection and scattering coefficients of our samples at microwave frequencies, VNA designed for simultaneous measurement of S-parameters of networks with more than two ports is used.

In Figure 5.5 measurement setup is given for rectangular concrete models. Measurement is made in an anechoic chamber using Vivaldi antenna array, VNA, computer, and specimen under test (SUT). Eight Vivaldi antennas are placed in

contact with the defect layer of concrete. Since the concrete is placed in contact with eight antennas in the measurement setup, eight sources are used in the simulations. Measurements are made in the 0.4-4.0 GHz frequency range.

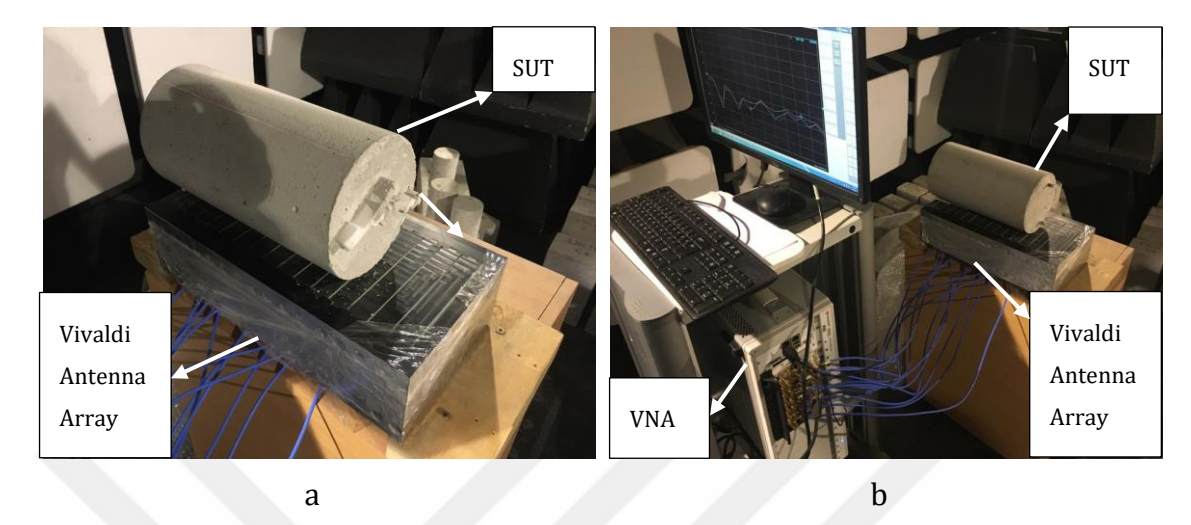


**Figure 5.6** Measurement Setup for Cylindrical Models: (a) Cylinder B, (b) Cylinder C

The physical structures of the cylindrical models and measurement setup is given in Figure 5.6. In the first concrete sample, there are two rebars and two styrofoam balls to express the void since its dielectric constant is very close to the dielectric constant of air. In the second concrete sample, although there is no rebar, instead of using styrofoam with a smooth surface, a broken styrofoam is used to express the branching crack in the concrete.

# 5.3 Calculating the Reflection and Transmission Coefficient

The scattering parameter, or in other words the S-parameter, measured with the aid of the transmitting and receiving radar antennas is known as the forward transmission gain. In microwave measurements, reflection and transmission coefficients are obtained from the measured or simulated scattering parameters. Since the system that provides the measurement of the scattering parameters is symmetrical in the y-axis, the scattering matrix is also symmetrical  $(S_{12} = S_{21})$ . According to this the scattering parameters can be given as follows:

$$S_{11} = R_1^2 \frac{\Gamma(1 - T^2)}{1 - \Gamma^2 T^2}, \ S_{22} = R_2^2 \frac{\Gamma(1 - T^2)}{1 - \Gamma^2 T^2}, \ S_{21} = R_1 R_2 \frac{\Gamma(1 - T^2)}{1 - \Gamma^2 T^2}$$
(5.7)

where,  $\Gamma$  is reflection coefficient, T is transmission coefficient,  $R_1$  and  $R_2$  are the reference plane transducers on the two ports. The reflection and transmission coefficients from the scattering parameters  $\left(S_{11},S_{12},S_{21},S_{21}\right)$  can be found as follows:

$$\Gamma = K \pm \sqrt{K^2 - 1} \tag{5.8}$$

$$K = \frac{\left(S_{11}^2 - S_{21}^2\right) + 1}{2S_{11}} \tag{5.9}$$

Positive or negative sign in the equation (5.8) is selected according to the value satisfying the  $|\Gamma| \le 1$  condition and transmission coefficient can be calculated as in (5.9).

$$T = \frac{\left(S_{11} + S_{21}\right) - \Gamma}{1 - \left(S_{11} + S_{21}\right)\Gamma} \tag{5.10}$$

Electric and magnetic permeability constants can also be calculated using scattering parameters.

$$\mu_r = \frac{1+\Gamma}{\left(1-\Gamma\right)\Lambda\sqrt{\left(1/\lambda_0^2\right)-\left(1/\lambda_c^2\right)}} \tag{5.11}$$

$$\varepsilon_r = \frac{\lambda_0^2}{\mu_r \left[ \left( \frac{1}{\lambda_c^2} \right) - \left( \frac{1}{\Lambda^2} \right) \right]}$$
 (5.12)

where  $\Lambda$  can be defined as follows:

$$\frac{1}{\Lambda^2} = -\left[\frac{1}{2\pi L} \ln\left(\frac{1}{T}\right)\right]^2 \tag{5.13}$$

The scattering parameter, or in other words the S-parameter, measured with the aid of the transmitting and receiving radar antennas is known as the forward transmission gain. It is not possible to express the complex permittivity value

directly in terms of the transmission coefficient  $T^*$ . The magnitude of  $T^*$  expressed in decibel (dB) can be expressed in terms of  $S_{21}^*$  as [105]:

$$T_{dB} = 10.\log(S_{21}^*.\overline{S}_{21}^*)$$
 (5.14)

where  $T_{dB}$  is a real number and  $\overline{S}_{21}^*$  is the complex conjugate of  $S_{21}^*$ .

The measurement and FDTD calculation results for rectangular concrete samples are presented in Figure 5.7.

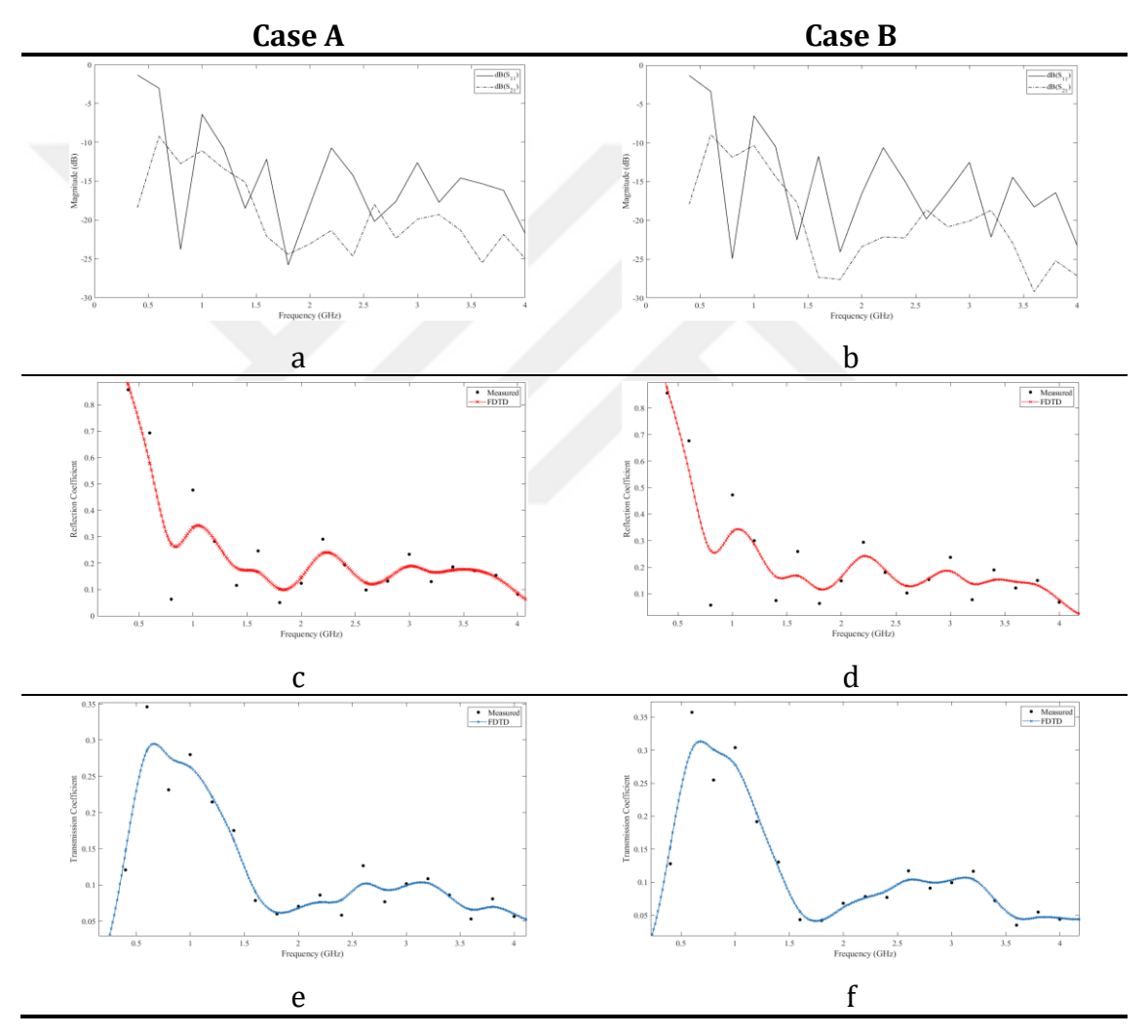


**Figure 5.7** Measurement Result: (a) S-parameters for Case A, (b) S-parameters for Case B, (c) Reflection Coefficient for Case A, (d) Reflection Coefficient for Case B, (e) Transmission Coefficient for Case B

The S<sub>11</sub> and S<sub>12</sub> parameters for Case A and Case B are presented in Figures 5.7 (a, b), respectively. The reflection and transmission coefficients are calculated using the S-parameters obtained from the measurement by coefficient calculation formula [48]. In addition, the reflection and transmission coefficients are computed with the FDTD method [45], and the results are compared in Figures 5.7 (c-f). It is seen that the measurement results and the FDTD results are overlapped.

The measurement and FDTD calculation results for cylindrical concrete samples are presented in Figure 5.8.

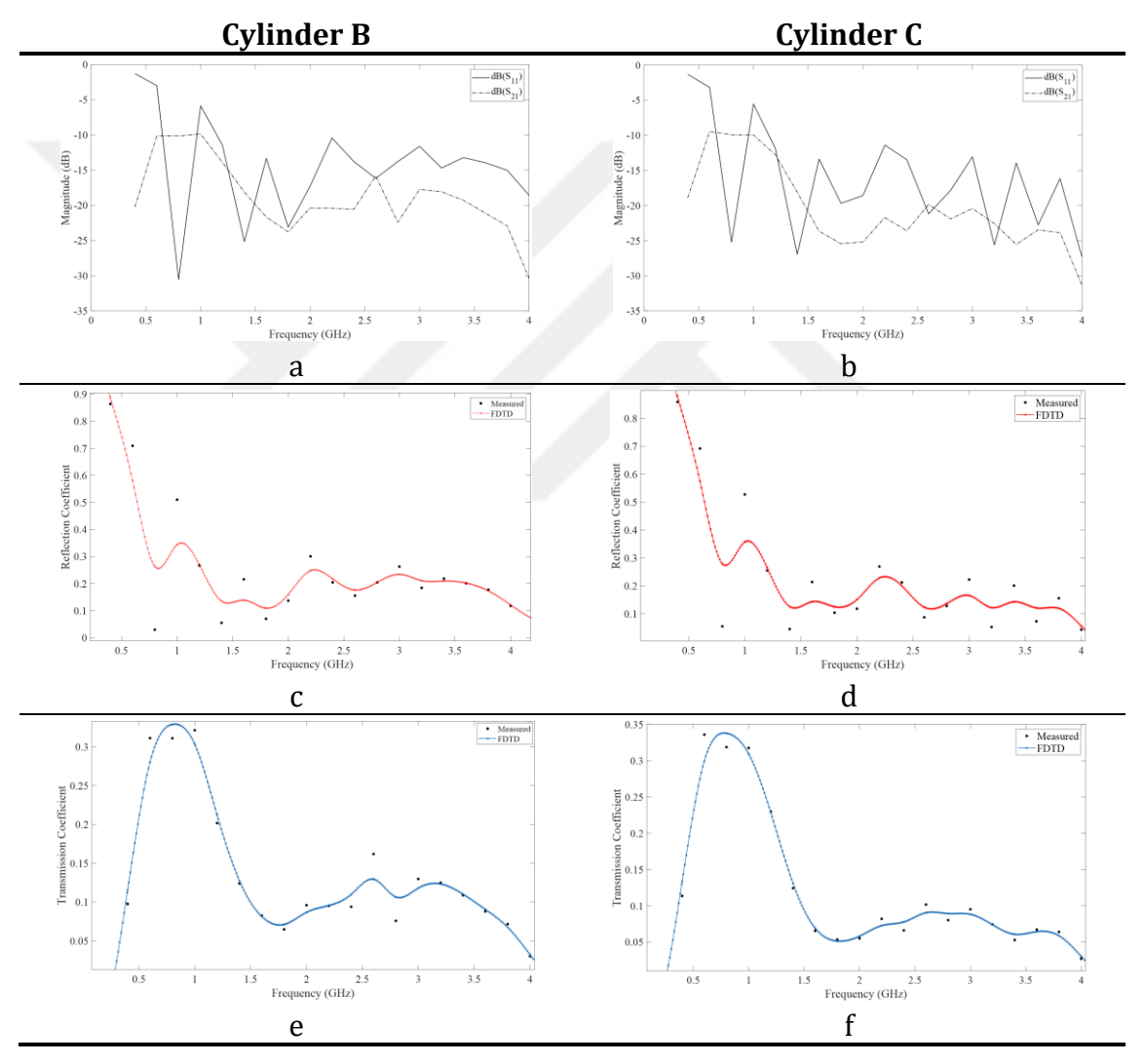


**Figure 5.8** Measurement Results: (a) S-parameters for Cylinder B, (b) S-parameters for Cylinder C, (c) Reflection Coefficient for Cylinder B, (d) Reflection Coefficient for Cylinder C, (e) Transmission Coefficient for Cylinder B, (e)

Transmission Coefficient for Cylinder C

The S<sub>11</sub> and S<sub>12</sub> parameters for Cylinder B and Cylinder C are presented in Figures 5.9 (a, b), respectively. The reflection and transmission coefficients are calculated using the S-parameters obtained from the measurement by coefficient calculation formula given in equations (5.8) and (5.10). In addition, the reflection and transmission coefficients are computed with the FDTD method [45], and the results are compared in Figures 5.8 (c-f). It can be seen that the measurement results and the FDTD results overlap.

## RESULTS AND DISCUSSION

In this thesis, simulation of rectangular concretes with different crack types, concrete structures containing different building materials, and cylindrical concretes containing defects is carried out by microwave radar NDT method for non-destructive testing. In addition, some of the simulated samples are physically created and measured in an anechoic chamber with the help of the Vivaldi antenna array, and the reflection and transmission coefficients obtained with FDTD and the reflection and transmission coefficients obtained from microwave radar measurement are compared. The findings obtained in this study are summarized below.

- The definition of non-destructive testing technique has been made, the types of non-destructive testing techniques and their usage purposes have been mentioned in summary. The advantages and disadvantages of non-destructive testing methods are compared to each other and their usage areas are discussed. The NDT methods used in the inspection of concrete structures have been specified, and since it will be used in this study, the microwave radar NDT method is explained in more detail and its advantages are emphasized.
- Maxwell's equations are discretized in space and time using the FDTD algorithm to simulate of how the electromagnetic wave propagates in concrete which includes rebar, cracks and other defects. The advantages of the FDTD method are briefly mentioned and discretizing the Maxwell's curl equations are explained. By examining the 3-D update equation of the FDTD method, its reduction to 2-D and 1-D has been studied in detail. The update equations of the field components in the relevant group are obtained by dividing the field components into two groups as TE<sub>z</sub> and TM<sub>z</sub> mode.

- Sources create electric and magnetic fields in the FDTD space. Therefore, resources are necessary components of FDTD simulation, and their types vary according to the problem to be applied. In general terms, the sources used in numerical solutions are introduced and the Gaussian pulse used in this study is examined. Since the numerical calculations must be terminated after a certain step, the absorber boundary condition is mentioned and the PML boundary condition, which is the most advantageous boundary condition in FDTD calculations, is introduced.
- Three different types of cracks that may be encountered in a concrete structure are defined. Rectangles are used one after another which deepening and shrinking downward for defining a surface crack. Circles are utilized to identify defect due to a wide breakage of the concrete surface. An interior crack whose depth and structure cannot be determined from the surface is considered as the Riemann integral domain. This domain is defined as the region between two curves as in the integral expression and is divided into smaller subdomains. The crack is expressed by assuming that these subregions are filled with air. Since the region formed by these subregions does not have a smooth shape, the most realistic crack definition is made.
- The simulation setups of six different layered rectangular structures with different construction materials are prepared. Some of these rectangular structures contain pavements, while one contains both mortar and pavement. One contains rebar and voids, while one contains soil at the base. Microwave radar technique non-destructive examination is also carried out for concrete filled composite piles used in environments with very high humidity.
- In simulations, it is investigated which mode is more advantageous in which situations by comparing the field distributions from both TE<sub>z</sub> mode and TM<sub>z</sub> mode. While TM mode is more suitable for observing the propagation of the EM wave as it propagates from one medium to a different medium and to detect fewer deep cracks, TE mode gives better results in determining the shapes of the deep cracks and the positions of the rebars. Surface cracks, rebars, and internal crack are simulated at 1.5 GHz, 3.0 GHz and 6.0 GHz

frequencies, 2-D and 3-D states of the field distributions are given. In the simulation, as the frequency increases, the scattering of the wave also increases, making it difficult to detect defects and rebars. For this reason, it has been observed that the crack and rebar detection simulation give better results around the 1.5 GHz frequency.

In order to validate the results obtained from the simulation setup, concrete samples of two of the rectangular geometries and two of the cylindrical geometries discussed in the simulation setup were prepared. For this purpose, a rectangular sample with deep surface crack and rebar and a rectangular sample with shallow surface crack and rebar are prepared. Similar to the simulation setup described in the section on cylindrical concrete structures, a cylindrical concrete sample containing internal crack and a cylindrical concrete sample containing rebar and air gap are prepared. The prepared four concrete samples are dried in air and measured nondestructively in an anechoic chamber using the Vivaldi antenna array and VNA. The reflection and transmission coefficients expressed with the help of the scattering parameters obtained from the measurement using VNA and the reflection and transmission coefficients calculated with the help of the FDTD approach are compared for verification purposes. Reflection and transmission coefficients obtained by FDTD approach and reflection and transmission coefficients obtained from measurement of rectangular concrete samples with different surface cracks and cylindrical concrete samples with internal crack and defects overlap. Since measurement, which is an experimental study, requires time and cost, it has been observed that modeling air-dry concrete using the FDTD approach gives reliable results.

- [1] T. V. Fursa, M. V. Petrov, and D. D. Dann, "Developing a nondestructive method for revealing defective areas in reinforced concrete under bending conditions", Russian Journal of Nondestructive Testing, vol. 55, no. 4, pp. 293-298, 2019.
- [2] O. Büyüköztürk and H. C. Rhim, "Radar imaging of concrete specimens for non-destructive testing", Construction and Building Materials, vol. 11, no. 3, pp. 195-198, 1997.
- [3] O. Büyüköztürk, "Imaging of concrete structures", NDT & E International, vol. 31, no. 4, pp. 233-243, 1998.
- [4] O. Büyüköztürk and H. C. Rhim, "Modeling of electromagnetic wave scattering by concrete specimens", Cement and concrete research, vol. 25, no. 5, pp. 1011-1022, 1995.
- [5] L. Jiao, Q. Ye, X. Cao, D. Huston, and T. Xia, "Identifying concrete structure defects in GPR image", Measurement, vol. 160, 107839, 2020.
- [6] M. A. Rasol, V. Pérez-Gracia, F. M. Fernandes et. al., "GPR laboratory tests and numerical models to characterize cracks in cement concrete specimens, exemplifying damage in rigid pavement" Measurement, vol. 158,107662, 2020.
- [7] T. Y. Yu, B. Boyaci, and H. F. Wu, "Simulated transient electromagnetic response for the inspection of GFRP-wrapped concrete cylinders using radar NDE", Research in Nondestructive Evaluation, vol. 24, no. 3, pp. 125-153, 2013.
- [8] H. C. Rhim and O. Büyüköztürk, "Wideband microwave imaging of concrete for nondestructive testing", Journal of Structural Engineering, vol. 126, no. 12, pp. 1451-1457, 2000.
- [9] T. Takagi, J. R Bowler, and Y. Yoshida, "Electromagnetic nondestructive evaluation" vol. 1, IOS press, 1997.
- [10] J. Lachowicz and M. Rucka, "Experimental and numerical investigations for GPR evaluation of reinforced concrete footbridge", 2016 16th International Conference on Ground Penetrating Radar (GPR) pp. 1-6, IEEE, 2016.
- [11] S. Zhao, I. L Al-Qadi, and S. Wang, "Prediction of thin asphalt concrete overlay thickness and density using nonlinear optimization of GPR data", NDT & E International, vol. 100, pp. 20-30, 2018.
- [12] J. Lachowicz and M. Rucka, "A concept of heterogeneous numerical model of concrete for GPR simulations", 9th International Workshop on Advanced Ground Penetrating Radar (IWAGPR), pp. 1-4 IEEE, 2017.
- [13] J. Lachowicz and M. Rucka, "A novel heterogeneous model of concrete for numerical modelling of ground penetrating radar", Construction and Building Materials, 227, 116703, 2019
- [14] T. Asakura, M. Toyoda, and T. Miyajima, "Numerical and experimental investigation on structure-borne sound transmission in multilayered concrete structures", Journal of Sound and Vibration, vol. 413, pp. 1-25, 2018.

- [15] S. Kawataki, T. Tanaka, S. Doi, S. Uchida, and M. Q. Feng, "Nondestructive inspection of voids in concrete by multi-layered scanning method with electromagnetic waves", IEEE International Conference on Mechatronics (ICM) pp. 336-341, IEEE, 2017.
- [16] Y. K. Zhu, G. Y. Tian, R. S Lu, and H. Zhang, "A review of optical NDT technologies" Sensors, vol. 11, no. 8, pp. 7773-7798, 2011.
- [17] H. N. Li, D. S. Li, and G. B. Song, "Recent applications of fiber optic sensors to health monitoring in civil engineering", Engineering structures, vol. 26, no. 11, pp. 1647-1657, 2004.
- [18] X. Gao, Y. Li, X. Zhou, X. Dai, Y. Zhang, D. You, N. Zhang, "Multidirectional magneto-optical imaging system for weld defects inspection", Optics and Lasers in Engineering, 124, 105812, 2020.
- [19] R. Ambu, F. Aymerich, F. Ginesu, and P. Priolo, "Assessment of NDT interferometric techniques for impact damage detection in composite laminates" Composites Science and Technology, vol. 66, no. 2, pp. 199-205, 2006.
- [20] M. S. Safizadeh and T. Azizzadeh, "Corrosion detection of internal pipeline using NDT optical inspection system", NDT & E International, vol. 52, pp. 144-148, 2012.
- [21] B. A. Graybeal, B. M. Phares, D. D. Rolander, M. Moore, and G. Washer, "Visual inspection of highway bridges", Journal of nondestructive evaluation, vol. 21, no. 3, pp. 67-83, 2002.
- [22] A. Carcione, P. Blanloeuil, and M. Veidt, "Demodulation technique to identify nonlinear characteristics of vibro-acoustic NDT measurements", Journal of Sound and Vibration, 466, 115014, 2020.
- [23] A. Mirmiran and S. Philip, "Comparison of acoustic emission activity in steel-reinforced and FRP-reinforced concrete beams", Construction and Building Materials, vol. 14, no. 6, pp. 299-310, 2000.
- [24] P. Duffour, M. Morbidini, and P. Cawley, "Comparison between a type of vibro-acoustic modulation and damping measurement as NDT techniques", NDT & E International, vol. 39, no. 2, pp. 123-131, 2006
- [25] R. Ludwig, Z. You, and R. Palanisamy," Numerical simulations of an electromagnetic acoustic transducer-receiver system for NDT applications", IEEE Transactions on Magnetics, vol. 29, no. 3, pp. 2081-2089, 1993.
- [26] N. S. V. N Hanuman, and T. Bose, "Acoustic nondestructive evaluation of Glass-Fibre Reinforced Plastic (GFRP) Plate", NDE Conference & Exhibition of the society for NDT (ISNT), 2018.
- [27] M. Hirao, H. Ogi, and H. Yasui," Contactless measurement of bolt axial stress using a shear-wave electromagnetic acoustic transducer", Ndt & E International, vol. 34, no. 3, pp. 179-183, 2001.
- [28] R. Murayam and K. Misumi, "Development of a non-contact stress measurement system during tensile testing using the electromagnetic acoustic transducer for a Lamb wave", NDT & E International, vol. 39, no. 4, pp. 299-303, 2006.
- [29] G. R. Stultz, R. W. Bono, and M. I. Schiefer, "Fundamentals of resonant acoustic method NDT", Advances in powder metallurgy and particulate materials, vol. 3, no. 11, 2005.

- [30] M. Scheerer, A. Peldszus, M. Stadtschnitzer, and R. Wagner, "Modern acoustic NDT methods for the off-and online detection of damages in composite aeronautic structures", Proc. 3rd IALCCE, Vienna, Austria, pp. 1430-1437, 2012.
- [31] R. Hamid, K. M Yusof, and M. F. M. Zain, "A combined ultrasound method applied to high performance concrete with silica fume", Construction and Building Materials, vol. 24, no. 1, pp. 94-98, 2010.
- [32] H. Azari, S. Nazarian, and D. Yuan, "Assessing sensitivity of impact echo and ultrasonic surface waves methods for nondestructive evaluation of concrete structures", Construction and Building Materials, vol. 71, pp. 384-391, 2014.
- [33] I. Solodov and G. Busse, "New advances in air-coupled ultrasonic NDT using acoustic mode conversion", Proc. EC NDT, 2006.
- [34] Y. Z. Pappas, A. Kontsos, T. H Loutas, and V. Kostopoulos, "On the characterization of continuous fibres fracture by quantifying acoustic emission and acousto-ultrasonics waveforms", NDT & E International, vol. 37 no. 5, pp. 389-401, 2004.
- [35] X. Zhang, T. Jackson, and E. Lafond, "Stiffness properties and stiffness orientation distributions for various paper grades by non-contact laser ultrasonics", NDT & E International, vol.39 no. 7, pp. 594-601, 2006.
- [36] D. G. Aggelis, E. Z. Kordatos, D. V. Soulioti, and T. E. Matikas, "Combined use of thermography and ultrasound for the characterization of subsurface cracks in concrete", Construction and Building Materials, vol. 24, no. 10, pp. 1888-1897, 2010.
- [37] L. J. Jacobs and R. W. Whitcomb, "Laser generation and detection of ultrasound in concrete", Journal of nondestructive evaluation, vol. 16, no. 2, pp.57-65, 1997.
- [38] C. Payan, A. Quiviger, V. Garnier, J. F. Chaix, and J. Salin, "Applying diffuse ultrasound under dynamic loading to improve closed crack characterization in concrete", The Journal of the Acoustical Society of America, vol. 134, no. 2, EL211-EL216, 2013.
- [39] I. N. Prassianakis and P. Giokas, "Mechanical properties of old concrete using destructive and ultrasonic non-destructive testing methods", Magazine of Concrete Research, vol. 55, no. 2, pp. 171-176, 2003.
- [40] Z. M. Sbartaï, D. Breysse, M. Larget, and J. P. Balayssac, "Combining NDT techniques for improved evaluation of concrete properties", Cement and Concrete Composites, vol. 34, no. 6, pp. 725-733, 2012.
- [41] M. J. Lovejoy, "Magnetic particle inspection: a practical guide", Springer Science & Business Media, 2012.
- [42] J. R. Bowler and N. Bowler, "Evaluation of the magnetic field near a crack with application to magnetic particle inspection", Journal of Physics D: Applied Physics, vol. 35, no. 18, 2237, 2002.
- [43] D. C. Jiles, "Review of magnetic methods for nondestructive evaluation (Part 2)", NDT international, vol. 23, no. 2, pp. 83-92, 1990.
- [44] A. Zolfaghari and F. Kolahan, "Reliability and sensitivity of magnetic particle nondestructive testing in detecting the surface cracks of welded components" Nondestructive Testing and Evaluation, vol. 33, no. 3, pp. 290-300, 2018.

- [45] S. K. Burke and R. J. Ditchburn, "Review of literature on probability of detection for magnetic particle nondestructive testing", 2013.
- [46] A. Sophian, G. Y. Tian, D. Taylor, and J. Rudlin, "Electromagnetic and eddy current NDT: a review", Insight, vol. 43, no. 5, pp. 302-306, 2001.
- [47] A. Sophian, G. Y Tian, D. Taylor, and J. Rudlin," A feature extraction technique based on principal component analysis for pulsed Eddy current NDT", NDT & e International, vol. 36, vol. 1, pp.37-41, 2003.
- [48] M. Pan, Y. He, G. Tian, D. Chen, and F. Luo," Defect characterization using pulsed eddy current thermography under transmission mode and NDT applications", Ndt & E International, vol. 52, pp. 28-36, 2012.
- [49] D. Zhou, G. Y. Tian, B. Zhang, M. Morozov, and H. Wang, "Optimal features combination for pulsed eddy current NDT." Nondestructive Testing and Evaluation, vol. 25, no. 2, pp. 133-143, 2010.
- [50] Y. Yu, Y. Zou, M. Al Hosani, and G. Tian," Conductivity invariance phenomenon of eddy current NDT: Investigation, verification, and application", IEEE Transactions on Magnetics, vol. 53, no. 1, pp. 1-7, 2016.
- [51] G. Y. Tian, A. Sophian, D. Taylor, and J. Rudlin," Wavelet-based PCA defect classification and quantification for pulsed eddy current NDT", IEE Proceedings-Science, Measurement and Technology, vol. 152, no. 4, pp. 141-148, 2005.
- [52] Y. Y. Hung, Y. S. Chen, S. P. Ng, L. Liu, Y. H. Huang, B. L. Luk, and P. S. Chung, "Review and comparison of shearography and active thermography for nondestructive evaluation", Materials Science and Engineering: R: Reports, vol. 64, no. 5, pp. 73-112, 2009.
- [53] S. M. Shepard, "Introduction to active thermography for non-destructive evaluation", Anti-Corrosion Methods and Materials, 1997.
- [54] C. Ibarra-Castanedo, J. M. Piau, S. Guilbert, N. P. Avdelidis, M. Genest, A. Bendada, and X. P. Maldague, "Comparative study of active thermography techniques for the nondestructive evaluation of honeycomb structures", Research in Nondestructive Evaluation, vol. 20, no. 1, pp. 1-31, 2009.
- [55] B. B. Lahiri, S. Bagavathiappan, P. R. Reshmi, J. Philip, T. Jayakumar, and B. Raj, "Quantification of defects in composites and rubber materials using active thermography", Infrared Physics & Technology, vol. 55 no. 2, pp. 191-199, 2012.
- [56] M. Lizaranzu, A. Lario, A. Chiminelli, and I. Amenabar, "Non-destructive testing of composite materials by means of active thermography-based tools" Infrared Physics & Technology, vol. 71, pp. 113-120, 2015.
- [57] A. P. Chrysafi, N. Athanasopoulos, and N. J. Siakavellas," Damage detection on composite materials with active thermography and digital image processing", International journal of thermal sciences, vol. 116, pp. 242-253, 2017.
- [58] N. P. Migoun and N. V. Delenkovsky, "The ways of penetrant testing applicability for rough surfaces", Proceedings of 17th World Conf. on NDT, Shanghai, China (p. 25), 2008.
- [59] N. P. Migoun and N. V. Delenkovskii, "Improvement of penetrant-testing methods", Journal of Engineering Physics and Thermophysics, vol. 82, no. 4, pp. 734-742, 2009.

- [60] D. E. Bray and D. McBride, "Nondestructive testing techniques" NASA STI/Recon Technical Report A, 93, 17573, 1992.
- [61] U. Zscherpel, U. Ewert, and K. Bavendiek, "Possibilities and Limits of Digital Industrial Radiology: -The new high contrast sensitivity technique-Examples and system theoretical analysis", International Symposium on Digital industrial Radiology and Computed Tomography, pp. 25-27, 2007.
- [62] R. Halmshaw, "Industrial radiology: theory and practice", Springer Science & Business Media, vol. 1, 2012.
- [63] H. Berger, "Trends in radiologic NDT", Materials Evaluation, vol. 52, no. 11, 1994.
- [64] U. Ewert, K. Bavendiek, J. Robbins, U. Zscherpel, C. Bueno, T. Gordon, and D. Mishra," New compensation principles for enhanced image quality in industrial radiology with digital detector arrays", Materials Evaluation, vol. 68, no. 2, pp. 163-168, 2010.
- [65] C. Colla, P. C. Das, D. McCann, and M. C. Forde, "Sonic, electromagnetic and impulse radar investigation of stone masonry bridges" NDT & E International, vol. 30, no. 4, pp. 249-254, 1997.
- [66] T. Yu, T. K. Cheng, A. Zhou, and D. Lau, "Remote defect detection of FRP-bonded concrete system using acoustic-laser and imaging radar techniques", Construction and Building Materials, vol. 109, pp. 146-155, 2016.
- [67] G. De Angelis, M. Meo, D. P. Almond, S. G. Pickering, and S. L. Angioni, "A new technique to detect defect size and depth in composite structures using digital shearography and unconstrained optimization" Ndt & E International, vol. 45, no. 1, pp. 91-96, 2012.
- [68] M. M. Tajdini and C. M.Rappaport, "An efficient forward model of ground penetrating radar for sensing deteriorated bridge decks, IEEE Antennas and Propagation Society International Symposium (APSURSI), pp. 1022-1023, IEEE, 2013.
- [69] M. M. Tajdini and C. M. Rappaport," Analytic analysis of ground penetrating radar wave scattering of reinforced concrete bridge decks", IEEE International Geoscience and Remote Sensing Symposium-IGARSS, pp. 4066-4069, IEEE, 2013.
- [70] O. Buyukozturk and B. Hearing, "Crack propagation in concrete composites influenced by interface fracture parameters", International Journal of Solids and Structures, vol. 35, no. 31, pp. 4055-4066, 1998.
- [71] O. Büyüköztürk and T. Y. Yu, "Structural health monitoring and seismic impact assessment", Proceedings of the 5th National Conference on Earthquake Engineering, 2003.
- [72] M. T. Ghasr, S. Kharkovsky, R. Bohnert, B. Hirst, and R. Zoughi, "30 GHz linear high-resolution and rapid millimeter wave imaging system for NDE", IEEE transactions on antennas and propagation, vol. 61, no. 9, pp. 4733-4740, 2013.
- [73] C. Y. Yeh and R. Zoughi, "A novel microwave method for detection of long surface cracks in metals", IEEE Transactions on Instrumentation and Measurement, vol. 43, no. 5, pp. 719-725, 1994.
- [74] L. Jiao, Q. Ye, X. Cao, D. Huston, and T. Xia, "Identifying concrete structure defects in GPR image", Measurement, vol. 160, 107839, 2020.

- [75] O. Gunes and O. Buyukozturk, "Simulation-based microwave imaging of plain and reinforced concrete for nondestructive evaluation", International Journal of Physical Sciences, vol. 7, no. 3, pp. 383-393, 2012.
- [76] T. Yu, T. K. Cheng, A. Zhou, and D. Lau, "Remote defect detection of FRP-bonded concrete system using acoustic-laser and imaging radar techniques", Construction and Building Materials, vol. 109, pp. 146-155, 2016.
- [77] K. Agred, G. Klysz, and J. P. Balayssac, "Location of reinforcement and moisture assessment in reinforced concrete with a double receiver GPR antenna" Construction and Building Materials, vol. 188, pp. 1119-1127, 2018.
- [78] Q. Feng, J. Cui, Q. Wang, S. Fan, Q. Kong, "A feasibility study on real-time evaluation of concrete surface crack repairing using embedded piezoceramic transducers", Measurement, vol. 122, pp. 591-596, 2018.
- [79] K. H. Lee, C. C. Chen, F. L Teixeira, and R. Lee, "Modeling and investigation of a geometrically complex UWB GPR antenna using FDTD", IEEE Transactions on Antennas and Propagation, vol. 52, no. 8, pp. 1983-1991, 2004.
- [80] F. M. Fernandes and J. C. Pais," Laboratory observation of cracks in road pavements with GPR", Construction and Building Materials, vol. 154, pp. 1130-1138, 2017.
- [81] R. Combrinck, L. Steyl, and W. P. Boshoff, "Influence of concrete depth and surface finishing on the cracking of plastic concrete", Construction and Building Materials, vol. 175, 621-628, 2018.
- [82] D. Feng, X. Wang, and B. Zhang," Specific evaluation of tunnel lining multidefects by all-refined GPR simulation method using hybrid algorithm of FETD and FDTD", Construction and Building Materials, vol. 185, pp. 220-229, 2018.
- [83] H. Rathod and R. Gupta, "Sub-surface simulated damage detection using Non-Destructive Testing Techniques in reinforced-concrete slabs" Construction and Building Materials, vol. 215, pp. 754-764, 2019.
- [84] W. W. L. Lai, X. Derobert, and P. Annan, "A review of Ground Penetrating Radar application in civil engineering: A 30-year journey from Locating and Testing to Imaging and Diagnosis", Ndt & E International, vol. 96, pp. 58-78, 2018.
- [85] M. A. Rasol, V. Pérez-Gracia, M. Solla, J. C. Pais, F. M. Fernandes, and C. Santos, "An experimental and numerical approach to combine Ground Penetrating Radar and computational modeling for the identification of early cracking in cement concrete pavements", NDT & E International, vol. 115, 102293, 2020.
- [86] E. A. Jiya, N. S. N. Anwar, S. A. Bala, and E. Bello, "Microwave imaging technique for detection of multiple Line cracks in concrete material", International Journal of Human and Technology Interaction (IJHaTI), vol. 2, no. 2, pp. 49-56, 2018.
- [87] D. M. Sullivan, "Electromagnetic simulation using the FDTD method" John Wiley & Sons, 2013.
- [88] K. S. Kunz, and R. J. Luebbers, "The finite difference time domain method for electromagnetics" CRC press, 1993.

- [89] A. Z. Elsherbeni and V. Demir, "The finite-difference time-domain method for electromagnetics with MATLAB simulations", SciTech Publishing, 2009.
- [90] A. Taflove and S. C. Hagness, "Computational electrodynamics", vol. 28, Norwood, MA: Artech house publishers, 2000.
- [91] K. Belli, H. Zhan, S. Wadia-Fascetti, and C. Rappaport, "Comparison of the accuracy of 2D VS. 3D FDTD air-coupled GPR modeling of bridge deck deterioration", Research in Nondestructive Evaluation, vol. 20, no. 2, pp. 94-115, 2009.
- [92] D. Insana and C. M. Rappaport, "Using FDFD technique in two-dimensional TE analysis for modeling clutter in wall penetrating radar, International Journal of Antennas and Propagation, 2014.
- [93] K. Yee, "Numerical solution of initial boundary value problems involving Maxwell's equations in isotropic media", IEEE Transactions on antennas and propagation, vol. 14, no. 3, pp. 302-307, 1996.
- [94] J. P. Berenger, "A perfectly matched layer for the absorption of electromagnetic waves", Journal of computational physics, vol. 114, no. 2, pp. 185-200, 1994.
- [95] J. P. Berenger, "Perfectly matched layer for the FDTD solution of wave-structure interaction problems", IEEE Transactions on antennas and propagation, vol. 44, no. 1, pp. 110-117, 1996.
- [96] W. V. Andrew, C. A. Balanis, and P. A. Tirkas, "A comparison of the Berenger perfectly matched layer and the Lindman higher-order ABC's for the FDTD method", IEEE Microwave and guided wave letters, vol. 5, no. 6, pp. 192-194, 1995.
- [97] J. P. Berenger, "Three-dimensional perfectly matched layer for the absorption of electromagnetic waves", Journal of computational physics, vol. 127, no. 2, pp. 363-379, 1996.
- [98] J. C. Veihl and R. Mittra, "An efficient implementation of Berenger's perfectly matched layer (PML) for finite-difference time-domain mesh truncation", IEEE Microwave and Guided Wave Letters, vol. 6, no. 2, pp. 94, 1996.
- [99] S. D. Gedney, "An anisotropic perfectly matched layer-absorbing medium for the truncation of FDTD lattices", IEEE transactions on Antennas and Propagation, vol. 44, no. 12, pp. 1630-1639, 1996.
- [100] G. Mur, "Absorbing boundary conditions for the finite-difference approximation of the time-domain electromagnetic-field equations", IEEE transactions on Electromagnetic Compatibility, no. 4, pp. 377-382, 1981.
- [101] W. C. Chew and W. H. Weedon, "A 3D perfectly matched medium from modified Maxwell's equations with stretched coordinates", Microwave and optical technology letters, vol. 7, no. 13, pp. 599-604, 1994.
- [102] R. Holland, "Finite-difference time-domain (FDTD) analysis of magnetic diffusion" IEEE transactions on electromagnetic compatibility, vol. 36, no. 1, pp. 32-39, 1994.
- [103] B. Wei, S. Q Zhang, F. Wang, and D. Ge, "A novel UPML FDTD absorbing boundary condition for dispersive media", Waves in Random and Complex Media, vol. 20, no. 3, pp. 511-527, 2010.
- [104] S. A. Cummer, "A simple, nearly perfectly matched layer for general electromagnetic media", IEEE microwave and wireless components letters, vol. 13, no. 3, pp. 128-130, 2003.

- [105] T. Y. Yu, "Condition assessment of GFRP-retrofitted concrete cylinders using electromagnetic waves", Doctoral dissertation, Massachusetts Institute of Technology, 2008.
- [106] H. C. Rhim and O. Büyüköztürk, "Electromagnetic properties of concrete at microwave frequency range", *Materials Journal*, vol. 95, no. 3, pp. 262-271, 1998.
- [107] H. Chung, J. Cho, S. G. Ha, S. Ju and K. Y. Jung, "Accurate FDTD dispersive modeling for concrete materials", ETRI Journal, vol. 35, no. 5, pp. 915-918, 2013.
- [108] D. Hughes, R. Zoughi, "A method for evaluating the dielectric properties of composites using a combined embedded modulated scattering and near-field microwave nondestructive testing technique, Proceedings of the 18th IEEE Instrumentation and Measurement Technology Conference, Rediscovering Measurement in the Age of Informatics (Cat. No. 01CH 37188), vol. 3, pp. 1882-1886, IEEE, 2001.
- [109] D. Hughes and R. Zoughi, "A novel method for determination of dielectric properties of materials using a combined embedded modulated scattering and near-field microwave techniques-Part I: Forward model", IEEE Transactions on Instrumentation and Measurement, vol. 54, no. 6, pp. 2389-2397, 2005.
- [110] S. I. Ganchev, S. Bakhtiari, and R. Zoughi, "A novel numerical technique for dielectric measurement of generally lossy dielectrics", IEEE Transactions on Instrumentation and Measurement, vol. 41, no. 3, pp. 361-365, 1992.
- [111] T. Asakura, M. Toyoda, and T. Miyajima, "Numerical and experimental investigation on structure-borne sound transmission in multilayered concrete structures", Journal of Sound and Vibration, vol. 413, pp. 1-25, 2018
- [112] M. V. Mohod and K. N. Kadam, "A comparative study on rigid and flexible pavement: A review", IOSR Journal of Mechanical and Civil Engineering (IOSR-JMCE), vol. 13, no. 3, pp. 84-88, 2016.
- [113] Technical Tutoring, Available online: http://www.hyperad.com/tutoring/math/calculus/construction\_of\_the\_riemann\_integral.ht m (accessed on 15th November 2020).
- [114] U. S. Sener, and S. Eker, "Nondestructive Approach for Complex-Shaped Cracks in Concrete Structures by Electromagnetic Waves with FDTD Technique", Mathematical Problems in Engineering, 2021
- [115] W. C. Chew, J. M. Jin, C. C. Lu, E. Michielssen, and J. M. Song, "Fast solution methods in electromagnetics", IEEE Transactions on Antennas and Propagation, vol. 45, no. 3, pp. 533-543, 1997.
- [116] A. Benedetto, F. Tosti, L. B. Ciampoli, and F. D'amico, "An overview of ground-penetrating radar signal processing techniques for road inspections", Signal processing, vol. 132, pp. 201-209, 2017.
- [117] U. S. Sener, and S. Eker, "A Novel Heterogeneous Model of Layered Structures for Numerical Modeling and Simulation at Microwave Frequencies via FDTD", European Journal of Technique, vol. 10, no. 2, pp. 289-300, 2020.

- [118] U. S. Sener, and S. Eker, "Microwave Non-Destructive Testing Technique for Material Characterization of Concrete Structures via Electromagnetic Waves with FDTD", ACES Journal, vol. 35, no. 11 pp. 1390-1391, IEEE, 2020.
- [119] P. Shangguan and I. L. Al-Qadi, "Calibration of FDTD simulation of GPR signal for asphalt pavement compaction monitoring", IEEE Transactions on Geoscience and Remote Sensing, vol. 53, no. 3, pp. 1538-1548, 2014.
- [120] M. Solla, R. Asorey-Cacheda, X. Núñez-Nieto, and B. Conde-Carnero, "Evaluation of historical bridges through recreation of GPR models with the FDTD algorithm" Ndt & E International, vol. 77, pp.19-27, 2016.
- [121] L. Binda, G. Lenzi, and A. Saisi, "NDE of masonry structures: use of radar tests for the characterisation of stone masonries", Ndt & E International, vol. 31, no. 6, pp. 411-419, 1998.
- [122] O. Büyüköztürk, M. J. Buehler, D. Lau, and C. Tuakta, "Structural solution using molecular dynamics: Fundamentals and a case study of epoxy-silica interface", International Journal of Solids and Structures, vol. 48, no. 14, pp. 2131-2140, 2011.
- [123] O. Büyüköztürk and T. Y. Yu, "Understanding and assessment of debonding failures in FRP-concrete systems", Seventh International Congress on Advances in Civil Engineering, pp. 11-13, 2006.
- [124] O. Gunes, O. Buyukozturk, and E. Karaca, "A fracture-based model for FRP debonding in strengthened beams", Engineering Fracture Mechanics, vol. 76, no. 12, pp. 1897-1909, 2009.
- [125] G. Ji, G. Li, and W. Alaywan, "A new fire resistant FRP for externally bonded concrete repair", Construction and Building Materials, vol. 42, pp. 87-96, 2013.
- [126] U. S. Sener, and S. Eker, "Microwave Non-Destructive Testing Technique for Defect Detection of Composite Piles via Electromagnetic Waves with FDTD", 2019 International Applied Computational Electromagnetics Society Symposium (ACES) pp. 1-2, IEEE, 2019.
- [127] P. K. Mehta, "Concrete. Structure, properties and materials", 1986.
- [128] M. I. Mousa, M. G. Mahdy, A. H. Abdel-Reheem, and A. Z. Yehia, "Self-curing concrete types; water retention and durability", Alexandria Engineering Journal, vol. 54, no. 3, pp. 565-575, 2015.
- [129] V. Kodur, and W. Khaliq, "Effect of temperature on thermal properties of different types of high-strength concrete", Journal of materials in civil engineering, vol. 23, no. 6, pp. 793-801, 2011.
- [130] C. A. Balanis, "Antenna theory: analysis and design", John wiley & sons, 2015.
- [131] E. P. Li, E. X. Liu, L. W. Li and M. S. Leong, "A coupled efficient and systematic full-wave time-domain macro modeling and circuit simulation method for signal integrity analysis of high-speed interconnects", IEEE Transactions on Advanced packaging, vol. 27, no. 1, pp. 213-223, 2004.
- [132] F. Costa, M. Borgese, M. Degiorgi, and A. Monorchio, "Electromagnetic characterization of materials by using transmission/reflection (T/R) devices", Electronics, vol. 6, no. 4, 95, 2017.
- [133] C. Xu, "Computational Electrodynamics and Simulation in High Speed Circuit Using Finite Difference Time Domain (FDTD) Method", Master thesis, St. Cloud State University, 2018.

## **PUBLICATIONS FROM THE THESIS**

## **Conference Papers**

- **1.** U. S. Sener, and S. Eker, "Microwave Non-Destructive Testing Technique for Defect Detection of Composite Piles via Electromagnetic Waves with FDTD", 2019 International Applied Computational Electromagnetics Society Symposium (ACES) pp. 1-2, IEEE, 2019.
- 2. U. S. Sener, and S. Eker, "Condition Investigations of Concrete Cylinders Using Electromagnetic Waves at Microwave Frequencies", 2021 International Applied Computational Electromagnetics Society Symposium (ACES) pp. 1-2, IEEE, 2021.

## **Papers**

- **1.** U. S. Sener, and S. Eker, "Microwave Non-Destructive Testing Technique for Material Characterization of Concrete Structures via Electromagnetic Waves with FDTD", ACES Journal, vol. 35, no. 11 pp. 1390-1391, IEEE, 2020. <a href="https://doi.org/10.47037/2020.ACES.J.351164">(https://doi.org/10.47037/2020.ACES.J.351164</a>)
- 2. U. S. Sener, and S. Eker, "A Novel Heterogeneous Model of Layered Structures for Numerical Modeling and Simulation at Microwave Frequencies via FDTD", European Journal of Technique, vol. 10, no. 2, pp. 289-300, 2020. [https://doi.org/10.36222/ejt.777489]
- 3. U. S. Sener, and S. Eker, "Nondestructive Approach for Complex-Shaped Cracks in Concrete Structures by Electromagnetic Waves with FDTD Technique", Mathematical Problems in Engineering, 2021. <a href="https://doi.org/10.1155/2021/6624982">(https://doi.org/10.1155/2021/6624982)</a>